Search for a Neutrino Signal from the Fermi Bubbles with the ANTARES Telescope

Masterarbeit aus der Physik

vorgelegt von

Steffen Hallmann

6. September 2015

Erlangen Centre for Astroparticle Physics
Physikalisches Institut
Friedrich-Alexander-Universität Erlangen-Nürnberg

1. Gutachter: Prof. Dr. Gisela Anton
2. Gutachter: Prof. Dr. Christopher van Eldik

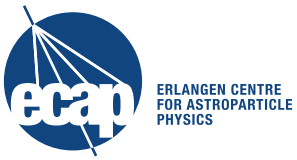

Abstract

In 2010 the discovery of the Fermi Bubbles – two large γ-ray lobes above and below the Galactic Centre – caused a lot of excitement. Since then many models have been proposed to explain their origin, but to date the mechanism producing the bubbles remains unclear. The detection of a neutrino signal from the Fermi Bubbles could help to distinguish hadronic from leptonic acceleration mechanisms, which are the two main groups of proposed models. This hypothesised neutrino signal is searched for using data from the ANTARES Cherenkov telescope, which is currently the largest deep-sea neutrino detector in operation.

In this thesis, data collected in 2012 and 2013 is analysed using neutrino interactions that leave track-like event signatures in the detector. Taking into account the latest results on the γ-ray flux measured by Fermi-LAT, this analysis updates an existing search for a signal from the Fermi Bubbles based on 4 years of ANTARES data (2008–2011). For the six years of data in total, a combined excess of 1.9σ is observed and new upper limits are set.

Kurzfassung

2010 wurden die Fermi Bubbles – zwei große blasenfömige Strukturen von γ-Strahlung ober- und unterhalb des Galaktischen Zentrums – entdeckt. Mit großer Aufregung wurde seitdem an Modellen gearbeitet, welche versuchen die Entstehung der Fermi Bubbles zu erklären. Bis heute ist jedoch nicht zweifelsfrei geklärt, welcher Mechanismus zu deren Entstehung führt. Der Nachweis eines Neutrino-Signals von den Fermi Bubbles könnte zur Unterscheidung von hadronischen und leptonischen Entstehungsszenarien beitragen. In diese beiden Szenarien lassen sich die meisten der vorgeschlagenen Modelle eingruppieren. Die Daten des größten derzeit betriebenen Cherenkov-Detektors in der Tiefsee, ANTARES, eignen sich am besten für eine solche Suche nach einem angenommenen Neutrino-Fluss aus den Fermi Bubbles.

Diese Arbeit analysiert die 2012 und 2013 genommenen Daten unter Verwendung von Neutrino-Wechselwirkungen, die spurartige Signaturen im Detektor hinterlassen. Die Analyse ist ein Update einer bestehenden 4–Jahres-Analyse (2008–2011) und berücksichtigt die neuesten Fermi-LAT Ergebnisse zum γ-Fluss aus den Fermi Bubbles. Für die insgesamt sechs analysierten Jahre wird ein statistisch insignifikanter Exzess von 1.9σ beobachtet. Neue obere Grenzen auf den Neutrino-Fluss werden daher gesetzt.

Contents

1 | Introduction: The Fermi Bubbles

The Fermi LAT experiment has revealed two giant lobes of γ–ray emission extending $7-8\,\mathrm{kpc}$ ($\approx 50°$) above and below the Galactic Centre, which are commonly referred to as the Fermi Bubbles (FB) [1]. Fig. 1 visualises the impressive size of the FB compared to our galaxy. Structures in spatial correlation to the FB have also been observed in the radio wave band [2], in the micro-wave band [3] and, predominantly towards the region close to the Galactic Centre, in X-rays [4]. A rough impression of where these related structures are located on the galactic sky for the different bands is given in Fig. 2.

To date the mechanism generating the Fermi Bubbles remains unknown. Many models have been proposed, which on the one side try to explain the properties of the γ-ray flux and on the other side also try to accomodate the structures observed in other wave-length bands.

Besides attempts to attribute at least part of the emission to decay of dark matter [7, 8], most of the models employ processes contained in the standard model of particle physics to explain the observed structures.

The symmetric shape of the lobes suggests that they are created close to the Galactic Centre, or by the central super-massive black hole, Sgr A*, itself. Whilst it is known that Sgr A* is quiescent at present, a past period of accretion could have lead to a jet-like emission known from other galaxies that host an AGN (active galactic nucleus) [1, 9]. Also, hot plasma outflows from the black hole have been proposed, which could be driven by periodic disruption of stars accreted onto the black hole [10]. Alternatively, a period of intense star formation in the central region of our galaxy – a starburst – and consequently a high rate of supernova explosions might cause a hot superwind driving relativistic particles out [1, 2, 11]. (c.f. [12, Sec. 4.6.1.])

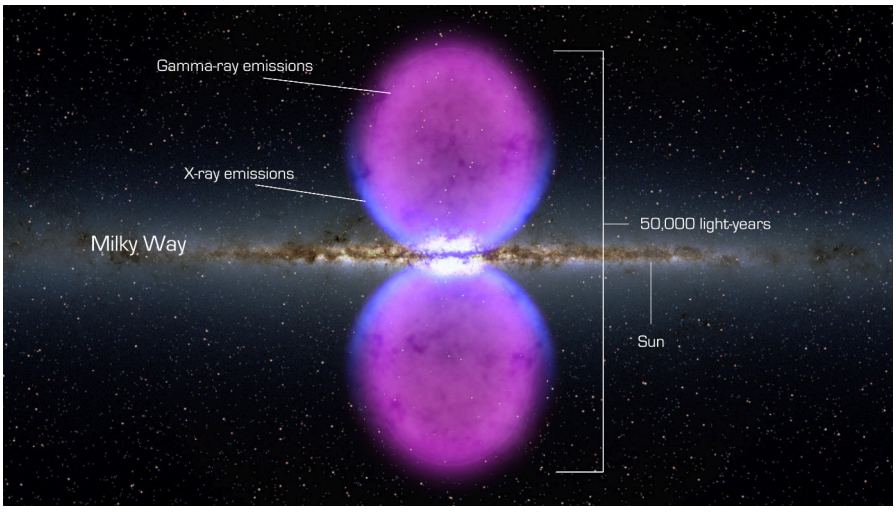

Figure 1: An artists impression illustrates the monumental size of the Fermi Bubbles within our galaxy. Figure taken from Ref. [5].

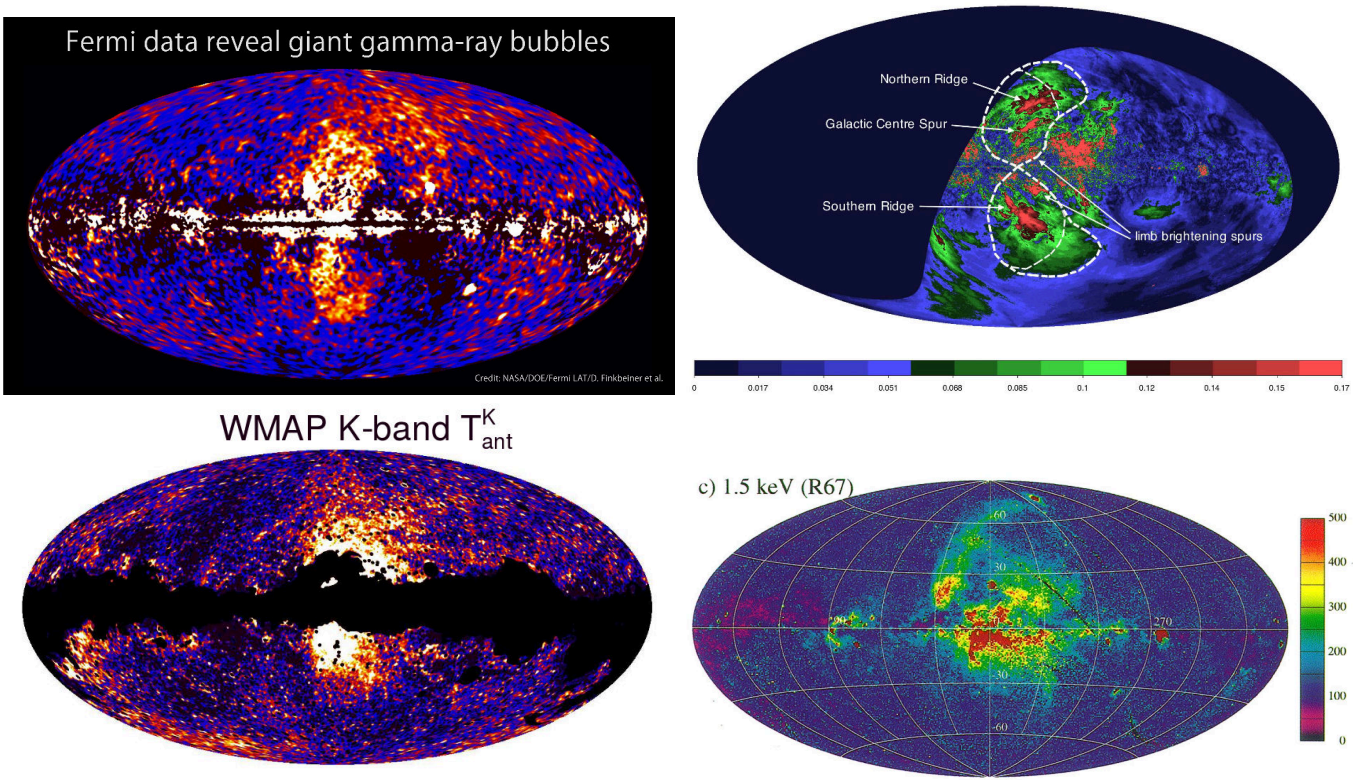

Figure 2: The Fermi Bubbles and related structures seen in different bands: *Top left:* γ–rays (Fermi-LAT), *Top right:* radio (S-PASS), *Bottom left:* micro-wave (WMAP), *Bottom right:* X–rays (ROSAT). Figures taken from Ref. [5, 2, 6, 4]. See these references for details and descriptions of intensity units.

Depending on whether electrons or protons are accelerated at the source, models are naturally subdivided into leptonic and hadronic emission scenarios:

In leptonic mechanisms [1, 13, 14] the γ-ray signal is produced by inverse compton scattering, when relativistic electrons hit on low energy photons from the cosmic microwave background or from ambient starlight and boost them to high energies.

In contrast, in hadronic scenarios [13, 11, 15] high energy protons interact with interstellar matter producing mainly charged ($\pi^{\pm}$) and neutral (π^0) pions. Their dominant decay channels are in turn

$$\pi^0 \longrightarrow \gamma\gamma \tag{1}$$

causing the γ-signal, and

$$\begin{aligned} \pi^- &\longrightarrow \mu^- + \overline{\nu}_\mu & \qquad \pi^+ &\longrightarrow \mu^+ + \nu_\mu \\ \mu^- &\longrightarrow e^- + \overline{\nu}_e + \nu_\mu & \qquad \mu^+ &\longrightarrow e^+ + \nu_e + \overline{\nu}_\mu, \end{aligned} \tag{2}$$

which leads also to a corresponding neutrino signal.

Hence, an observation of a neutrino flux from the Fermi Bubbles – present in hadronic, but absent in leptonic models – gives a unique possibility to distinguish hadronic from leptonic processes generating the γ–ray signal observed by Fermi-LAT.

Both hadronic and leptonic models have been proposed for all of the three scenarios of acceleration mentioned above, which can more or less naturally explain all of the properties of the γ-ray flux and the other correlated multi-wavelength observations. A short review with references for further reading can be found in Ref. [12, Sec. 4.6.1.].

A major difference between hadronic and leptonic scenarios is the timescale on which the injection has happened. Whereas high energy protons are not subject to cooling (and consequently can have been injected some $10^6 - 10^9$ years ago), electrons will lose energy more rapidly, eg. via synchrotron emission in magnetic fields. As a consequence, the energy spectrum for electrons will soften significantly on a timescale of beyond $10^5 - 10^6$ years, which is the typical cooling time for TeV electrons. (c.f. [12, Sec. 4.6.1.]). Consequently, a precise measurement of the energy spectrum of the FB emission and subsequent spectral fits from both hadronic and leptonic γ–ray production, can also be used to differentiate between the two scenarios of emission. The precise measurement is complicated by the fact that known foreground and background γ–ray sources need to be subtracted, which introduces systematic errors. Such an analysis of fitting hadronic and leptonic templates to the full γ-ray sky measured by Fermi has recently been done and suggests that hot outflows like the Fermi Bubbles might be dominated by leptonic processes [16]. Since to date the level of contribution from leptonic and hadronic processes to the FB signal is not known, the most optimistic case for neutrino astronomy of purely hadronic emission is assumed.

The neutrino flux that can be expected from hadronic emission in the FB is derived in Sec. 2. Then, in Sec. 3, the ANTARES neutrino detector is described together with the two main signatures: track- and shower-like events. A search based on track-like neutrino events from the FB has already been performed using 4 years of data recorded

from 2008 to 2011 with the ANTARES detector [17].[1] Taking this existing 4–year analysis up, two additional years, 2012 and 2013, are analysed in Sec. 4. From this the combined result for 6 years of ANTARES data using tracks is obtained. The analysis focusses on track-like events, on which ANTARES has an excellent median angular resolution of 0.5° [19]. Recently developed reconstruction algorithms have also achieved median angular resolutions of $3° - 5°$ for shower-like interactions [20, 21]. The conclusion in Sec. 5 will therefore also give an outlook on the future plans of a combined FB analysis using tracks- and showers.

2 | Expected neutrino flux from the Fermi Bubbles

The FB are uniformly bright across their extension and have sharp edges. Their most interesting feature with respect to neutrino astronomy however is a hard γ-ray spectrum [1].

Due to its limited size, the Fermi satellite can only measure the photon spectrum to energies of some 100 GeV. The spectrum and cutoff of the FB signal at higher energies is to date undetermined. However, the northern bubble is visible to the ground based HAWC Gamma-Ray Observatory, which has started data-taking in its full configuration in spring 2015. A preliminary analysis based on data recorded with a partial array of the HAWC Gamma-Ray Observatory (HAWC-111) can already exclude an E^{-2} power-law with no cut-off for γ-ray energies between 10^4 and 10^5 GeV [22]. For a prediction of the neutrino flux that can be measured with ANTARES, the energy region above ≈ 10 TeV is most interesting. While HAWC might provide precise flux measurements in the future, at present the Fermi-LAT data needs to be extrapolated to higher energies. In this analysis, as in the 4–year analysis, the γ–ray flux is modeled with a simple power-law spectrum with spectral index α and an exponential cutoff at a cut-off energy E_{cutoff},

$$\Phi_\gamma(E) \propto E^{-\alpha} \times \exp\left(\frac{E}{E_{\mathrm{cutoff}}}\right). \tag{3}$$

The first Fermi-LAT analysis [1] measured a spectrum compatible with a power-law $E^{-\alpha}$ with a spectral index $\alpha = 2$ and no cut-off was observed. The corresponding γ-flux is

$$E^2 \frac{\mathrm{d}\Phi_\gamma}{\mathrm{d}E} \approx 3 - 6 \times 10^{-7}\,\mathrm{GeV\ cm^{-2}\ s^{-1}\ sr^{-1}}. \tag{4}$$

The most recent analysis on the spectrum of the Fermi Bubbles by Fermi-LAT [23] prefers a softer spectrum or very low cut-off energies at the sub-TeV scale. Using a parametrisation for the γ-flux that is produced in hadronic interactions derived from the SYBILL-code [24], the authors of Ref. [25] show that an $E^{-2.25}$ proton spectrum can produce a γ-flux that gives a good fit to the Fermi-LAT data. A power-law fit to this parametrisation at energies beyond 10 GeV (see Fig. 3) yields a spectral index of

[1] Hereinafter the indication '4–year analysis' implies that what is described has been developed in Ref. [17]. A more detailed description of the analysis method can be found in Ref. [18].

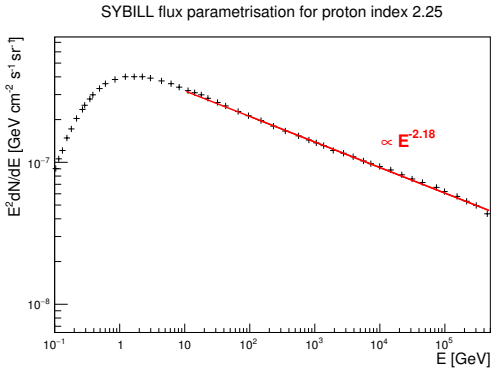

Figure 3: The γ–flux parametrisation (black crosses) of the SIBYLL-code [24] for a proton spectrum with a spectral index of 2.25 is fit with a power-law at energies above 10 GeV (red line). From this an index of $\alpha = 2.18$ for the power-law spectrum is obtained.

$\alpha = 2.18$ and a γ-flux (c.f. [25, Fig. 2])

$$E^{2.18}\frac{\mathrm{d}\Phi_\gamma}{\mathrm{d}E} \approx 0.5 - 1.0 \times 10^{-6}\,\mathrm{GeV}^{1.18}\ \mathrm{cm}^{-2}\ \mathrm{s}^{-1}\ \mathrm{sr}^{-1}. \tag{5}$$

In addition, a full parameter scan (see Appendix A) for different cut-off energies and spectral indices confirms that $\alpha = 2.18$ is a choice that gives an acceptable fit to the Fermi-LAT data whilst allowing for high cut-off energies. These are necessary for ANTARES since at low energies the neutrino flux produced in the atmosphere will dominate and make the detection of a FB signal with low cut-off impossible.

Note that the $\approx \pm 30\%$ uncertainty in the γ-fluxes (Eq. 4 and Eq. 5) is mainly due to systematic uncertainties that come from the subtraction of known sources in the γ–ray sky maps. The spectra of the γ–ray lobes and the two flux extrapolations are shown in Fig. 4.

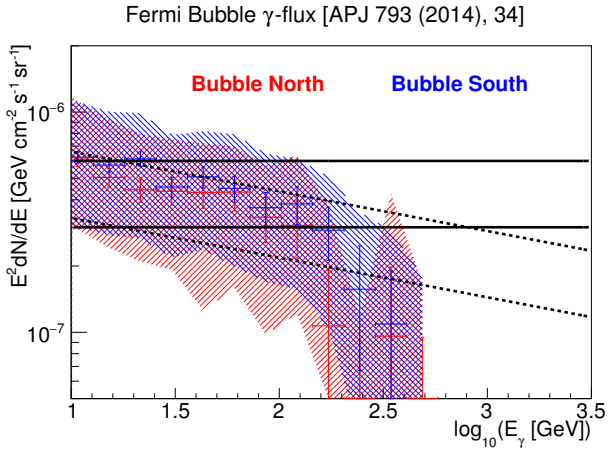

Figure 4: The γ–ray spectra of the more recent Fermi Bubble analysis [23] with the corresponding statistical (error bars) and systematic (shaded bands) uncertainties for energies above 10 GeV are superposed with the flux extrapolations for spectral indices $\alpha = 2.0$ (see Eq. 4) in solid and $\alpha = 2.18$ (see Eq. 5) in dashed.

In a purely hadronic emission scenario the γ-ray flux and the corresponding neutrino flux originate mainly from the decay of neutral and charged pions, which in turn are produced in collisions of cosmic-ray protons with the interstellar gas. At high energies the neutrino and γ-ray flux in this hadronic case differ only by a scaling factor $\xi(\alpha)$ [26],

$$\Phi_\nu(E) = \xi(\alpha) \times \Phi_\gamma(E). \tag{6}$$

Figure 5: Proportionality factors $\xi(\alpha)$ of the neutrino (red) and anti-neutrino (blue) fluxes to the corresponding γ–flux as a function of the spectral index α (calculated using [26, Eq. 35]):

	ν_μ	$\overline{\nu}_\mu$
$\xi(2.00)$	0.211	0.196
$\xi(2.18)$	0.188	0.175

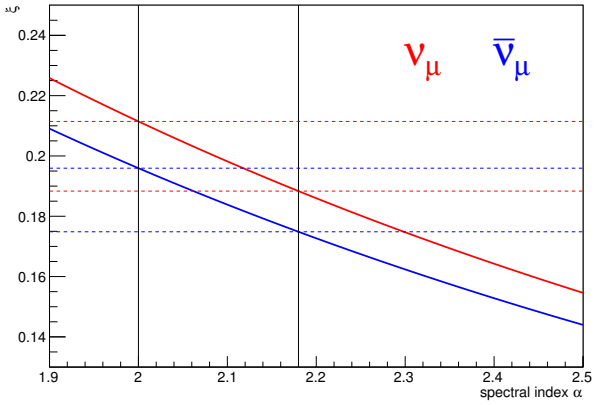

The scaling depends on the spectral index of the γ-rays, α, and drops with steeper spectra, as shown in Fig. 5. While at the source only electron and muon neutrinos are produced, they are subject to vacuum oscillations[2] on their way to Earth. At the detector, the flavour ratio will be almost equal, $\Phi_{\nu_e} : \Phi_{\nu_\mu} : \Phi_{\nu_\tau} \approx 1 : 1 : 1$. For the combined neutrino and anti-neutrino flux of one flavour, the proportionalities are $\xi(2.0)_{\nu_\mu+\overline{\nu}_\mu} = 0.41$ for a spectral index $\alpha = 2.0$ and $\xi(2.18)_{\nu_\mu+\overline{\nu}_\mu} = 0.36$ for $\alpha = 2.18$.

It is assumed that protons can only be efficiently accelerated up to energies of 1–10 PeV within our galaxy [11]. This will induce also a cutoff in the observed γ-ray and neutrino spectra. As a crude approximation 20% of the proton energy is on average converted into charged pions. Equipartition of this energy over the four daughters in pion decay yields

$$E_{\mathrm{cutoff},\nu} = \frac{1}{20} \times E_{\mathrm{cutoff},p} \tag{7}$$

for the neutrino cutoff, i.e. cutoffs ranging from 50 to 500 TeV.

Taking into account the scaling factors for the spectral indices α gives the expected neutrino fluxes

$$E^\alpha \frac{\mathrm{d}\Phi_{\mathrm{model},\nu_\mu+\overline{\nu}_\mu}}{\mathrm{d}E} = A^\alpha_{\mathrm{model}} \times \exp\left(-\frac{E}{E_{\mathrm{cutoff},\nu}}\right), \tag{8}$$

with

$$A^{2.0}_{\mathrm{model}} = 1.2 - 2.4 \times 10^{-7}\,\mathrm{GeV\ cm^{-2}\ s^{-1}\ sr^{-1}} \qquad \text{for } \alpha = 2.0, \tag{9}$$

for the assumed flux in Eq. 4 and

$$A^{2.18}_{\mathrm{model}} = 1.8 - 3.6 \times 10^{-7}\,\mathrm{GeV^{1.18}\ cm^{-2}\ s^{-1}\ sr^{-1}} \qquad \text{for } \alpha = 2.18 \tag{10}$$

for the flux assumption in Eq. 5, respectively.

The track-analysis in Sec. 4 uses the same appoximation for the FB shape as in the 4–year ANTARES analysis [17]. This geometric shape is defined by

$$\left(l^2 + b^2\right)^2 \leq 50^\circ \cdot 50^\circ \cdot \left(b^2 - l^2\right), \tag{11}$$

[2] See Ref.[27, C. 14] for a review of neutrino properties and oscillation.

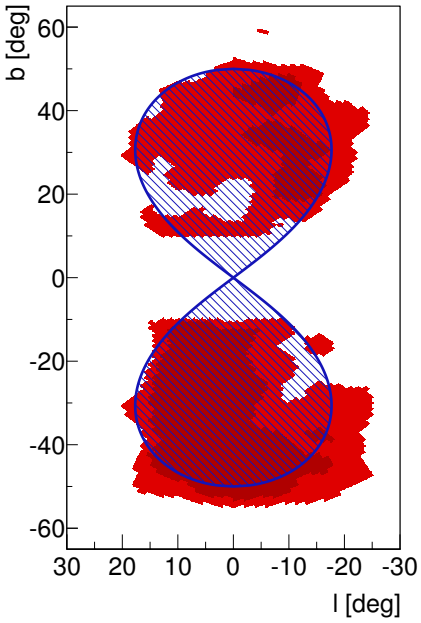

Figure 6: The shape of the FB structure found in Ref. [23] is indicated in red. Additionally, a 'cocoon' substructure (dark red) can be identified, which shows a higher γ-ray intensity. Both the Fermi Bubble shape and the nested 'cocoon' are well covered by the approximation (blue shaded area) used for the track-analysis (74% overlap for the FB and 91% for the 'cocoon'). Figure taken from Ref. [28].

where l and b are the galactic longitude and latitude.

The red area in Fig. 6 shows the shape of the γ-ray lobes as observed by the most recent Fermi-LAT analysis. In search of a sub-structure within the FB a nested 'cocoon' could be identified (Fig. 6, dark red area), which shows an increased γ–ray intensity with respect to the rest of the FB [23]. The geometric approximation still covers the FB structure well (76% overlap). In particular the 'cocoon' structure, with an overlap of 91%, is almost fully contained.

A comparison of the FB shape used by the 4–year analysis and the one presented in the most recent Fermi-LAT publication is given in Fig. 7.

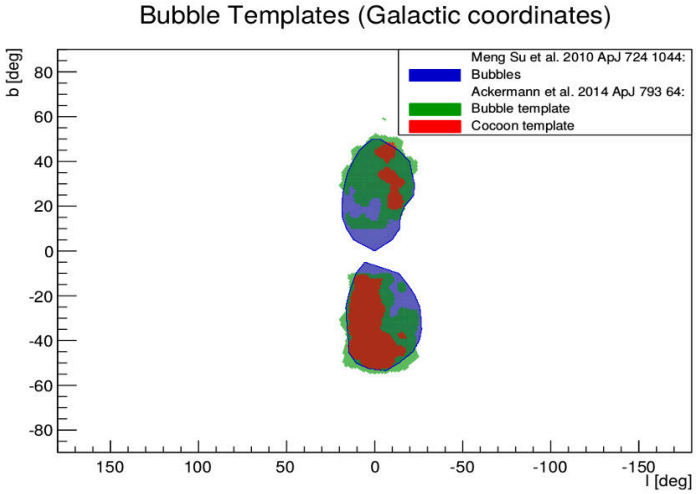

Figure 7: γ-ray templates for the Fermi Bubbles from the earlier [1] and latter [23] Fermi-LAT analysis.

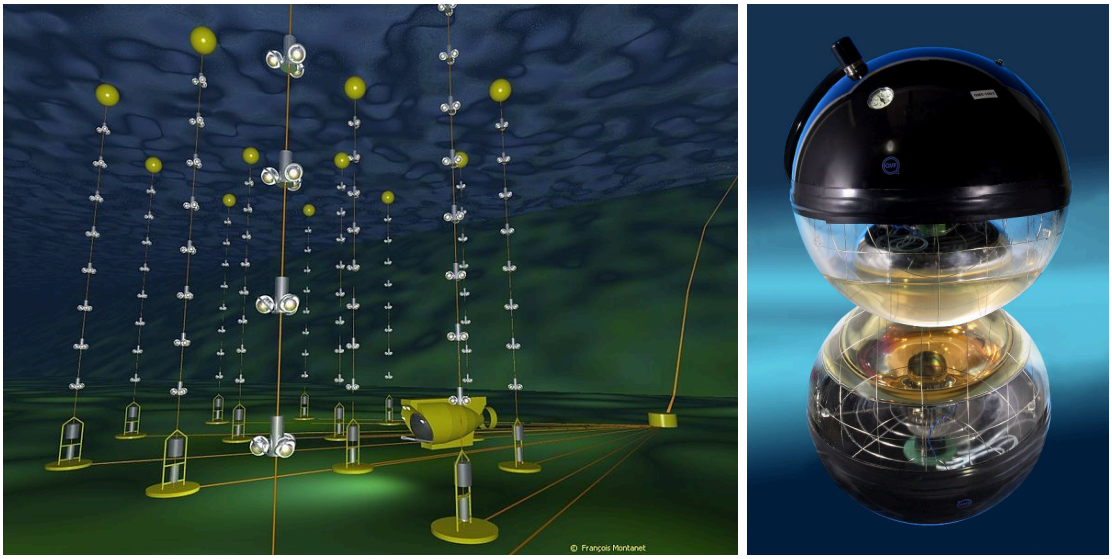

Figure 8: *Left:* Artistic visualisation of the ANTARES detector. The 885 optical modules are arranged in storeys – groups of three optical modules – with a vertical spacing of $14.5\,\mathrm{m}$. The distance between lines is $\approx 70\,\mathrm{m}$. *Right:* Photograph of one optical module and the contained $10\,\mathrm{inch}$ photomultiplier tube laid on a mirror. Figures taken from Ref. [30].

3 | Event reconstruction in the Antares detector

3.1 | The Antares detector

The ANTARES neutrino telescope is located 40 km off-shore from Toulon in the Mediterranean Sea at a depth of $\approx 2.5\,\mathrm{km}$. Since 2008 the detector is taking data in its final configuration. It consists of 885 optical modules (OMs), which are distributed over twelve detection lines in groups of three (so called storeys). The detection lines are anchored to the sea floor and held upright by a buoy. Each optical module hosts one 10 inch photomultiplier tube (PMT). Data is sent to the shore station over an electro-optical fibre. The detector setup is illustrated in Fig. 8 and a more detailed description of the detector can be found in Ref. [29].

3.2 | Neutrino interactions: Track and shower signatures

The PMTs detect Cherenkov light [31] emitted from ultra-relativistic charged secondary particles generated in neutrino interactions. Cherenkov radiation is the coherent emission of light produced in a polar medium like water, when the speed of charged particles exceeds the speed of light in water. The light emission peaks at a characteristic angle of 43° in sea water.

Two main topologies of neutrino interactions can be reconstructed with the ANTARES detector: Muon neutrinos ν_μ can interact with nucleons N within the sea water via

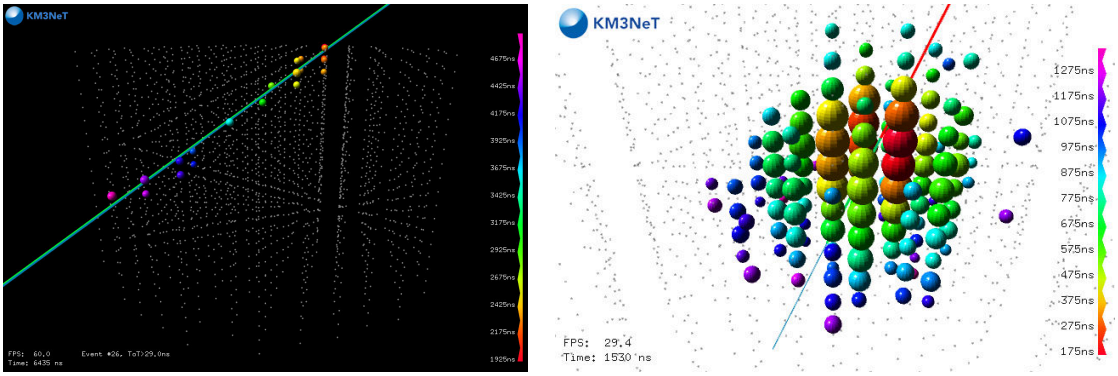

Figure 9: Event display for the sucessor of ANTARES, the future KM3NeT detector. The two main topologies of events are shown. The size of the spheres visualises the charge that was registered by an optical module (OM). Colors indicate the arrival time of the photons at the OM from early (red) to late (pink). *Left:* Track-like event with hit OMs mainly within a cylinder around the muon path. *Right:* Shower-like event with almost point-like emission near the interaction vertex.

charged current interactions

$$\nu_\mu + N \longrightarrow \mu^- + \text{hadronic shower} \tag{12}$$

and produce a hadronic cascade at the interaction vertex and a relativistic muon μ^-, which may traverse distances of several hundred metres in sea water. The anti-neutrino $\overline{\nu}_\mu$ can interact similarly producing a μ^+ and a hadronic cascade.

The relativistic muon then emits Cherenkov light all along its trajectory, hence these events are called 'track-like'. In contrast, other charged particles emitting Cherenkov light will only travel small distances of some metres, such that all light is emitted close to the interaction vertex.

On the other hand, in neutral current interactions of all neutrino flavours

$$\nu + N \longrightarrow \nu' + \text{hadronic shower} \tag{13}$$

and in charged current interactions of the electron neutrino

$$\nu_e + N \longrightarrow e^- + \text{hadronic shower} \tag{14}$$

all Cherenkov light is emitted close to the interaction vertex by the electron or the cascade, giving them a 'shower-like' appearance in the detector.

Both event signatures are visualised in Fig. 9 with an event display [32] for the KM3NeT detector[3], a future neutrino telescope in the Mediterranean Sea, that is now in the construction phase. Since the KM3NeT detector will be much larger than ANTARES, the difference between tracks and showers can be seen more easily.

[3] http://www.km3net.org/

3.3 | Event reconstruction in Antares

When photons hit on an optical module and produce a signal pulse – in ANTARES these are called (L0) 'hits' – the signal is digitised by the local OM electronics and tagged with a time-stamp. ANTARES uses an *all-data-to-shore* principle, which means that all signal is sent to the shore station, where the information from all OM's is collected. To reduce the amount of data that needs to be stored on disk, interesting events are selected by software-triggers. The standard physics triggers are based on so called L1 coincidences, which are *(a)* two coincident (within a time-range of $\leq 20\,\text{ns}$) hits on one storey, or *(b)* one single hit with very high charge (with a charge equivalent to typically more than 3 photoelectrons). (cf. [29]) As in the first FB analysis, four triggers are considered for the analysis, namely **T2**, **T3**, **3N** and **TQ**. These triggers work as follows (cf. [33, 34, 35]):

T2: The T2 trigger requires two L1 hits on neighbouring storeys within a time range of 100 ns.[4]

T3 (more explicitly: 2T3): A 1T3 cluster is a time coincidence of two L1 hits on adjacent or next-to-adjacent storeys. The 2T3 trigger looks for two 1T3 clusters within a time range of 100 ns or 200 ns, respectively.

3N: This trigger is a three dimensional track trigger which scans various directions in the sky and, within $2.2\,\mu\text{s}$, looks for more than 5 causally connected L1 hits along a direction.

TQ: The TQ is a time and charge trigger which also scans various directions in the sky for causally connected hits. It combines L1 hits with L0 hits, i.e. single hits on a storey.

Also, several other triggers exist, e.g. for monitoring purposes, for special incidents and directions (gamma-ray bursts, supernovae, Galactic Centre), or for beyond standard-model physics (slowly moving monopoles).

Triggered data is saved to disk and can be reconstructed with the various reconstruction algorithms for track- and shower-like emission.

Typically, algorithms for track reconstruction assume light emission under the Cherenkov angle along a straight line; those for shower reconstruction assume that the light is emitted under the Cherenkov angle from a point source. Both use the timing and charge information of the hits and project them back onto a hypothesised track or shower position and direction. A minimisation process then results in a fit position and direction. Also, some fit quality parameters are usually obtained.

In this thesis, the track reconstruction algorithm AaFit [19] is used. This fit has two main quality parameters: The track-fit quality, Λ, and an estimate for the angular error of the reconstructed direction, β. Thanks to the long lever arm of track-like events, the

[4] This trigger has not been used in the last years' data taking any more.

direction of the neutrino can be precisely determined from the direction of the muon. The reconstruction accuracy achieved has an excellent angular resolution of only 0.5° [19].

For an estimate of the track energy the ANN energy estimator [36] is used. This determines an energy estimate using Artificial Neutral Networks. These were produced by training a machine learning algorithm to derive the energy estimate from a set of variables which correlate with the energy deposited in the detector, such as the number of hits or the total charge that was deposited on the OMs, or represent the data-taking conditions. The median angular resolution in the relevant energy range ($\approx 10\,\mathrm{TeV}$) is 30% on $\log_{10}(E_{\mathrm{ANN}}\,[\mathrm{GeV}])$ [36].

Also, in Sec. 4.2.3, the Dusj shower reconstruction algorithm is used. Its most important quality parameter is the likelihood for the vertex fit, VLLH. However, for this thesis only the position of the reconstructed shower, and a variable correlating with the energy of the event, the number of used hits by Dusj, will be of importance. A detailed description of the algorithm can be found in Ref. [20]. The Dusj reconstruction algorithm, and also the more recently developed TANTRA reconstruction [21] both achieve angular resolutions of $3-5°$, which opens up the possibility to look for point-sources even with showers [37]. At least for extended sources like the Fermi Bubbles the angular error from reconstruction is small compared to the size of the source. Besides their worse angular resolution compared to tracks, showers also need to interact within or close to the instrumented volume to be accurately reconstructed. This decreases the effective volume of the detector for showers. On the other hand, all the light deposited by shower events interacting close to the detector will be in the range of the OMs. This increases the accuracy of the energy reconstruction. To detect track-like events, only part of the muon track needs to pass the detector. The start or the end of the muon track or the vertex shower may be invisible for the detector. Hence, reconstruction of the deposited energy is more accurate for shower-like events.

Charged current interactions of ν_τ produce a short-lived τ-lepton. Currently no dedicated reconstruction algorithm for ν_τ events exists in ANTARES. However, depending on whether the τ decays into a muon or an electron, the signatures from this channel appear either more track- or shower-like. For this analysis, they are not not considered in the optimisation of the event selection.

The reconstructed data in ANTARES is accessible in SeaTray I3 format, which is based on the IceTray framework[5] by the IceCube Collaboration, and in AntDST[6] format, which is based on ROOT data structures. In this analysis the AntDST files are used.

3.4 | Background contributions for neutrino searches

There are various backgrounds which have to be suppressed in order to observe galactic neutrinos. Background light not caused by Cherenkov emission is produced by ^{40}K decay on the one hand and by bioluminescent organisms in the deap-sea on the other. Whereas the background rate due to ^{40}K decay in marine water is constant over time and has

[5] see http://software.icecube.wisc.edu/offline_trunk/metaproject/overview.html
[6] see http://ific.uv.es/~jpablo/html/main.html

only minor effects on the reconstruction of high energy neutrino events, optical rates can increase dramatically due to bioluminescence and are typically highest in ANTARES during spring time. Bioluminescent activity of micro-organisms like algae leads to an increase of the slowly varying 'baseline rate' registered by the photomultipliers. Larger bioluminescent deep-sea animals use their capability of producing light for defence, hunting, and mating. To these ends they generate light seen as short bioluminescent bursts. The amount of this kind of light is measured with a parameter named 'burst fraction' in ANTARES. (c.f. Ref. [38])

Also, it has been observed in data that rarely malfunctioning photomultipliers can produce sparks of light. These events typically illuminate the whole detector and may be erroneously reconstructed as very bright neutrino events.

A detailed description of the run selection, which suppresses both sparking events and runs with bad data taking conditions due to high optical background rates is given in Sec. 4.2.

In addition to these backgrounds not caused by actual physics events, ANTARES sees also a high background from muons and neutrinos produced in the Earth's atmosphere. Cosmic rays interacting in the atmosphere produce particle cascades which give rise to a down-going flux of atmospheric muons and a flux of atmospheric neutrinos. As opposed to muons, neutrinos only interact weakly with matter and can also penetrate the Earth and reach ANTARES from all directions. These background contributions need to be reduced by an effective event selection described in Sec. 4.5.

3.5 | Run-by-run Monte Carlo simulation

The data collection is organised in runs, which used to be 2–3 hours of data-taking. In spring 2013, the run duration was increased to 12 hours per run. Each data-taking run in ANTARES is simulated with a dedicated Monte Carlo simulation, the run-by-run simulation, to account for the variable data-taking conditions, such as the number of OMs that was active during the run, the baseline rate, and the burst fraction. For atmospheric muons one third of the run's lifetime is simulated using MUPAGE [39], thus in analyses Monte Carlo muons are weighted with a factor 3. Neutrinos are in turn simulated with much higher statistics than detected in the detector. Their event weights are therefore small. In this analysis the atmospheric neutrino signal is weighted with the conventional Bartol flux [40], and the flux derived in Sec. 2 is used for the signal coming from the Fermi Bubbles. Since neutrino experiments suffer from low statistics, the analysis method is tested and optimised using data from the run-by-run simulation only, before unblinding, i.e. looking at, real data from the Fermi Bubbles' region.

4 | Update to the 4–year Antares analysis: Track-like event signatures in 2012/13 data

4.1 | On- and Off-zones

A signal from the Fermi Bubbles is searched for by comparing the number of events observed in the Fermi Bubble region to the background expectation. As in the 4–year analysis, the determination of the expected background is done by using regions which have an identical shape as the signal region but point to other directions on the sky from which no signal is expected. Thanks to the rotation of the Earth, events coming from the same position in Galactic Coordinates are observed from different local directions within the ANTARES detector in the course of the day. Shifting the positions on the galactic sky in time by 1/4, 1/2 and 3/4 of a sidereal day yields three non-overlapping off-zones. The positions of the on- and the three off-zones are fixed in galactic coordinates and can be seen in Fig. 10.

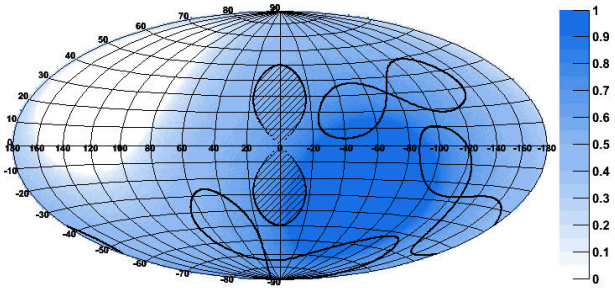

Figure 10: On-zone (shaded region) and the three off-zones in galactic coordinates. The blue colour indicates the visibility from 0 to 1, that is the fraction of the day during which the galactic position is observed with a zenith angle $\geq 90°$ (i.e. up-going) in ANTARES. Figure taken from Ref. [18].

In local coorinates at the detector site, the positions of the zones shift during a sidereal day. For an exemplary point of time (04/08/2015, 16^{00} h) the local positions are shown in Fig. 11. At that moment off-zones 1 and 2 are fully visible to ANTARES. For off-zone 3 only part of the southern lobe is below the horizon. Also only the southern lobe of the on-zone is visible. This illustrates also that during one day the southern bubble has a higher visibility than the northern bubble in ANTARES (see also the colour code of Fig. 10).

Contrary to the IceCube detector, where – thanks to the unique position on the south pole – on- and off-zones would have equal visibility for each individual point of time (see Appendix B), the visibilities for each zone in ANTARES is different at particular times. However, visibilities for the on-zone and each of the off-zones will equalise for a homogeneous data-taking over a sufficiently long range of time. In reality, the ANTARES-telescope is a very dynamic detector with varying optical background from bioluminescence. Additionally optical modules, entire lines, or even the whole detector happen to be in-active for certain periods. This can induce differences in the visibility for the different zones. Below, in Sec. 4.4.1, it is therefore verified that the background expectation is indeed equal for all zones in the analysed data-set.

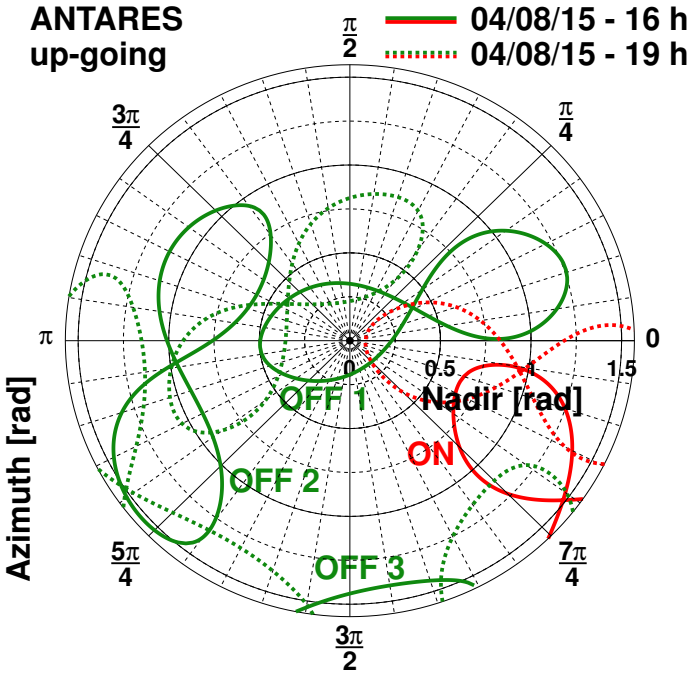

Figure 11: On-zone (red, solid) and the three off-zones (green, solid) as seen within the ANTARES detector at a particular time. The range of nadir angles is restricted to up-going events. The dashed lines illustrate the local positions within the detector three hours later. The off-zones are shifted in time by 6 (off-zone 1), 12 (off-zone 2) and 18 hours (off-zone 3) with respect to the on-zone.

4.2 | Data for the analysis update

The existing 4–year FB analysis has analysed data from 2008 to 2011. Since then 2012 and 2013 data have been processed and are now available for analysis. Furthermore, except for one single run (run `46195`), a range of runs taken from end-December 2009 to mid-February 2010 (runs `45495`→`46576`)[7] was not analysed in the existing analysis due to problems with the data production. These runs are now reprocessed and added to the analysis.

4.2.1 | Basic run selection

In ANTARES each data-run is assigned a quality basic value QB from 0 to 4. A standard selection recommended by the data-quality working group is to use runs with $QB \geq 1$. This essentially ensures that data has been recorded throughout the duration of the run and the trigger rates of one standard trigger, the `3N` trigger, are in an acceptable range from 10^{-2} to 10^{2} Hz. Runs failing to meet this criterium usually have technical problems. Higher quality basic values require that more than 80% of the optical modules are actively taking data ($QB \geq 2$) and that the optical background from bioluminescence is low (baseline $< 120\,\text{kHz}$ and burst fraction < 0.4 for $QB \geq 3$, baseline $< 120\,\text{kHz}$ and burst fraction < 0.2 for $QB \geq 4$) [41, 5.2]. In this analysis the standard selection $QB \geq 1$ is used and only regular physics runs are selected. The latter requirement excludes runs

[7] although some runs of 2009 are part of this group of runs, for simplicity this period will be refered to as the 2010 data

that carry one of the following data-base flags:

- `SCAN:` These runs have been taken for monitoring during the optimisation of parameter settings.
- `PRELIM`: These runs have been taken with preliminary settings after changing some setup parameters.
- `HALF, OVER`: The gain of the PMTs has been reduced by 1/2, 1/4 or 1/8 in these runs. They behave very differently from the runs taken with the nominal gain.
- `SPARKING`: These runs are confirmed to be sparking (these are given in the 2007–2011 list in Sec. D.1). See Sec. 4.2.3 for a detailed description and the identification of additional sparking runs.

According to the data base, the collected lifetime passing this basic requirement 252 days in 2012 and 286 days in 2013, the period of 2010 contributes 39 days.

4.2.2 | From the basic run selection to the final sample

Starting off from 4149 runs passing the basic selection, the final sample of runs is obtained after five subsequent reduction steps. These steps exclude from the analysis:

1. **Runs with incomplete data file:**
   For reconstruction a run is sometimes split into several parts, to keep the time needed for processing reasonably small. Even if only part of the data for a run is missing due to processing failures it is precluded from the analysis.
2. **Runs with incomplete run-by-run Monte Carlo simulation:**
   For this analysis the version 3 of the run-by-run simulation is used. At the time of finalising this analysis, the processing has not been fully completed. Hence, runs where no full corresponding Monte Carlo simulation is available, need to be excluded.
3. **Runs that are identified or suspicious to be sparking:**
   A priory, only the sparking runs from 2007 to 2011 that are confirmed to be sparking are already excluded from the analysis. Additional runs that are sparking are hence excluded from the analysis: While for 2012 preliminary lists exist, analyses using 2013 data [37, 42, 43] have only been finalised simultaneously with this analysis. Amongst these, the ANTARES point-source analysis using tracks and showers [37] has tried to identify sparking runs and found three runs for 2013 data (`70201`, `70203`, `70633`), which are all confirmed to be clearly sparking by the method developed in this analysis, which is presented in Sec. 4.2.3.
4. **Runs with processing problems:**
   Under items 1.) and 2.) runs, where the data file or part of the corresponding simulation files was not present, are already subtracted. However, sometimes the

Table 1: Number of runs passing the selection criteria for the analysis. Runs in each row satisfy all previous requirements. A list of the final set of 2568 runs used for the analysis is given in Appendix C.

year	2010	2012	2013	Σ	
regular physics runs with $QB \geq 1$	337	2636	1176	4149	
data file complete	316	2626	1130	4072	- 2%
RBR V3 Monte Carlo complete	248	1909	940	3097	-24%
not identified as sparking	248	1881	938	3067	- 1%
no processing problems	204	1572	889	2665	-13%
good data/MC agreement	198	1511	859	2568	- 4%

attempt to read the AntDST file which was used for the analysis failed. Most of these errors occured because the AntDST file to be read was corrupt. More precisely, broken ROOT baskets, which are some partition of the data file in the AntDST, and buffer or compression errors caused during production of the AntDST files gave rise to problems.

5. **Runs, where the agreement with the run-by-run simulation is bad:** The method used in the 4–year analysis selects only runs for which the data is well described by the run-by-run simulation. This method is attuned to both the new dataset and the new version of the Monte Carlo simulation (RBR V3) in Sec. 4.2.4.

Tab. 1 lists the number of runs available for the analysis after each of the above five selection steps. From spring 2013 onwards the length of data-taking runs is increased from 2 hours to 12 hours. This is why the number of runs in 2013 data is much smaller than for 2012. The most dramatic decrease in data is due to the missing files of the RBR V3 simulation, which could be recovered once all files are processed and made available. This includes also the re-processing of Monte Carlo runs where all files were present but partially corrupt. Compared to this, the lifetime that can be gained by recovering runs, where part of the data files is not available or corrupt, is small. However, the intact parts of these runs could rather easily be added to the analysis by adjusting the lifetime in the corresponding Monte Carlo.

The final set of runs comprises a lifetime of

366 days (for a total of 2568 runs),

which can safely be added to the analysis. A full list of runs is given in Appendix C.

In the following, details are given on the identification of runs that are sparking and runs where the agreement between data and the corresponding simulation is bad.

4.2.3 | Identification of sparking runs

It was noticed that in ANTARES occasionally malfunctioning PMTs can produce sparks of light that illuminate the whole detector during a limited time range of usually several

minutes. Such sparking events typically are

- extremely bright, and
- reconstructed close to the problematic OM by shower reconstruction algorithms.

These fake events may be erroneously reconstructed as very high energy neutrino events and unfortunately even obtain a good reconstruction quality. Hence, if a run is identified to contain sparking events, it is usually excluded from physics analyses.

Previous attempts to find sparking runs have exploited at least one of their main properties, brightness and proximity to an OM. For the identification one method uses a high rate of events for which the respective reconstruction algorithm has used many hits to fit the track or shower. For the AaFit track reconstruction algorithm runs that have a high rate of events with more than 200 used hits are clearly sparking. The same applies for the Dusj shower reconstruction and more than 100 used hits. The comparison of a standard run and a sparking run that can be identified with this method is shown in Fig. 12. This method may however miss problematic runs if the sparks are less bright or directed away from the detector (see Fig. 13).

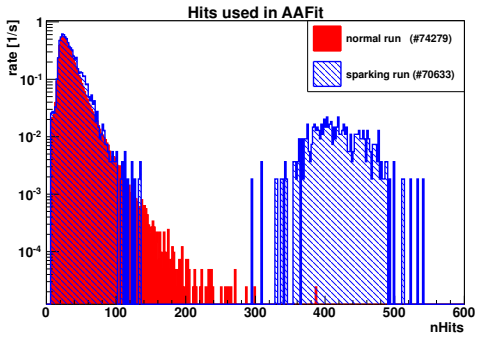

Figure 12: The high rate of events with more than 200 hits used by the AaFit track reconstruction present in the sparking run (blue) is absent in a standard run (red).

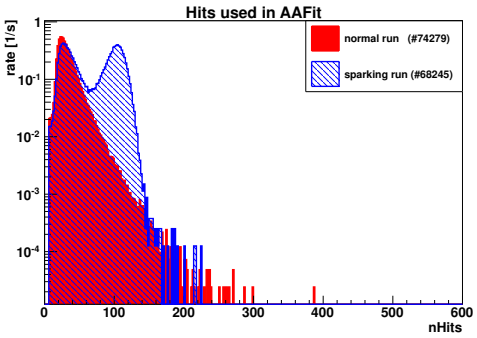

Figure 13: Run number 68245 (blue) behaves very differently from a standard run (red). Nevertheless it is impossible to identify this run as sparking by a high rate of events with more than 200 hits used by the AaFit track reconstruction.

Also, sparking runs have an increased rate of bright events where the vertex of the shower fit is close ($\lesssim 15\,\mathrm{m}$) to the nearest optical module [20]. Since just one of the 885 PMTs is expected to be sparking, the additional events at small distances to the optical module will be generated by this particular PMT only. To see a deviation from a normal run, again a hard cut on the number of used hits is applied [44]. Alternatively, it can be checked for all OMs individually, if the light was emitted from the position of this particular OM [41]. This method may even indicate which of the PMTs is sparking.

In this analysis a complementary approach is used to identify sparking runs: Since in a sparking run the light flash is expected to be emitted from the same OM, the reconstructed vertices of the very brightest events should cluster near this particular problematic

OM. For all available physics runs passing the basic quality selection (Sec. 4.2.1), the 25 events with the most hits used by the Dusj shower reconstruction are picked and the average pairwise distance of their vertices,

$$\overline{r}(n) = \frac{\sum_{i=1}^{n-1}\sum_{j=i+1}^{n} r_{ij}}{\frac{n\cdot(n+1)}{2}} \qquad \overset{n=25}{\longrightarrow} \qquad \overline{r} = \frac{\sum_{i=1}^{24}\sum_{j=i+1}^{25} r_{ij}}{300}, \tag{15}$$

is calculated, with r_{ij} being the Euclidean distance between the vertices of event numbers i and j. The number 25 was chosen as a trade-off: Single real neutrino events, which should have an isotropic distribution of interaction vertices, would lead to a large increase in $\overline{r}$ for numbers much smaller than 25. For higher numbers the calculated $\overline{r}$-value may not be dominated by clustered bright sparking-events any more, but by lower energy atmospheric neutrino or muon events. The values for $\overline{r}$ have been calculated for 13,263 physics runs from 2007–2013 and the distribution of the resulting values for $\overline{r}$ shown in Fig. 14 is Gaussian around 192 m with a root mean square (RMS) width of 20.3 m. Runs with $\overline{r} < (192\,\mathrm{m} - 5 \times \mathrm{RMS}) \approx 90\,\mathrm{m}$ are marked as clearly sparking and are not analysed. The distributions of the Dusj vertex positions and the number of used hits for all runs identified as sparking are given in Sec. D.4. As a cross-check $\overline{r}$ was determined also for 2007–2011 runs that are confirmed to be sparking (listed in Sec. D.1). Many data-files of these heavily sparking runs are not available, because the high number of shower events could not be processed any more. The $\overline{r}$–distribution for the rather weakly sparking ones is indicated in green in Fig. 14. It can be seen that part of these are clearly sparking, but also part of them are not sparking frequently of brightly enough to be identified by a small average pairwise distance.

The center of the cluster, which is obtained by averaging over the 25 event positions, is always in proximity to a storey and can help localising the problematic OM, as is clear from the xy–projection in Fig. 15.

In addition to the runs found to be sparking already by other analyses[8], 31 runs[9] are newly identified as sparking thanks to their low average pairwise distance $\overline{r}$. It is interesting to see that some of these runs identified have subsequent run numbers[10]. This indicates that it might rarely occur that a PMT is in a flashing state even for periods as long as a day, probably multiple times for a short duration within this time range. While all three runs for 2013 identified in the point-source analysis using tracks and showers are also clearly identified by this method, it is clear from the runs identified as sparking in previous years that a single method does not find all problematic runs. Some problematic runs might still be undetected and above all it is not excluded that a PMT might spark only once. To prevent such events from entering the data analysis, an additional selection cut will exclude events which look more shower- than track-like. This cut is introduced in Sec. 4.3

[8] A complete list is given in Sec. D.1.

[9] See Sec. D.2 for a list. Runs with $\overline{r}$ in the range of $3 - 5 \times$ RMS below the mean are listed in Sec. D.3.

[10] The acoustic runs of the AMADEUS project [45] as part of the ANTARES detector also obtain run numbers. Hence, ANTARES data-taking run numbers may differ by more than one although the runs are indeed consecutive.

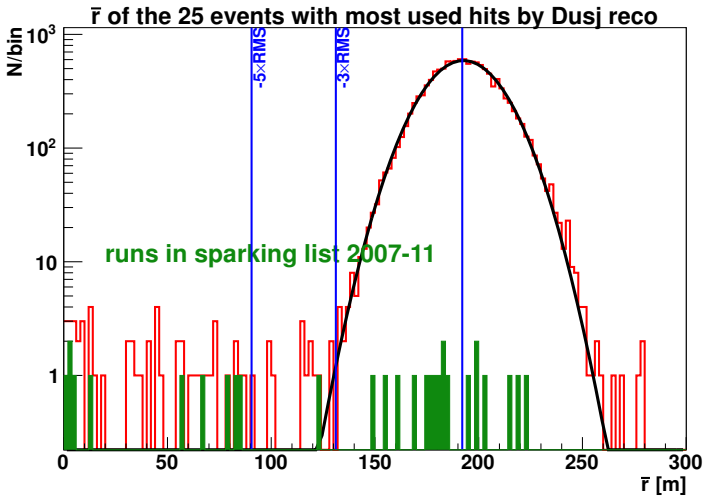

Figure 14: Runs are identified as sparking, if the average pairwise distance $\overline{r}$ of the 25 events with most number of hits used by the Dusj shower reconstruction algorithm is very low. Runs with $\overline{r} < \mathrm{MEAN} - 5 \times \mathrm{RMS}$ are clearly sparking. Normal runs are well fit by a Gaussian (black line) with a mean of 192 m.

4.2.4 | Agreement of measured and simulated muon rates

In the 4–year analysis only runs have been selected, where the amount of reconstructed atmospheric muons is in agreement with the expectation from the run-by-run Monte Carlo simulation. For the comparison all events with an AaFit track-fit quality of $\Lambda > -6.5$ triggered by the 3N, T3, T2 and TQ triggers were selected. Here only atmospheric muons are used to calculate the ratio since the contribution from neutrinos is negligible compared to the muon flux if no additional cuts are applied. A weak cut on Λ is necessary to exclude random coincidences, which occur during data-taking periods when the optical background rates are high. This feature is seen in the Λ-distribution in Fig. 16 (right) for a sample of runs recorded in 2013. Also, from comparing the two plots in Fig. 16, one clearly sees that the agreement between data and Monte Carlo is very good for runs in 2010. For 2013 however, a deficit of events is seen in the data. A loss in this ratio of measured to simulated muons has already been observed in the 4–year analysis. There it was decided to exclude runs where the ratio is more than 3σ from the fitted exponential loss of 6% per year (see Fig. 17). At present, the reason for the loss is not fully understood, but it was suspected that the transmission of light through the OMs' glass might be reduced due to sedimentation of dirt particles or adherence of bacteria (bio-fouling) [18].

Also in 2012 and 2013 data a continuing loss in data is observed as shown in Fig. 18. The 4–year analysis used version 2 of the run-by-run simulation (Fig. 18, red), which is only available for data before December 2012. Since a large part of the new data will be from 2013, this analysis uses the most recent Monte Carlo, i.e. version 3 (Fig. 18,

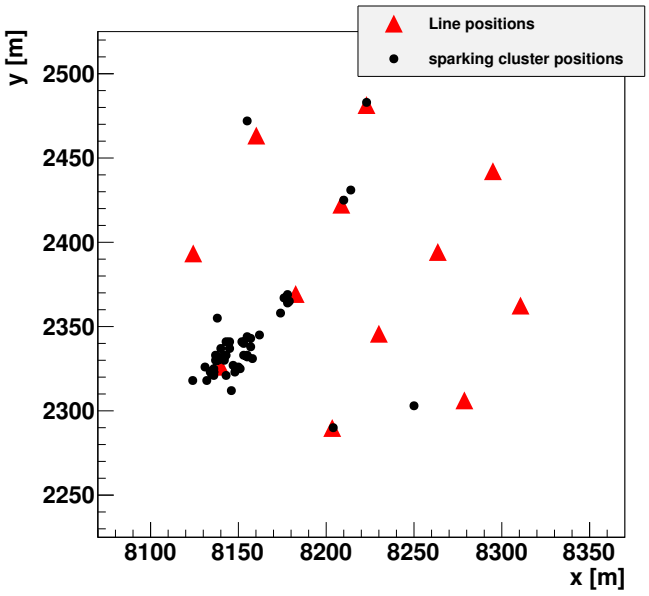

Figure 15: The cluster positions (black dots) of the sparking runs from Sec. D.2 are all close to the position of a detection line (red triangles). Especially ANTARES line 11 in the lower left of the plot contains PMTs which tend to be sparking frequently.

blue). A zoom to the time range around early 2010, which had processing problems in the 4–year analysis (Fig. 18, green), shows that the reprocessed data has a stable ratio of data and Monte Carlo. The other eye-catching feature is that the ratio of data to Monte Carlo for the run-by-run version 3 is constantly below the one for version two. The large difference at this lowest cut stage comes from major changes in the Monte Carlo between these versions. The most important modifications are [46]:

- The medium of photon generation and propagation was changed from pure water to denser sea water.
- Several improvements in accuracy related to interpolation and histogramming were implemented.
- An updated model for the PMT simulation was used (angular efficiency and glass properties were changed).
- The scattering behaviour of light now includes wavelength dependence.
- Showers are simulated more accurately with a multi-particle approximation.

A closer comparison of the simulated event numbers for the two Monte Carlo versions (see Fig. 19) shows that using version 3 (RBR V3) instead of version 2 (RBR V2) increases the number of reconstructed atmospheric muons by 33% at this low cut stage. Also, this factor is constant over the whole period where a version 2 simulation is available.

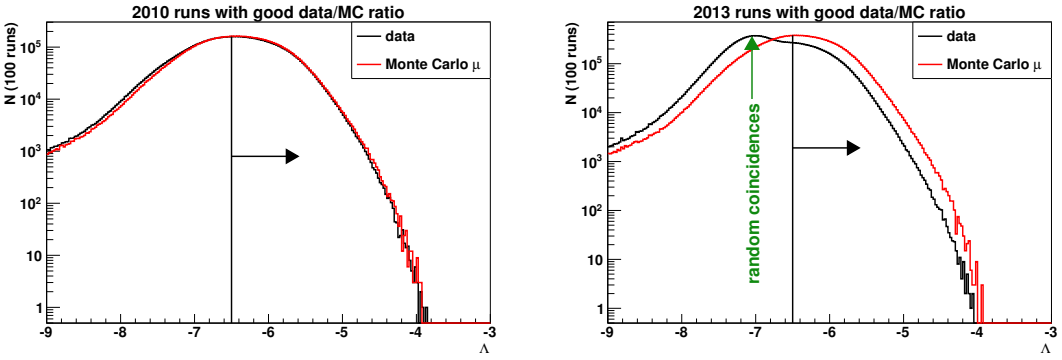

Figure 16: Distribution of the track-fit quality Λ for samples of 100 runs in 2010 (*left*) and 2013 (*right*) selected to have a normal data to Monte Carlo ratio. Except for periods of low optical background rates, events may be reconstructed from purely random coincidences with $\Lambda \lesssim -6.5$. Comparing the above plots a loss in data is evident in 2013.

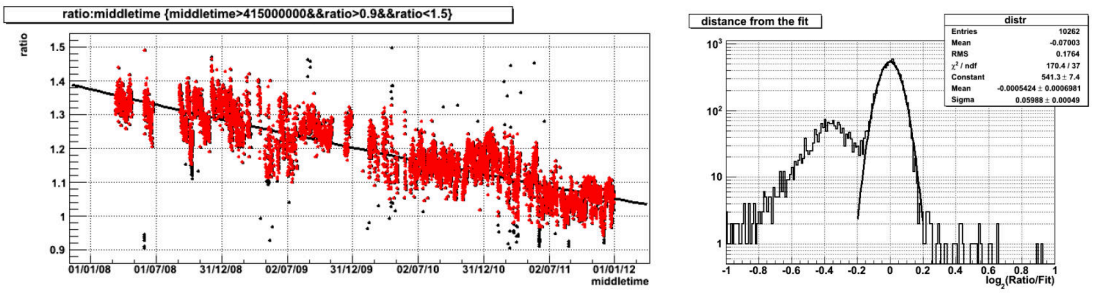

Figure 17: *Left:* Ratio of measured data events to simulated atmospheric muons in the 4–year analysis. The runs within 3σ from the exponential fit are selected for the analysis (red). *Right:* Distribution of the distance to the fit. Runs within $3\sigma = 0.18$ of the Gaussian fit are selected. Both figures taken from Ref. [18, C. 4.3.2].

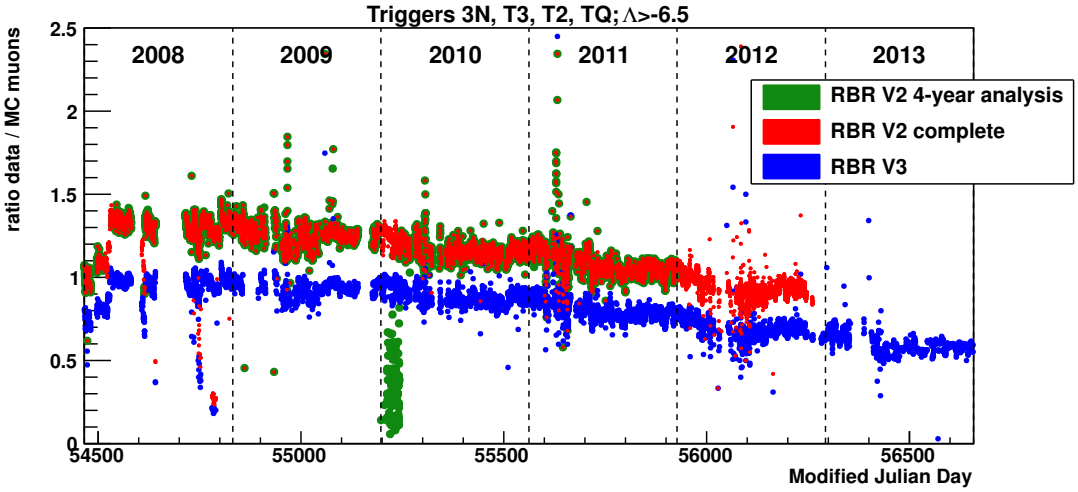

Figure 18: Run-wise ratios of event numbers in the data file and the corresponding muon Monte Carlo simulation. Events are triggered with the same triggers that are also used in the analysis and a cut on the track reconstruction quality $\Lambda > -6.5$ is applied. Ratios are shown for the version of the run-by-run simulation used in the 4–year analysis (RBR V2), and the latest version (RBR V3). *Top:* Period from January 2008 to December 2013. *Right:* Zoom in to the period with data-production problems at the time the 4–year analysis was done.

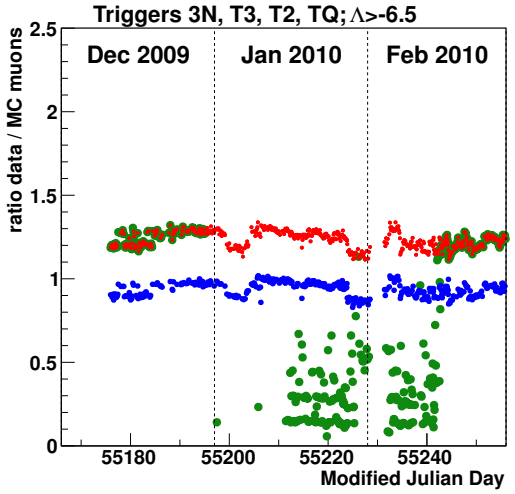

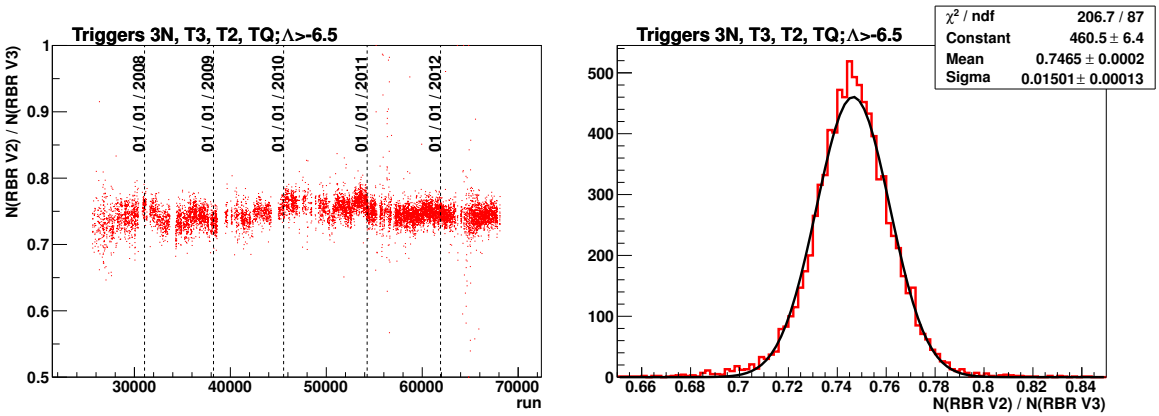

Figure 19: In the newer version of the run-by-run Monte Carlo (RBR V3), the number of simulated events for each run which are reconstructed by AaFit with $\Lambda > -6.5$ is increased by 1/3 compared to the previous version (RBR V2).

For the runs from the 2010 period, the old selection criterium for a good data – Monte Carlo agreement is re-used: The fit ratio $\mathcal{R}$ is an exponential function,

$$\mathcal{R} = \exp\left[A + B \cdot (t/1\ \mathrm{MJD})\right], \tag{16}$$

and for the runs used in the 4–year analysis the fit values determined for the RBR V2 simulation are

$$A = (10.3 \pm 0.2), \quad B = (-1.82 \pm 0.03) \times 10^{-4} \qquad (2008 - 2011, \mathrm{RBR\ V2}), \tag{17}$$

which is a loss of $1 - \exp(-1.82 \cdot 10^{-4} \times 365.25) = 6\%$ per year. With the scaling factor of 0.746 determined in Fig. 19, this can be simply rescaled for the RBR V3 simulation to:

$$A = (10.0 \pm 0.2), \quad B = (-1.82 \pm 0.03) \times 10^{-4} \qquad (2008 - 2011, \mathrm{RBR\ V3}) \tag{18}$$

Here again, as in the 4–year analysis a run is selected, if

$$\log_2(\mathrm{ratio}/\mathcal{R}) \leq 0.18 \qquad (\mathrm{for}\ 2008 - 2011), \tag{19}$$

and only six runs fail to meet this selection criterium for the 2010 period.

It turns out that the loss of 6% per year observed in the 4–year analysis has increased during the last years and the fit cannot be extapolated to 2012 and 2013 data. Re-fitting an exponential loss to the period from 2011 to 2013, the loss in this period is 14% per year (see Fig. 20). The precise fit values are

$$A = (22.3 \pm 0.3), \quad B = (-4.05 \pm 0.05) \times 10^{-4} \qquad (2011 - 2013, \mathrm{RBR\ V3}). \tag{20}$$

Plotting the distance of individual runs from the fit (Fig. 21) shows two peaks, centered at -0.040 and +0.075. This indicates that the data – Monte Carlo ratio for the data-runs has two levels. This might be due to the amount of bioluminescent background in

a run or depend on which of the used triggers were active during data-taking, but was not investigated further. Instead, the selection criterium was changed and the distance to the closest of the two peak values, -0.040 and +0.075, was used. This is similar to splitting the runs and fitting two exponential functions with the same loss, except that it is not determined which run belongs to which level. As can be seen from Fig. 22, this distribution looks much more Gaussian, although the procedure of taking the distance to the closest of the two peaks suppresses the amount of outliers, and thus narrows down the width of the distribution. A reasonable choice is therefore to re-use the value of 0.18 as maximum distance to be accepted, or equivalently

$$-0.22 \leq \log_2\left(\text{ratio}/\mathcal{R}\right) \leq 0.255 \qquad \text{(for } 2008-2011\text{)}. \tag{21}$$

This requirement excludes 91 runs in the new dataset. A full list of all runs excluded due to bad agreement of data and Monte Carlo is given in Appendix E.

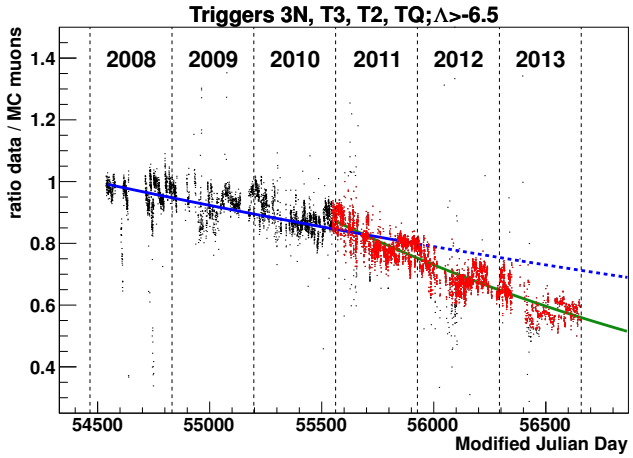

Figure 20: The exponential decrease of $\approx$ 6% in the ratio of observed to simulated (RBR V3) events per annum for 2008–2011 data (blue line) cannot be extrapolated to 2012/13. Instead a steepening in 2011 is observed. A new fit (green line) from 2011 to 2013 yields an exponential decrease of 14% per year. Red points are runs that are accepted for the analysis thanks to their proximity to the fit.

4.3 | Event pre-selection

For the analysis update the event pre-selection is adopted from the 4–year analysis. As stated previously, the track analysis uses events reconstructed with the AaFit track-fit algorithm. As energy estimator the ANN is used.

Events are required to pass all of the following pre-selection cuts in order to enter the final event selection:

1. arriving from the on- or one of the off-zones:
   Only events coming from the approximated shape of the Fermi Bubbles or one of the regions for background determination are selected.

2. BBFit $\chi^2_{\text{track}} < \chi^2_{\text{point}}$:
   BBFit [47] *is an alternative* χ^2*–based fitting algorithm. It fits both a track hypothesis* (χ^2_{track}) *and a shower hypothesis* (χ^2_{point})*, i.e. emission of the light from a*

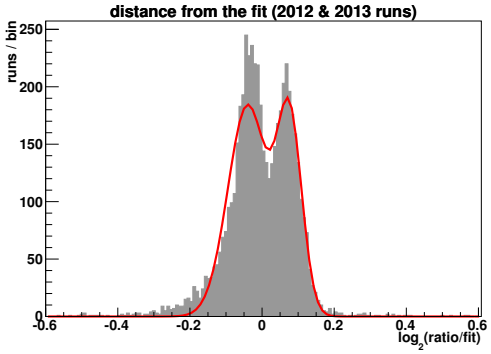

Figure 21: Distance from the observed ratio of data to RBR V3 muons for 2012 and 2013 runs. Two peaks at -0.075 and +0.04 are observed. The red line shows the fit of a double-Gaussian.

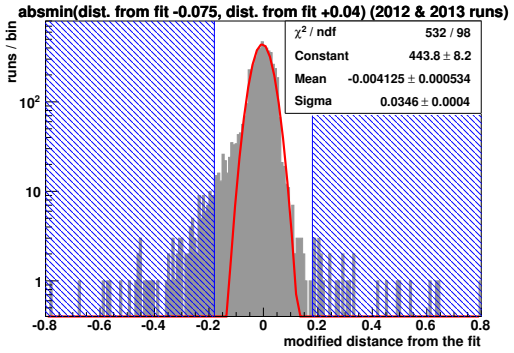

Figure 22: The distance to the closer of the two maxima ($\log_2$(ratio/fit)-0.075, $\log_2$(ratio/fit)+0.04) in Fig. 21 is rather Gaussian (red line) distributed. The procedure suppresses outliers, hence instead of $3\sigma \approx 0.1$ from the fit, the value of the 4–year analysis is used, which excludes runs with a modified distance of larger than 0.18 to the closer level.

point source. Selecting only $\chi^2_{\text{track}} < \chi^2_{\text{point}}$ *suppresses events which appear shower-like. It was shown* [18]*, that this cut also very efficiently removes sparking events that might still be present in the data-set after the removal of sparking runs in Sec. 4.2.3.*

3. nUsedHits$_{\text{AaFit}} > 10$:
   This cut admits only events where AaFit has used more than 10 hits to fit the track. This ensures a stable fit result and also suppresses background.

4. AaFit zenith $\theta > \pi/2$:
   Only events that are recontructed as up-going are selected to reject most of the atmospheric muons, which despite the overburden of sea water still dominate over the neutrino signal by six orders of magnitude in ANTARES.

5. AAFit $\beta < 1°$:
   The cut on the angular error estimate β *of the AaFit reconstruction deselects events with misreconstructed direction.*

The track-fit quality Λ is very efficient to suppress atmospheric muons, and therefore one of the parameters the final cut optimisation will be done on. However, for the comparison of data and Monte Carlo (Sec. 4.4) the following pre-selection cut will be also applied:

6. AaFit $\Lambda > -6$:
   The loose cut on the AaFit track-fit quality, Λ*, is mainly to exclude pure noise events that are not simlated but present in the measured data.*

4.4 | Data ↔ data and data ↔ Monte Carlo checks

Using the events passing the pre-selection above in Sec. 4.3, it is necessary to make several quality checks before moving on with the final event selection and the unblinding of the data-set. These checks validate the analysis method of using on- and off-zones (Sec. 4.4.1), and ensure that the data agrees well with the expectation from the run-by-run simulation (Sec. 4.4.2).

4.4.1 | Validation of the on-/off-zone choice

In Sec. 4.1 it was argued that the visibility for the different zones equalise over time. If this really is the case for the used data-set needs to be checked.

To this end, the number of events coming from each of the three off-zones is compared by calculating the difference (cf. [18])

$$\mathrm{diff}_{ij} = \frac{N_i - N_j}{\langle N_{\mathrm{off}} \rangle} \times 100\% \tag{22}$$

for the pairs of zones (i,j)=$\{(1,2), (2,3), (3,1)\}$. Here $\langle N_{\mathrm{off}} \rangle = \sum_{i=1}^{3} N_i/3$ is the average number of events observed per off-zone. This difference is calculated for all possible combinations of equally spaced cuts on the range of track fit quality, $\Lambda^{\mathrm{cut}} = -6 \ldots -3$, and the reconstructed energy, $\log_{10}\left(E^{\mathrm{cut}}_{\mathrm{ANN}}[\mathrm{GeV}]\right) = 2 \ldots 6$ as shown in Fig. 23.

It can be seen that most of the points lie within the grey shaded band, which represents the 68% statistical error band. The error band is obtained via propagation of a $\sqrt{N}$ error on the number of events for each of the three zones in Eq. 22. More intuitively, 68% of the measured diff_{ij} would lie within this region when drawing i and j randomly from a Poissonian distribution around a mean $\langle N_{\mathrm{off}} \rangle$ (black dashed line). The line-like structures in Fig. 23 originate from the fact that two very similar pairs of cuts ($\Lambda^{\mathrm{cut},1} \approx \Lambda^{\mathrm{cut},2}$, $E^{\mathrm{cut},1}_{\mathrm{ANN}} \approx E^{\mathrm{cut},2}_{\mathrm{ANN}}$) will select almost the same set of events, and therefore will also have a similar asymmetry. Anyway, since the majority of points lies within the statistical error, it can be concluded that the visibility for the three off-zones is similar. For a broad range of cuts (region $\langle N_{\mathrm{off}} \rangle \lesssim 500$) slightly more events are seen in off-zone 3 than in the other two.

A similar difference can be calculated between the on-zone and the average from the off-zones. However, since this analysis uses a blind-strategy, the quantity is calculated with the run-by-run simulation for atmospheric neutrinos instead of real data (cf. [18]):

$$\mathrm{diff}_{\mathrm{on/off}} = \frac{N^{\mathrm{MC}}_{\mathrm{on}} - < N^{\mathrm{MC}}_{\mathrm{off}} >}{< N^{\mathrm{MC}}_{\mathrm{off}} >} \times 100\%. \tag{23}$$

The same range of cuts on Λ and E_{ANN} as for the comparison amongst the off-zones is used to plot the asymmetry between on- and off-zones in Fig. 24. Here again, the grey band represents the statistical error, which is based on the event weights of the run-by-run MC simulation. This is why the error band is much narrower for the difference between on- and off-zones (Fig. 24) than for the comparison amongst the off-zones using real data (Fig. 23). Fig. 24 shows that $\approx$ 4% more events are seen in the on-zone

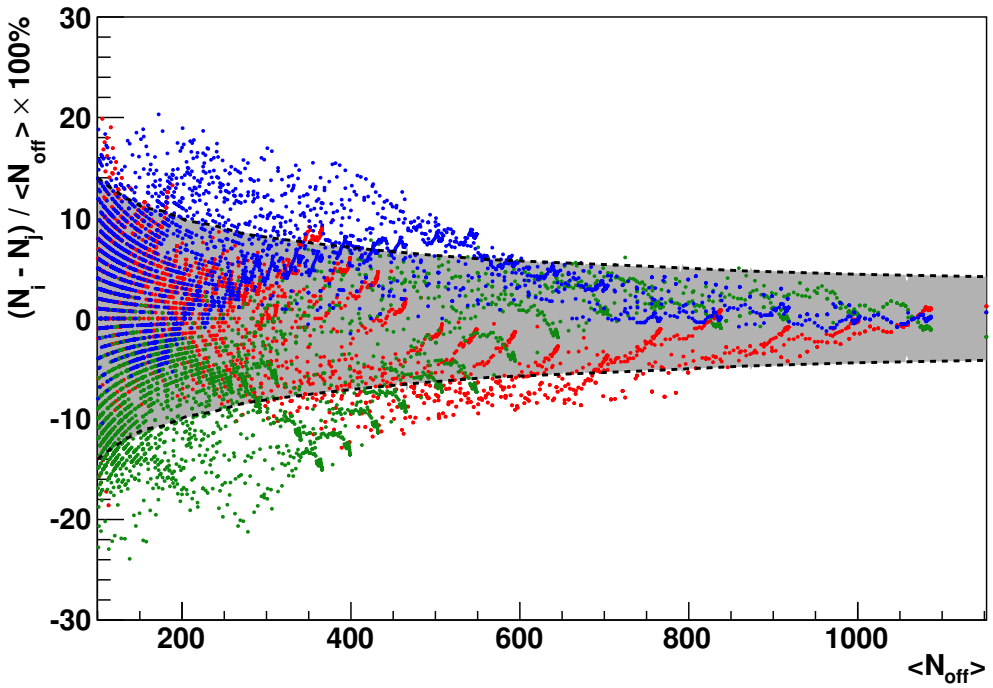

Figure 23: Difference between data events from the different off-zones for cuts on Λ and $\log_{10}(E_{\mathrm{ANN}})$. Most of the points lie within the 1σ statistical error band (grey area). Colors indicate pairs of zones – *red:* (i,j) = (1,2), *green:* (i,j) = (2,3), *blue:* (i,j) = (3,1).

compared to the off-zones for the various cuts. This small excess is however still at the edge of the statistical error band. In summary, it is expected that the background contribution is similar for all off-zones and also the on-zone for the analysis update.

In addition, it is favourable to avoid an overlap of the off-zones with possible extended neutrino sources. A recent ANTARES search [42] for a neutrino flux from a bar around the Galactic Centre and a circular region around an overfluctuation seen in the 3–year IceCube high energy starting events (HESE) analysis [48] has also used on- and off-zones for the signal search. Here, the FB off-zones do not overlap with the signal regions, and the overlap of the signal regions in both analyses is small. On top of this, no excess over the background expectation was found in the Galactic Centre and the IceCube 'warm spot' [42]. The 'Model-independent search for neutrino anisotropies with the ANTARES neutrino telescope' looks for an excess in neutrino events in clusters of all sizes and preliminary results are presented in Ref. [49]. The region containing the most significant (2.5σ) cluster has a vast extension of ≈ 1.3 sr on the southern sky. It is reassuring that the off-zones in the FB analysis have only small overlap with the structure – 0.03 sr for off-zone 1 and 0.09 sr for off-zone 3. The overlap with the on-zone is 0.2 sr, but it must be stated that the major part of the events used for the multiscale-search was of lower energies than the ones used in the FB analysis. No problematic overlap with previous

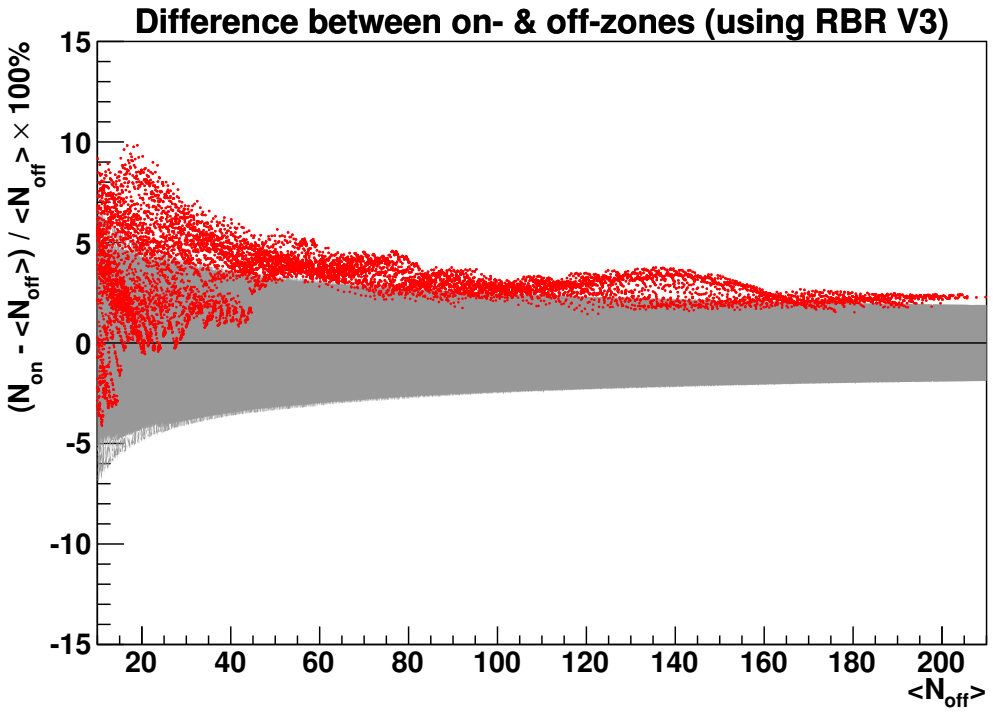

Figure 24: Difference between simulated neutrinos from the on-zone and the average of the three off-zones for cuts on Λ and $\log_{10}(E_{\mathrm{ANN}})$. The statistical error band is indicated in grey.

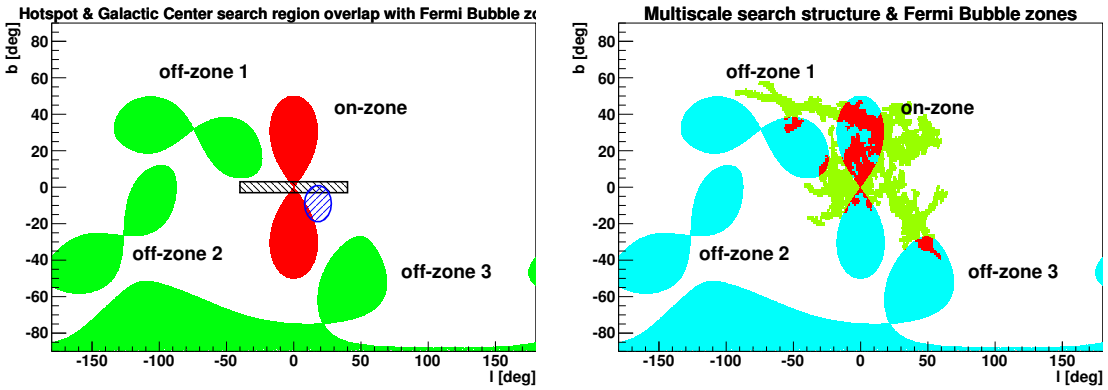

Figure 25: Overlap of the ANTARES zones with different extended source regions. *Left:* Galactic Center search region ($|l| \leq 40°$, $|b| \leq 3°$) and IceCube 'warm spot' (radius of $10°$ around $l = 18°$, $b = -9°$) [42]. *Right:* Most significant structure found in a recent multiscale source search [49].

extended source searches is thus found.

4.4.2 | Data/MC checks and reweighting of Monte Carlo

Re-weighting of the atmospheric muon simulation: From the data agreement with Monte Carlo in the run selection (Sec. 4.2.4), it is apparent, that the number of reconstructed atmospheric muons will drop for the 2012 and 2013 data. The amount of this drop has been calculated in a dedicated analysis that derived the loss in quantum efficiency from the decrease in the ^{40}K background coincidence rate [50]. This resulted in a formula for down-weighting the MUPAGE weight of 3 per simulated muon by the multiplicative factor

$$w_{\mathrm{QE}} = 3.622 - 3.985 \cdot 10^{-5} \times \mathrm{RUNNUMBER}, \tag{24}$$

for run numbers greater than 68306. In this analysis Eq. 24 was used for reweighting the muon simulation for run numbers greater than 68306. For lower run numbers a constant factor of 0.9 was applied to allow for a smooth transition of this re-weighting. This additional weight factor is also presented in Fig. 26. From the Λ-distribution in the off-zones after the event pre-selection in Fig. 27, it can be seen, that at low Λ values the MUPAGE expectation – even with this factor applied – still overestimates the measured contribution of atmospheric muons. A change from the main component of the atmospheric background from muons to neutrinos is seen at $\Lambda \approx -5.2$. Since an incomplete compensation of the difference in simulated and observed muons only results in a more conservative estimate on this background, and the final selection will cut almost all muons away, the re-weighting derived from the quantum efficiency studies is used without further modification.

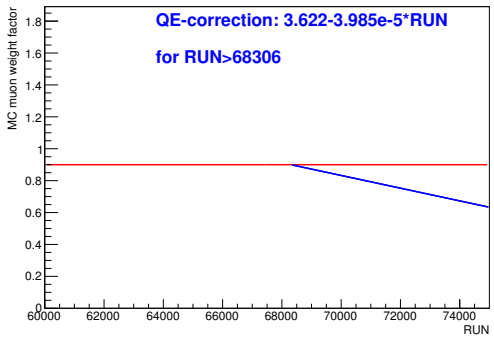

Figure 26: The additional weight factor applied to MUPAGE muons is 0.9 for runs<68306 (red) and the value from the QE-correction formula in Eq. 24 beyond (blue).

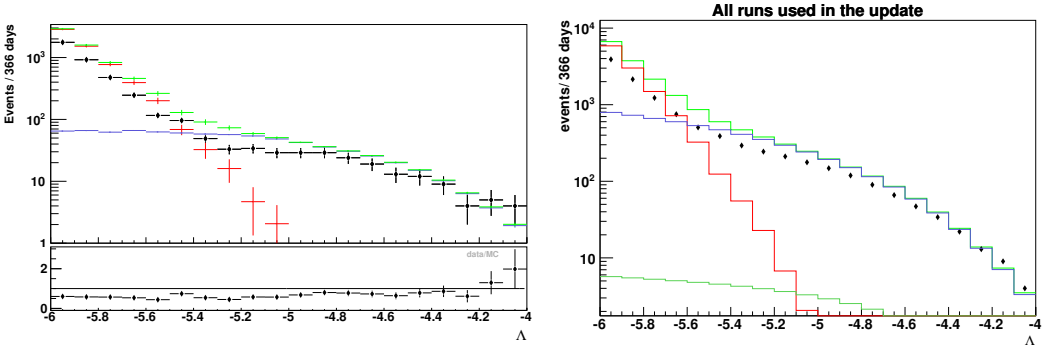

Figure 27: Λ distribution (*left:* normal, *right:* cumulative) of the whole dataset used for the analysis update. All events coming from the off-zones with the pre-selection applied are shown in black. Atmospheric muon (red) weights are quantum-efficiency corrected. Nominal Monte Carlo weights are used for atmospheric neutrinos (blue). The sum of atmospherics is shown in light green. The additional green line in the lower part of the cumulative distribution represents the level of a simulated E^{-2} FB flux.

Lambda distribution For the whole time period, also less atmospheric neutrinos are reconstructed than is expected from the run-by-run simulation (compare the central part of the cumulative plot in Fig. 27). This is most easily seen in the cumulative distribution, where the content of each bin i is the sum over all bins j with $j \geq i$.

It is interesting to see, if this drop is present for all the data used in the analysis. To this end, the dataset is split into three parts, and the distribution is shown for each year – 2010, 2012 and 2013 – separately in Fig. 28.

It is apparent that the agreement between data and Monte Carlo, whilst good for $\Lambda > -5.2$ in 2010, gets worse in 2012 and 2013. The overfluctuation for large Λ values in the cumulative distribution for 2012 is due to the overfluctuation in the uppermost bin. Besides this, the 2012 and 2013 distribution constantly observe less data than expected. For this analysis, it has been decided to rescale the 2012 and 2013 Monte Carlo to match the measured flux for $\Lambda > -5.1$ by a constant factor. A more detailed study of the origin and evolution of this loss would involve reproducing part of the Monte Carlo simulation

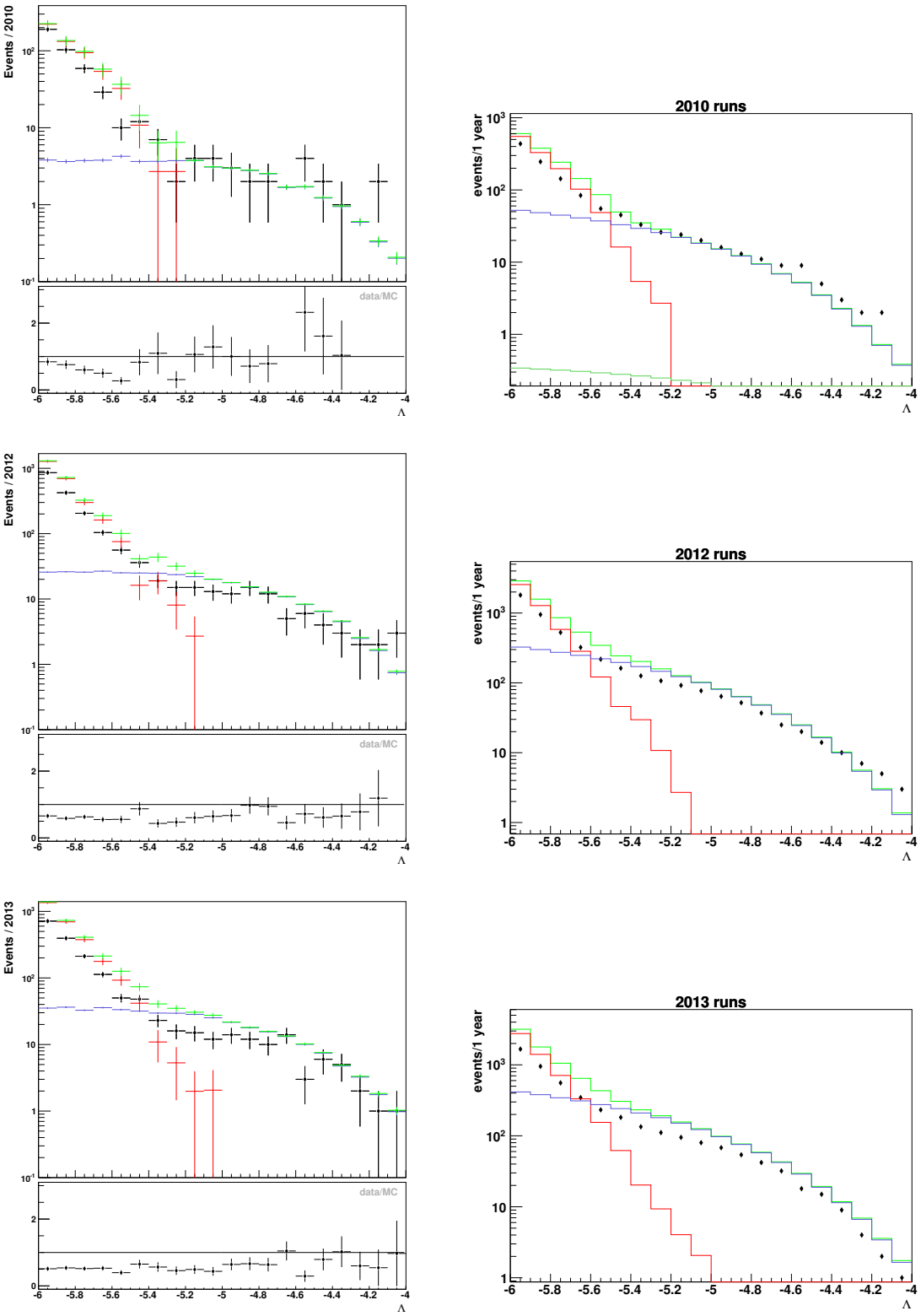

Figure 28: Distribution for Λ with the original Monte Carlo weights for each year separately. *Left:* normal, *right:* cumulative. See caption of Fig. 27 for a detailed description.

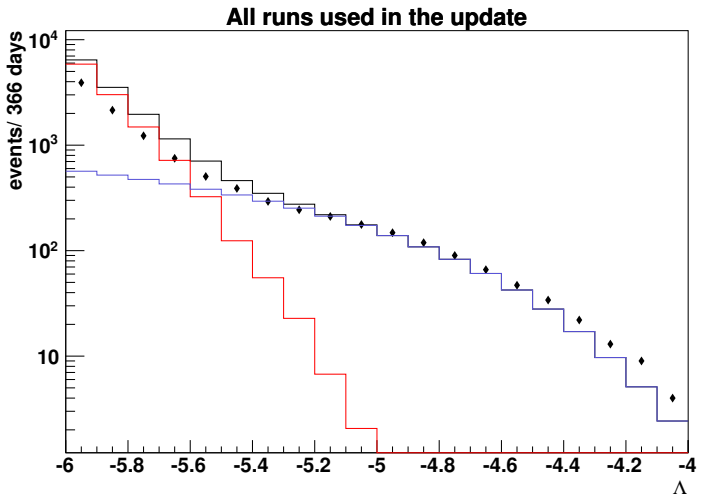

Figure 29: Cumulative distribution for Λ after rescaling the 2012 and 2013 Monte Carlo weights by 0.7. Red: atmospheric muons, blue: atmospheric neutrinos, black line: sum of MC, diamonds: data.

with varied parameters for the quantum efficiency. This is desirable for the future, but beyond the scope of this thesis. Also, since the estimated loss from the quantum efficiency studies on a neutrino signal is only 3% [50], no re-scaling is used for the simulated FB flux in this analysis. The **rescaling factor for the 2012 and 2013 atmospheric neutrino simulation** is determined to be **0.7**. This factor gives a data to Monte Carlo ratio of 1 in the cumulative distribution at $\Lambda = -5.1$. The cumulative distribution after this rescaling is shown in Fig. 29. The rescaling is still within the uncertainty on the Bartol flux normalisation, which is of the order of $\approx \pm 30\%$. However, also the 4–year analysis has used a constant factor to tune the Monte Carlo [18, Sec. 5.4]. Although this used RBR V2 Monte Carlo and a direct comparison of the numbers may not be strictly correct, the Monte Carlo neutrinos had to be scaled up by 23%. This emphasises even more that there is a loss seen in the atmospheric neutrinos over the years.

ANN energy distribution In the 4–year analysis (cf. [18, Sec. 5.4]), the comparison of measured and simulated data has shown, that the distribution for the simulated neutrino flux is shifted to lower energies. This can be compensated by shifting the simulated flux by +0.1 in logarithmic scale of the reconstructed ANN energy to obtain the reconstructed energy

$$\log_{10}\left(E_{\text{reco}}\,[\text{GeV}]\right) = \log_{10}\left(E_{\text{ANN}}\,[\text{GeV}]\right) + 0.1. \tag{25}$$

Since the 4–year analysis has used RBR V2 Monte Carlo, but RBR V3 is used here, it needs to be checked if this shift is still applicable. The cumulative distributions of the

reconstructed energy for the data and the simulated shifted neutrino background in the three off-zones agree well after the rescaling of the neutrino flux by 0.7 (see Fig. 30).

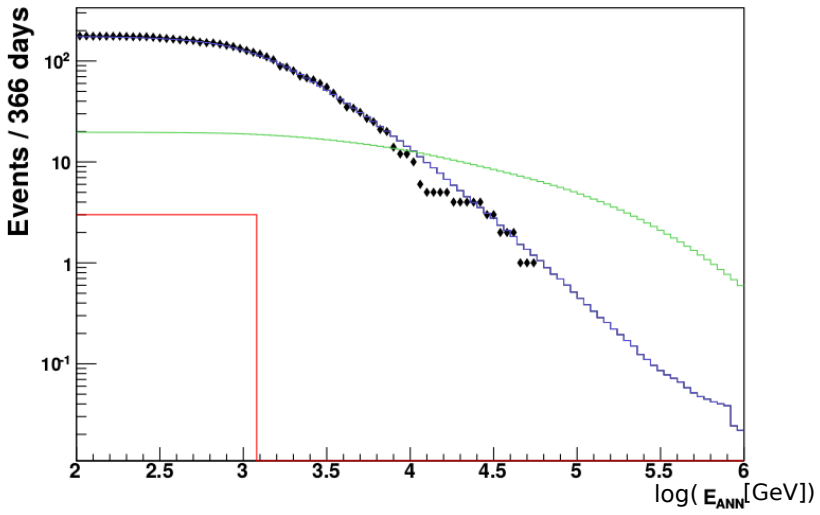

Figure 30: Distribution of the reconstructed energy for $\Lambda > -5.1$. Blue: atmospheric neutrinos, red: atmospheric muons. The lower bound of the expected FB flux for an E^{-2} spectrum and no cut-off, scaled by a factor of 3 to allow for easy comparison with the offzones, is also indicated (green). The Monte Carlo distribution is shifted by +0.1 in log-scale.

The scaled and shifted off-zone distributions for Λ and E_{reco} shown in Fig. 31 have a good agreement of data and Monte Carlo. As stated above, the Λ distribution has a dominating contribution of atmospheric neutrinos for $\Lambda \lesssim -5.2$. Similarly, the reconstructed energy shows a transition from atmospheric neutrinos to a FB signal in the region above 10 TeV, depending on the assumed FB spectrum. For this reason, the final cut optimisation is done on these two parameters in the following section, Sec. 4.5.

4.5 | Cut optimisation

In Fig. 31 it was shown that the neutrino signal from the FB tends to have a better track-fit quality Λ than the misreconstructed atmospheric muons and differs from the atmospheric neutrino flux by a harder energy spectrum, which results in higher reconstructed energies E_{reco}. Hence, the two variables are key variables for the suppression of atmospheric backgrounds.

The cut values on these two variables, the track fit quality parameter Λ^{cut} and the reconstructed energy $E_{\text{reco}}^{\text{cut}}$, are optimised to yield the best average upper limit on the signal flux. A popular method in neutrino astronomy to do this optimisation is the model rejection factor (MRF) technique [51].

However, this analysis of the 2012/13 data will later be combined with the result of the

4–year analysis. The procedure described in Ref. [51] is therefore extended to account for the result of this initial analysis as follows. The first measurement has observed $N_{\mathrm{on},1} = 16$ events in the on-zone and an average background of $\overline{N}_{\mathrm{off},1} = 11$ events in the three off-zones. The optimal cut values for the new data are obtained by minimising the average upper limit on the signal flux:

$$\overline{\Phi}_{90\%} = \Phi_{\mathrm{model}} \frac{\overline{s}_{90\%}(b_2|N_{\mathrm{on},1}, \overline{N}_{\mathrm{off},1})}{s_1 + s_2} = \Phi_{\mathrm{model}} \times \mathrm{MRF}, \tag{26}$$

where $s_1 + s_2$ is the number of simulated signal events that originates and is reconstructed within the on-zone in the whole data taking period used for the initial analysis (s_1) and the update (s_2). The signal flux was simulated with the assumed neutrino fluxes Φ_{model} from Eq. 8. For a known mean number of simulated background neutrinos from the off-zones in the new dataset, b_2, an average over the 90% confidence level Feldman&Cousins [52] upper limits, $\mu_{90\%}$, can be calculated as

$$\overline{s}_{90\%}(b_2|N_{\mathrm{on},1}, \overline{N}_{\mathrm{off},1}) = \sum_{k=0}^{\infty} \mu_{90\%}(k + N_{\mathrm{on},1}, b_2 + \overline{N}_{\mathrm{off},1}) \times \mathrm{Poisson}(k|b_2). \tag{27}$$

This is an average over all possible numbers of events k observed in the on-zone weighted by the according Poisson probability of observing k events given the background b_2. The value $\mu_{90\%}(N_{\mathrm{observed}}, N_{\mathrm{background}})$ represents an upper limit on the number of signal events at 90% confidence level, when N_{observed} events are observed and the background contained in this observation is $N_{\mathrm{background}}$. Upper limits using Eq. 27 with $N_{\mathrm{on},1} = 16$

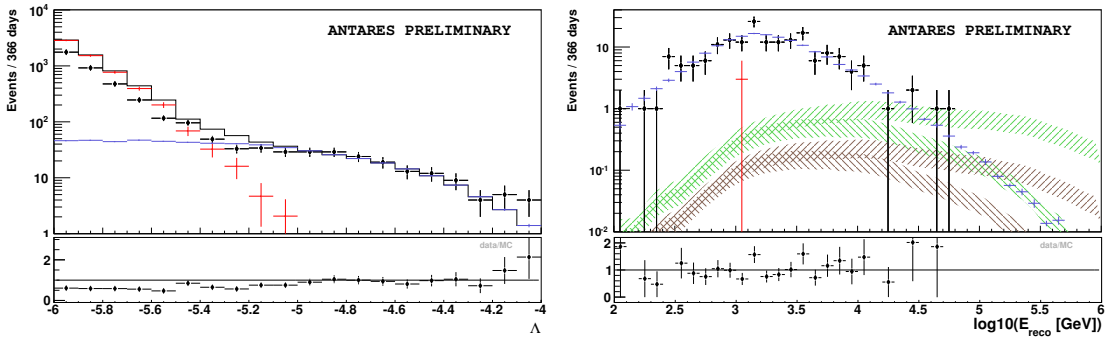

Figure 31: Off-zone distribution of Λ and E_{reco} for measured (black points) and simulated events. On the left a transition of the main contribution from muons (red) to neutrinos (blue) is seen in the track fit quality parameter at $\Lambda \approx -5.2$. On the right the distribution of the reconstructed energy for $\Lambda > -5.1$ is shown. The signal flux (scaled up by a factor of 3 for easy comparison with the off-zones) for an E^{-2} spectrum (green) and an $E^{-2.18}$ spectrum (brown) is also indicated for a 50 TeV cut-off and no cut-off . The pre-selection mentioned in the text has been used. A scaling factor of 0.7 has been applied to the atmospheric neutrino flux to allow for better agreement between measured data and simulation. Figures taken from Ref. [28].

and $\overline{N}_{\mathrm{off},1} = 11$ have been calculated using the Feldman&Cousins method of the ROOT software framework[11] and are given in Fig. 32. Setting $N_{\mathrm{on},1}$ and $\overline{N}_{\mathrm{off},1}$ to zero reduces the MRF calculation in Eq. 26 to the standard case of a single measurement developed in Ref. [51].

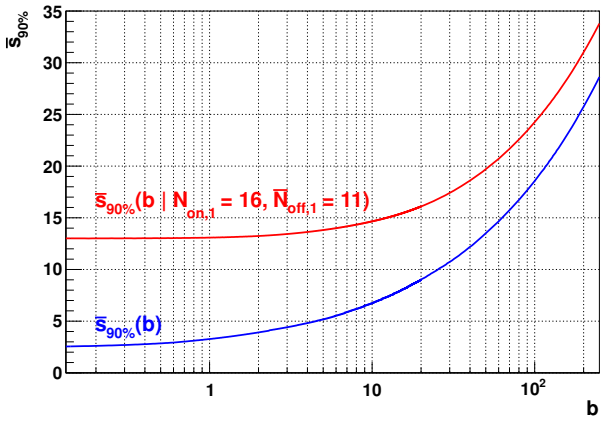

Figure 32: Average 90% signal upper limits calculated for different numbers of the mean background b. The red line is obtained for a second analysis under the condition that the initial analysis has observed $N_{\mathrm{on},1} = 16$ events in the signal region and an average of $\overline{N}_{\mathrm{off},1} = 11$ events in the off-zones (Eq. 27). The blue line denotes the average upper limit for a single analysis (i.e. $N_{\mathrm{on},1} = 0$, $\overline{N}_{\mathrm{off},1} = 0$).

MRF values (Eq. 26) are calculated for a two-dimensional range of possible cut values on Λ^{cut} and $\log_{10}(E^{\mathrm{cut}}_{\mathrm{reco}}[\mathrm{GeV}])$ and the set of cuts minimising the MRF represents the sensitivity of the ANTARES detector to the neutrino flux from the Fermi Bubbles.

For an exemplary spectral index of $\alpha = 2.0$ and a cutoff of $E_{\mathrm{cutoff}} = 500\,\mathrm{TeV}$, Fig. 33 shows the event distributions[12] of the atmospheric backgrounds (blue) and the expected signal flux (red) that survive the pre-selection (Sec. 4.3). The resulting MRF landscape for this signal spectrum is depicted in Fig. 34 and the best pair of cut values is indicated by a marker. The steplike behaviour of the MRF in the lower left part of Fig. 34 is

[11] available from https://root.cern.ch

[12] The number of bins per axis that is used for the MRF optimisation is a factor 5 higher than in Fig. 33.

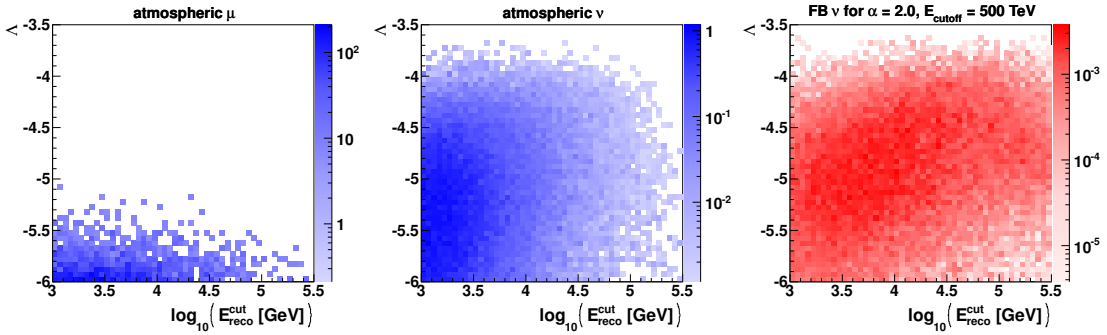

Figure 33: Background distributions of atmospheric muons and atmospheric neutrinos (*left, centre*) and distribution of signal events for a Fermi Bubble power-law flux with spectral index $\alpha = 2.0$ and cut-off $E_{\mathrm{cutoff}} = 500\,\mathrm{TeV}$ (*right*).

due to the sparse simulation of atmospheric muons in this region (as can be seen from Fig. 33). If a cut value is decreased and an additional simulated muon is accepted, the high individual event weight compared to the neutrino fluxes leads to a step-like increase of the MRF.

To obtain a conservative sensitivity, the lower bounds of the neutrino flux normalisations (Eq. 9, Eq. 10) have been used for the simulated signal. The sets of cuts (Λ^{cut}, $E^{\mathrm{cut}}_{\mathrm{reco}}$) optimising the average upper limit on the neutrino flux given in Eq. 26 and the respective flux coefficients are reported in Tab. 2 for an E^{-2} and an $E^{-2.18}$ neutrino spectrum with cut-off energies of 50 TeV, 100 TeV, 500 TeV and with no cut-off. Here, the background simulation has been reweighted as reported in Sec. 4.4.2. It has been checked (see Appendix G), that this reweighting of the background simulation does not notably change the optimal cut values. Since the MRF minimum is very shallow, the obtained MRF does not increase significantly when using only one set of cuts, the cuts for 100 TeV (second last row in Tab. 2), also for the other cut-off energies. This shows that only one unblinding for a single pair of cut values per spectral index yields an optimal result for all cut-off energies. Furthermore, it has been verified that the cut values used in the 4–year analysis yield MRF values which are close to optimal (last row in Tab. 2). Hence, the cuts of the 4–year analysis,

$$\Lambda^{\mathrm{cut}} > -5.14 \qquad \text{and} \qquad \log_{10}\left(E^{\mathrm{cut}}_{\mathrm{reco}}[\mathrm{GeV}]\right) = 4.0\overline{3}, \tag{28}$$

are also used for this analysis, which is very convenient for the comparison of the two analyses. Tab. 3 presents the number of signal events remaining for each of the spectra after applying this final set of selection cuts.

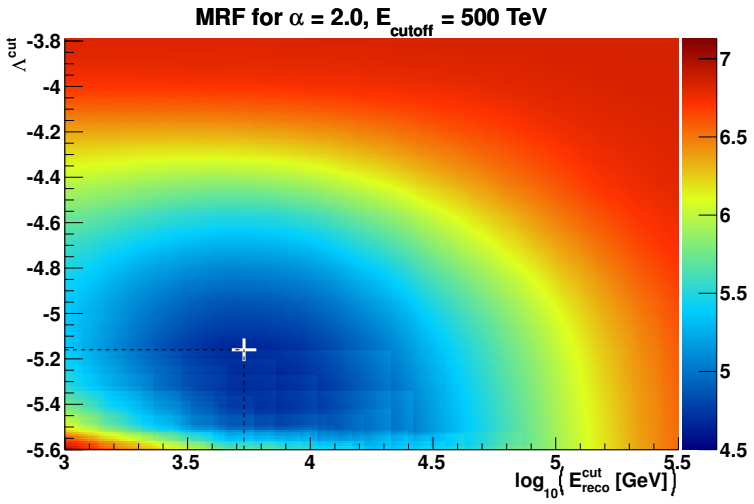

Figure 34: MRF values for different cuts on the reconstructed energy, $E^{\mathrm{cut}}_{\mathrm{reco}}$, and track fit quality, Λ^{cut} assuming a Fermi Bubble flux with spectral index $\alpha = 2.0$ and a cutoff at 500 TeV. For the optimal cut values $\Lambda^{\mathrm{cut}} = -5.16$, $\log_{10}\left(E^{\mathrm{cut}}_{\mathrm{reco}}[\mathrm{GeV}]\right) = 3.73$ a MRF value of 4.7 is obtained.

Table 2: Results for the cut optimisation for an E^{-2} ($E^{-2.18}$) neutrino spectrum on the left (right) with different cutoff energies.The coefficient for the flux sensitivity $\overline{A}^{\alpha}_{90\%}$ is given in units of $1 \times 10^{-7}\,\mathrm{GeV}^{\alpha\,-\,1}\,\mathrm{cm}^{-2}\,\mathrm{s}^{-1}\,\mathrm{sr}^{-1}$. This flux sensitivity is the obtained MRF times the model flux of Eq. 9, Eq. 10. Grey shaded numbers indicate the cut values used to calculate the 100 TeV cuts sensitivity.

	E^{-2} neutrino spectrum:				$E^{-2.18}$ neutrino spectrum:			
$E_{\mathrm{cutoff},\nu}$ [TeV]	∞	500	100	50	∞	500	100	50
Λ^{cut}	-5.34	-5.16	-5.16	-5.34	-5.16	-5.16	-5.16	-5.32
$\log_{10}\left(E^{\mathrm{cut}}_{\mathrm{reco}}[\mathrm{GeV}]\right)$	4.04	3.78	3.64	3.52	3.68	3.64	3.44	3.36
background MC	5.61	8.32	12.1	24.6	10.9	12.1	20.1	34.3
signal MC	1.6	1.2	0.81	0.74	0.36	0.29	0.24	0.23
$\overline{A}^{\alpha}_{90\%}$	3.73	5.60	9.41	13.9	29.3	38.3	59.0	78.3
Applying the cut values obtained for 100 TeV to all other cutoff energies:								
$\overline{A}^{\alpha}_{90\%}$ (100 TeV cuts)	3.83	5.65	9.41	14.1	30.5	39.3	59.7	79.2
Applying the cut values obtained in 4–year analysis to all cutoff energies:								
$\overline{A}^{\alpha}_{90\%}$ (cuts from Ref. [17])[a]	3.78	5.74	10.0	15.5	30.0	40.2	65.3	91.3

[a] $\Lambda^{\mathrm{cut}} > -5.14$, $\log_{10}\left(E^{\mathrm{cut}}_{\mathrm{reco}}[\mathrm{GeV}]\right) > 4.0\bar{3}$

Table 3: Number of signal ($N_{\mathrm{sig,MC}}$) and background ($N_{\mathrm{bgr,MC}}$) events in the run-by-run simulation passing the final selection using the analysis cuts of the 4–year analysis ($\Lambda^{\mathrm{cut}} > -5.14$, $\log_{10}\left(E^{\mathrm{cut}}_{\mathrm{reco}}[\mathrm{GeV}]\right) > 4.0\bar{3}$).

	$N_{\mathrm{sig,MC}}$, E^{-2} spectrum				$N_{\mathrm{sig,MC}}$, $E^{-2.18}$ spectrum				$N_{\mathrm{bgr,MC}}$
$E_{\mathrm{cutoff},\nu}$ [TeV]	∞	500	100	50	∞	500	100	50	
2008–2011 RBR V2[a]	2.9	1.9	1.1	0.7	–	–	–	–	–
2008–2011 RBR V3	2.93	1.93	1.08	0.72	0.55	0.41	0.25	0.18	(not calc.)
2012–2013 RBR V3	1.42	0.94	0.53	0.35	0.27	0.20	0.13	0.09	4.10

[a] Numbers taken from [18, Tab. 5.2].

Table 4: Parameters of the 22 neutrino candidates found in the on-zone for 6–years of ANTARES data.

#	run	date	Λ	logE[a]	(l,b)
1	35246	2008-09-10	-3.95	4.14	(12, 30)
2	35583	2008-09-22	-4.81	4.98	(-12, -18)
3	36471	2008-10-17	-4.86	4.41	(9, 38)
4	36908	2008-11-07	-5.02	4.19	(1, 41)
5	38756	2009-01-28	-4.13	4.23	(15, 19)
6	38791	2009-01-31	-4.72	4.31	(15, 23)
7	40917	2009-05-20	-4.89	4.37	(-4, 25)
8	43555	2009-10-01	-4.46	4.09	(6, -35)
9	44124	2009-10-28	-4.93	4.92	(0, 43)
10	46640	2010-02-17	-4.77	4.10	(11, 30)
11	47870	2010-04-07	-4.57	4.19	(-9, -26)
12	53563	2010-12-02	-5.03	4.26	(3, 43)
13	53804	2010-12-13	-4.83	4.3	(5, -28)
14	54210	2010-12-29	-4.07	4.75	(10, -29)
15	54898	2011-01-29	-4.09	4.19	(2, -41)
16	60845	2011-11-08	-4.47	4.39	(5, 32)
17	62033	2012-01-07	-4.68	4.29	(-2, -8)
18	62477	2012-01-30	-5.14	4.32	(-2, -47)
19	66859	2012-09-23	-4.73	4.37	(-9, -23)
20	68961	2013-01-17	-4.96	4.08	(8, -38)
21	72065	2013-08-03	-4.79	4.13	(-13, -23)
22	72985	2013-10-05	-5.11	4.27	(13, -31)

[a] $\log_{10}(E_{\text{reco}}\,[\text{GeV}])$

4.6 | Analysis result

To validate the analysis chain developed for the new data-set, the 806 days of data used in the 4–year analysis are re-analysed, and the same events 16 on-zone and 33 (9+12+12) off-zone events as in the 4–year analysis are obtained.

Then, the new dataset comprising a life-time of 366 days is analysed using the cut values $\Lambda^{\text{cut}} > -5.14$ and $\log_{10}\left(E^{\text{cut}}_{\text{reco}}[\text{GeV}]\right) = 4.0\overline{3}$ determined in Sec. 4.5 with all pre-selection cuts (Sec. 4.3) applied.

In the three off-zones **1**, **2** and **3** events are observed. Whereas an averaged background of 2 events is thus expected, **6** signal candidates are measured in the on-zone. The distribution of the on-zone events observed in this analysis is shown together with the 16 on-zone events of the 4–year analysis in Fig. 35.

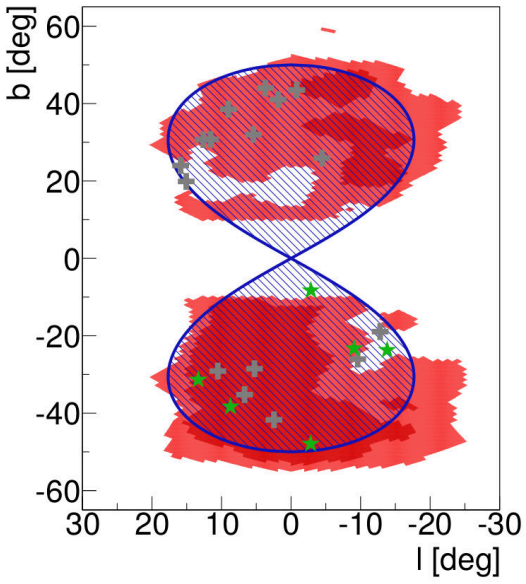

Figure 35: Galactic coordinates of the neutrino events observed in the on-zone. Grey crosses are the 16 events found in the 4–year analysis, green stars indicate the positions of the signal candidates found in the analysis update.

All six neutrino candidates found in the new analysis originate from the southern lobe,

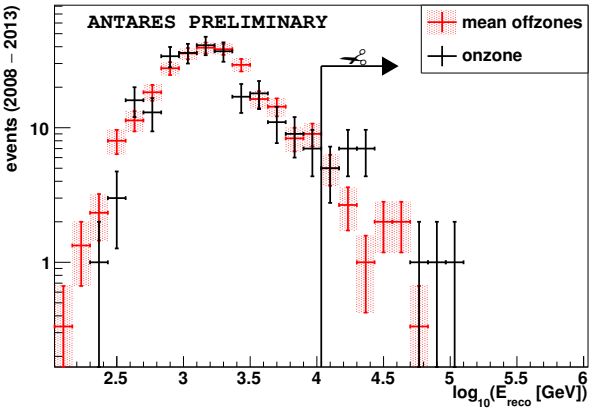

Figure 36: Comparison of the reconstructed energy for the on-zone and the average over the off-zones. Figure taken from Ref. [28].

which is not startling since the visibility in ANTARES is higher than for the northern lobe. In contrast, also a band of neutrinos reconstructed within the northern bubble was observed in the 4–year analysis. The observed events do not show a strong clustering in time, as can be seen from Tab. 4. Also, the additional on-zone events in the new analysis are all in the lower part of the reconstructed energy range above the cut, as shown in Fig. 36. Comparing the reconstruction result of the AaFit track reconstruction and the Dusj shower reconstruction on the ANTARES event display (see Appendix F), all six neutrino candidates found look clearly track-like.

Combining the two analyses, a total of 22 (16+6) on-zone events is found in six years (2008–2013) of ANTARES data. The background in the three off-zones in the same dataset sums to an average of 13 (11+2) events.

Since an excess is seen in the on-zone, it is a key question how significant this excess is. In frequentist statistics, a discovery can be claimed, if the probability is very small to make an observation from overfluctuating background only. This probability is usually defined as the area in a Gaussian tail in terms of σ. 3σ would be an 'evidence' for a signal, a discovery can be claimed if the probability exceeds 5σ.

It was first shown by Li and Ma in Ref. [53], that the statistical significance S of an excess in an on- and off-zone analysis can be estimated with the following calculation:

$$S = \sqrt{2}\left\{ N_{\mathrm{on}} \ln\left[\frac{1+\alpha}{\alpha}\left(\frac{N_{\mathrm{on}}}{N_{\mathrm{on}}+N_{\mathrm{off}}}\right)\right] + N_{\mathrm{off}} \ln\left[(1+\alpha)\left(\frac{N_{\mathrm{off}}}{N_{\mathrm{on}}+N_{\mathrm{off}}}\right)\right]\right\}^{1/2}, \quad (29)$$

where $1/\alpha = 3$ is the number of off-zones. N_{on} is the total number of events observed in the on-zone, N_{off} the total number of all three off-zones together. It was shown, that S corresponds to a single tail of a Gaussian distribution, and can therefore be used to express the significance in units of standard deviations for this type of measurement using on- and off-zones with low statistics [53].

The excess in the 16 on-zone events over the expected background of $33/3 = 11$ off-zone events Eq. 29 yields a significance of 1.2σ in the 4–year analysis alone [17]. For the

6 on-zone events and a total of 6 background events in the analysis update, the obtained significance is 1.86σ. For the whole analysed period from 2008 to 2013 with 22 on-zone events and 39 off-zone events, the excess is 1.92σ.

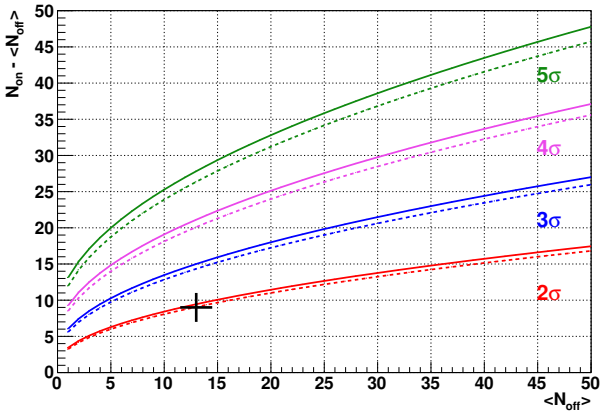

Figure 37: Signal significances calculated using Eq. 29 for an excess in the events measured in the onzone N_{on} over the average background $\langle N_{\mathrm{off}} \rangle$. The solid (dashed) lines represent two to five standard deviations when the background is measured in three (four) off-zones.

Fig. 37 shows that the significance of a measured excess does only increase marginally if the background was determined from four instead of three off-zones.

Under the assumption that the excess of nine events over the background expectation of 13 in the on-zone is due to a real signal, 2–3 times the current statistics is needed for an evidence of a FB flux at the 3σ-level with the current analysis. While there is no sufficient amount of data to achieve this with the current event selection in the track-channel alone, a combined analysis using tracks and showers and an optimised run-selection may achieve this. The expectation of the actual signal flux for the most optimistic, and considering the mentioned preliminary HAWC result too optimistic, case of an E^{-2} spectrum without cut-off is 4.3–8.7 events (cf. Tab. 3 and taking into account that the lower bound of the allowed flux from Eq. 9 was taken for the MRF optimisation). However, the measured excess is still compatible with background only. The observed background of 33 in the previous analysis would yield 15 events of background when scaling the lifetime. Only 6 are observed, which can be attributed to the increasing amount of broken OMs and, in particular, to the loss in data due to (presumably) aging or biofouling observed in the last years.

4.7 | Systematic uncertainties and flux upper limit

Since the excess seen in the on-zone is not statistically significant, upper limits are set on the signal flux. The 90% upper limits are again calculated using the approach by Feldman&Cousins [52]:

$$\Phi_{90\%} = \Phi_{\mathrm{model}} \times \frac{\mu_{90\%}\left(N_{\mathrm{on}} = 22, \langle N_{\mathrm{off}} \rangle = 13\right)}{s_1 + s_2}, \tag{30}$$

where s_1, s_2 are the number of signal events for the 4–year analysis and the new analysis from Tab. 3, and $\mu_{90\%}$ is the 90% Feldman&Cousins upper limit for the observed number

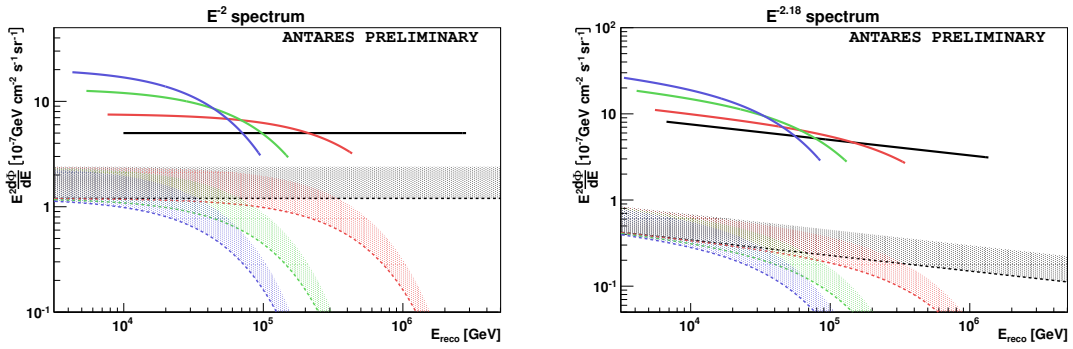

Figure 38: Upper limits on the neutrino flux from the Fermi Bubbles for different cutoff energies (black: no cut-off, red: 500 TeV, green: 100 TeV, blue: 50 TeV). The shaded areas are the corresponding flux predictions for hadronic models. The limits are drawn for the energy range where 90% of the signal is expected. Figures taken from Ref. [28].

of signal and background events. The obtained upper limits are given in Fig. 38. The model fluxes are indicated as shaded bands. The upper limits presented do not yet include systematic errors. A dedicated simulation with the absorption and scattering lengths varied by $\pm 10\%$ is still to be done at the moment of writing this thesis, and the upper limits will shift up slightly when including these. Also the potential loss of signal events due to the reduced quantum efficiency should be evaluated. Already without systematics it can be seen, that the upper limits are above the flux sensitivities determined in Tab. 2, which is due to the strong excess observed in the on-zone.

5 | Conclusion & Outlook

The latest analysis by Fermi-LAT [23] disfavours a hard E^{-2} neutrino spectrum from the Fermi Bubbles. Therefore a steeper spectrum has been derived from the Fermi data for the analysis of 2012 and 2013 data. In the run selection a new method to identify sparking runs in ANTARES was presented. It has been shown, that the analysis-cuts of the 4–year analysis can be re-used as the result of a dedicated cut optimisation. The analysis resulted in an excess of 6 events observed in the on-zone with an expected background of 2 events. The combined significance of the excess in six years of ANTARES data sums to 1.9σ, which is not statistically significant, but drives the upper limits above the flux sensitivity. Here, a detailed study of the systematics still needs to be included to the upper limits calculation.

In the future, the KM3NeT detector will improve the sensitivity by at least one order of magnitude [54]. Until then, also a more detailed study of the γ-ray spectrum by the HAWC observatory will set better constraints of the neutrino flux that can be expected from the Fermi Bubbles.

Since shower reconstructions with a small angular resolution compared to the size of the Fermi Bubbles are at hand in ANTARES, the next step will be a combined analysis using tracks and showers. Results from this study of combining tracks and showers are still due and therefore not part of this thesis, but the use of multivariate methods to select the track and shower signal is envisaged. The result from this will either further increase the intriguing excess seen in the on-zone or be able to set more stringent limits on the signal flux.

References

[1] M. Su, T. R. Slatyer, and D. P. Finkbeiner, *Giant Gamma-ray Bubbles from Fermi-LAT: Active Galactic Nucleus Activity or Bipolar Galactic Wind?*, ApJ **724** (Dec., 2010) 1044–1082, [arXiv:1005.5480].

[2] E. Carretti, R. M. Crocker, L. Staveley-Smith, M. Haverkorn, C. Purcell, B. M. Gaensler, G. Bernardi, M. J. Kesteven, and S. Poppi, *Giant magnetized outflows from the centre of the Milky Way*, Nature **493** (Jan., 2013) 66–69, [arXiv:1301.0512].

[3] G. Dobler, *A Last Look at the Microwave Haze/Bubbles with WMAP*, ApJ **750** (May, 2012) 17, [arXiv:1109.4418].

[4] S. L. Snowden, R. Egger, M. J. Freyberg, D. McCammon, P. P. Plucinsky, W. T. Sanders, J. H. M. M. Schmitt, J. Trümper, and W. Voges, *ROSAT Survey Diffuse X-Ray Background Maps. II.*, ApJ **485** (Aug., 1997) 125–135.

[5] Nasa's Goddart Space Flight Center, "Homepage." http://www.nasa.gov/mission_pages/GLAST/news/new-structure.html, Aug., 2015.

[6] G. Dobler, *Identifying the Radio Bubble Nature of the Microwave Haze*, ApJ **760** (Nov., 2012) L8, [arXiv:1208.2690].

[7] G. Dobler, I. Cholis, and N. Weiner, *The Fermi Gamma-Ray Haze from Dark Matter Annihilations and Anisotropic Diffusion*, ApJ **741** (Nov., 2011) 25, [arXiv:1102.5095].

[8] D. Hooper and T. R. Slatyer, *Two emission mechanisms in the Fermi Bubbles: A possible signal of annihilating dark matter*, *Physics of the Dark Universe* **2** (Sept., 2013) 118–138, [arXiv:1302.6589].

[9] F. Guo and W. G. Mathews, *The Fermi Bubbles. I. Possible Evidence for Recent AGN Jet Activity in the Galaxy*, ApJ **756** (Sept., 2012) 181, [arXiv:1103.0055].

[10] K.-S. Cheng, D. O. Chernyshov, V. A. Dogiel, C.-M. Ko, and W.-H. Ip, *Origin of the Fermi Bubble*, ApJ **731** (Apr., 2011) L17, [arXiv:1103.1002].

[11] R. M. Crocker and F. Aharonian, *Fermi Bubbles: Giant, Multibillion-Year-Old Reservoirs of Galactic Center Cosmic Rays*, *Physical Review Letters* **106** (Mar., 2011) 101102, [arXiv:1008.2658].

[12] C. van Eldik, *Gamma rays from the Galactic Centre region: A review*, *Astroparticle Physics* **71** (Dec., 2015) 45–70, [arXiv:1505.0605].

[13] B. C. Lacki, *The Fermi bubbles as starburst wind termination shocks*, MNRAS **444** (Oct., 2014) L39–L43, [arXiv:1304.6137].

[14] P. Mertsch and S. Sarkar, *Fermi Gamma-Ray "Bubbles" from Stochastic Acceleration of Electrons*, *Physical Review Letters* **107** (Aug., 2011) 091101, [arXiv:1104.3585].

[15] S. Thoudam, *Fermi Bubble γ-Rays as a Result of Diffusive Injection of Galactic Cosmic Rays*, ApJ **778** (Nov., 2013) L20, [arXiv:1304.6972].

[16] Selig, M. and Vacca, V. and Oppermann, N. and Enßlin, T., *Imaging the Fermi gamma-ray sky*, *Proceedings of the 34th ICRC* **PoS (ICRC2015) 768** (2015).

[17] **ANTARES** Collaboration, S. Adrián-Martínez et al., *A Search for Neutrino Emission from the Fermi Bubbles with the ANTARES Telescope*, *Eur. Phys. J.* **C74** (2014), no. 2 2701, [arXiv:1308.5260].

[18] V. Kulikovskiy, *Neutrino astrophysics with the ANTARES telescope*. PhD thesis, University of Genova, 2014.

[19] **ANTARES** Collaboration, S. Adrián-Martínez et al., *Search for Cosmic Neutrino Point Sources with Four Years of Data from the ANTARES Telescope*, ApJ **760** (Nov., 2012) 53, [arXiv:1207.3105].

[20] F. Folger, *Search for a diffuse cosmic neutrino flux using shower events in the ANTARES neutrino telescope*. PhD thesis, FAU Erlangen-Nürnberg / ECAP, 2014.

[21] Michael, T., *TANTRA – Tinos's ANTARES Shower Reconstruction Algorithm*, *ANTARES Internal Note* **ANTARES-SOFT-2015-002** (2015).

[22] **HAWC** Collaboration, H. Ayala et al., *A First Look at the Fermi Bubbles in HAWC Data*, *Proceedings of the 34th ICRC* (2015) ICRC2015–I/359.

[23] M. Ackermann et al., *The Spectrum and Morphology of the Fermi Bubbles*, ApJ **793** (Sept., 2014) 64, [arXiv:1407.7905].

[24] S. R. Kelner, F. A. Aharonian, and V. V. Bugayov, *Energy spectra of gamma rays, electrons, and neutrinos produced at proton-proton interactions in the very high energy regime*, Phys. Rev. D **74** (Aug., 2006) 034018, [astro-ph/0606058].

[25] C. Lunardini, S. Razzaque, and L. Yang, *Multimessenger study of the Fermi bubbles: Very high energy gamma rays and neutrinos*, Phys. Rev. D **92** (July, 2015) 021301, [arXiv:1504.0703].

[26] F. L. Villante and F. Vissani, *How precisely can neutrino emission from supernova remnants be constrained by gamma ray observations?*, Phys. Rev. D **78** (Nov., 2008) 103007, [arXiv:0807.4151].

[27] **Particle Data Group** Collaboration, K. A. Olive et al., *Review of Particle Physics*, *Chin. Phys.* **C38** (2014) 090001.

[28] S. Hallmann on behalf of the ANTARES Collaboration, *Search for a neutrino flux from the Fermi Bubbles with the ANTARES telescope*, *Proceedings of the 34th ICRC* **PoS (ICRC2015) 1059** (2015).

[29] M. Ageron, J. A. Aguilar, I. Al Samarai, A. Albert, F. Ameli, M. André, M. Anghinolfi, G. Anton, S. Anvar, M. Ardid, and et al., *ANTARES: The first undersea neutrino telescope*, *Nuclear Instruments and Methods in Physics Research A* **656** (Nov., 2011) 11–38, [arXiv:1104.1607].

[30] ANTARES, "Homepage." http://antares.in2p3.fr/Gallery/index.html, Aug., 2015.

[31] P. A. Cherenkov, *Visible emission of clean liquids by action of gamma radiation*, *Doklady Akademii Nauk SSSR* **2** (1934) 451+.

[32] T. Gal, "Git repository." https://github.com/tamasgal/rainbowalga, Aug., 2015.

[33] Escoffier, S., *Performance of the T3 Triggers on MC Data*, *ANTARES Internal Note* **ANTARES-SOFT-2008-009** (2008).

[34] De Jong, M., *The antares trigger software*, *ANTARES Internal Note* **ANTARES-SOFT-2005-005** (2005).

[35] B. Bardo, *Trigger studies for the Antares and KM3NeT neutrino telescopes*. Master's Thesis, University of Amsterdam, 2011.

[36] J. Schnabel and ANTARES Collaboration, *Muon energy reconstruction in the ANTARES detector*, *Nuclear Instruments and Methods in Physics Research A* **725** (Oct., 2013) 106–109.

[37] T. Michael on behalf of the ANTARES Collaboration, *Neutrino Point Source Search including Cascade Events with the ANTARES Neutrino Telescope*, *Proceedings of the 34th ICRC* **PoS (ICRC2015) 1078** (2015).

[38] ANTARES Collaboration: S. Escoffier, *The ANTARES detector: background sources and effects on detector performance*, *ArXiv e-prints* (Oct., 2007) [arXiv:0710.0527].

[39] G. Carminati, M. Bazzotti, S. Biagi, S. Cecchini, T. Chiarusi, A. Margiotta, M. Sioli, and M. Spurio, *MUPAGE: a fast atmospheric MUon GEnerator for neutrino telescopes based on PArametric formulas*, *ArXiv e-prints* (July, 2009) [arXiv:0907.5563].

[40] V. Agrawal, T. K. Gaisser, P. Lipari, and T. Stanev, *Atmospheric neutrino flux above 1 GeV*, Phys. Rev. D **53** (Feb., 1996) 1314–1323, [hep-ph/9509423].

[41] L. Core, *Search for an ultra high energy neutrino diffuse flux with the ANTARES telescope*. PhD thesis, University of Marseille, 2013.

[42] L. A. Fusco on behalf of the ANTARES Collaboration, *Search for an enhanced emission of neutrinos from the Southern Sky with the ANTARES telescope*, *Proceedings of the 34th ICRC* **PoS (ICRC2015) 1055** (2015).

[43] J. Schnabel on behalf of the ANTARES Collaboration, *Search for a diffuse cosmic neutrino flux with ANTARES using track and cascade events*, *Proceedings of the 34th ICRC* **PoS (ICRC2015) 1065** (2015).

[44] E. Presani, *Neutrino Induced Showers From Gamma-Ray Bursts*. PhD thesis, University of Amsterdam, 2011.

[45] J. A. Aguilar et al., *AMADEUS – The acoustic neutrino detection test system of the ANTARES deep-sea neutrino telescope*, *Nuclear Instruments and Methods in Physics Research A* **626** (Jan., 2011) 128–143, [arXiv:1009.4179].

[46] James, C. W., *Internal ANTARES telephone conference*, May, 2015.

[47] J. A. Aguilar et al., *A fast algorithm for muon track reconstruction and its application to the ANTARES neutrino telescope*, *Astroparticle Physics* **34** (Apr., 2011) 652–662, [arXiv:1105.4116].

[48] M. G. Aartsen, M. Ackermann, J. Adams, J. A. Aguilar, M. Ahlers, M. Ahrens, D. Altmann, T. Anderson, C. Arguelles, T. C. Arlen, and et al., *Observation of High-Energy Astrophysical Neutrinos in Three Years of IceCube Data*, *Physical Review Letters* **113** (Sept., 2014) 101101, [arXiv:1405.5303].

[49] S. Geißelsöder on behalf of the ANTARES Collaboration, *Model-independent search for neutrino anisotropies with the ANTARES neutrino telescope*, *Proceedings of the 34th ICRC* **PoS (ICRC2015) 1054** (2015).

[50] Sanguineti, M., *Internal ANTARES telephone conference*, May, 2015.

[51] G. C. Hill and K. Rawlins, *Unbiased cut selection for optimal upper limits in neutrino detectors: the model rejection potential technique*, ApJ **19** (2003) 393, [astro-ph/0209350].

[52] G. J. Feldman and R. D. Cousins, *Unified approach to the classical statistical analysis of small signals*, Phys. Rev. D **57** (Apr., 1998) 3873–3889, [physics/9711021].

[53] T.-P. Li and Y.-Q. Ma, *Analysis methods for results in gamma-ray astronomy*, ApJ **272** (Sept., 1983) 317–324.

[54] KM3NeT Collaboration, S. Adrián-Martínez, and et al., *Detection potential of the KM3NeT detector for high-energy neutrinos from the Fermi bubbles*, *Astroparticle Physics* **42** (Feb., 2013) 7–14, [arXiv:1208.1226].

[55] N. Karlsson, "Git repository." https://github.com/niklask/cparamlib/, Aug., 2015.

[56] T. Kamae, N. Karlsson, T. Mizuno, T. Abe, and T. Koi, *Parameterization of γ, $e^{+/-}$, and Neutrino Spectra Produced by p-p Interaction in Astronomical Environments*, ApJ **647** (Aug., 2006) 692–708, [astro-ph/0605581].

[57] N. Karlsson and T. Kamae, *Parameterization of the Angular Distribution of Gamma Rays Produced by p-p Interaction in Astronomical Environments*, ApJ **674** (Feb., 2008) 278–285, [arXiv:0709.0233].

Statutory Declaration

I declare that I have developed and written the enclosed thesis entirely by myself and have not used sources or means without declaration in the text. Any thoughts or quotations which were inferred from these sources are cleary marked as such. This thesis was not submitted in the same or in a substantially smiliar version, not even partially, to any other authority to achieve an academic grading. The results of this work have in part been published in the proceedings of the 34th International Cosmic Ray Conference [28] held in The Hague (The Netherlands).

Steffen Hallmann Erlangen, 06/09/2015

Acknowledgements

■ First of all I would like to thank Gisela Anton for giving me the opportunity to work on this very interesting topic. With your continuous support you have given me the opportunity to join summer schools and several Collaboration Meetings, which enriched my studies very much. Moreover, I am happy about the opportunity to help rearing the ORCA in your group during the upcoming years. ■ Many thanks also to Thomas Eberl for the supervision of my work on this thesis. You always had an open ear for my questions, and helped me whenever I hit on problems. Pushing me to start writing the thesis was especially valuable (and most probably also necessary). ;-) ■ I could benefit a lot from the track & shower combination meetings with Vladimir Kulikovskiy and Jutta Schnabel. Thank you for sharing the experience you had from the first Fermi Bubble analysis, Vladimir, and on the usage of multivariate classification tools, Jutta. ■ Last but not least I want to thank Thomas, Luigi, Jannik, Stefan, Jürgen and all the others I have not yet mentioned for spreading such a nice atmosphere both in our office and during lunch and coffee breaks at ECAP.

Appendix

A | Additional cross-checks regarding cut-offs and spectral indices of the gamma-ray spectrum

In the analysis, a spectral index of the proton flux of $\alpha_p = 2.25$ corresponding to a γ-flux spectral index of $\alpha = 2.18$ was assumed. This spectral index was reported in Ref. [25] as the best-fit value to the measured FB spectrum when the proton flux is parametrised as a power-law spectrum with exponential cut-off,

$$\frac{\mathrm{d}\Phi_p}{\mathrm{d}E} = \mathcal{N} \cdot \left(\frac{E_p}{1\,\mathrm{GeV}}\right)^{-\alpha} \cdot \exp\left[-\frac{E_p}{E_{\mathrm{cutoff,p}}}\right], \tag{31}$$

with a flux normalisation $\mathcal{N}$. There, the $\gamma-$ and neutrino-spectra used are a parametrisation derived from the SIBYLL code [24]. In the following, the best-fit choice of $\alpha_p = 2.25$ (based on a coarse scanning with step-width 0.25) is verified with a full parameter scan on the spectral index α_p and the proton cutoff $E_{\mathrm{cutoff,p}}$ using the `cparamlib` package [55] which is an implementation of the $\gamma-$ and neutrino-flux parametrisations by Kamae et al. [56] & Karlsson and Kamae [57]. Also the approximation of $E_{\mathrm{cutoff},\nu} \approx 1/20 \times E_{\mathrm{cutoff},p}$ is compared to the SIBYLL parametrisation, and comments on the shift from 2.25 to 2.18 between the proton and neutrino spectrum are given.

Parameter scan for best fit proton spectral indices and cutoffs

For the proton parametrisation in Eq. 31, with a known spectral index α_p and cutoff-energy $E_{\mathrm{cutoff,p}}$, the γ-ray spectrum can be obtained using the flux parametrisation in the `cparamlib` package [55]. The obtained spectrum has the parametrisation $\mathcal{N}$ as a free parameter. Fitting this spectrum to the Fermi Bubble spectrum observed by Fermi-LAT, will yield a p-value, which is 0, if the fit is very bad. The data points for the

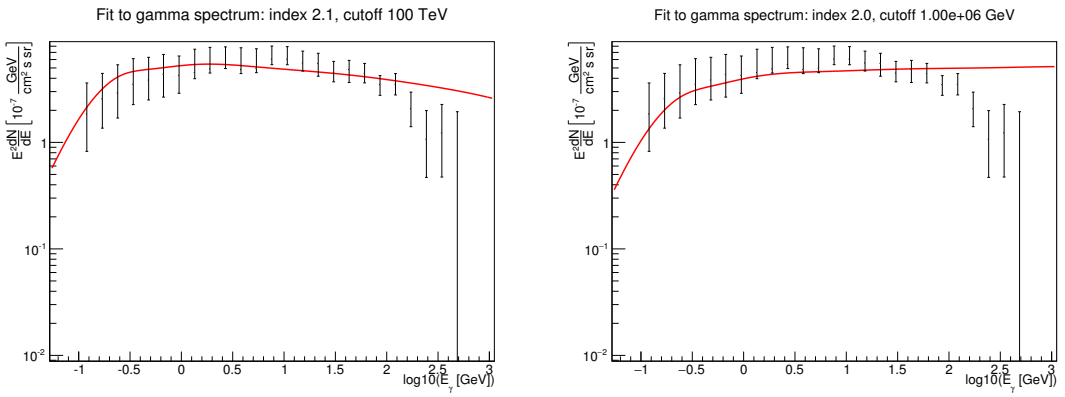

Figure 39: Fit of two γ-ray spectra (red line) obtained with the `cparamlib` package to the energy spectrum of the Fermi Bubbles [23, Tab. 2].

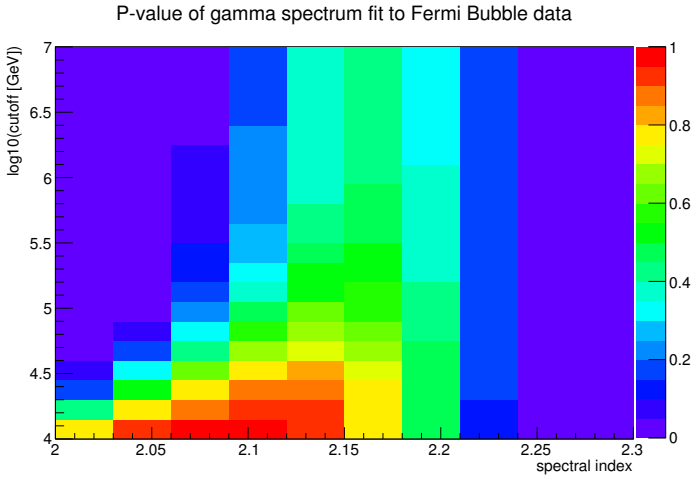

Figure 40: P-values of a fit of the parametrised γ-flux to the Fermi Bubble spectrum. The γ-flux is fit for different values of the proton flux 'spectral index' and 'cutoff'.

Fermi Bubble flux are taken from [23, Tab. 2]. Fig. 39 shows a fit of the γ-ray spectrum resulting from the proton flux for two exemplary cut-off energies and spectral indices.

A parameter scan is done in several steps in a range of $2.0 < \alpha_p < 2.3$ and $10\,\mathrm{TeV} < E_{\mathrm{cutoff},p} < 10\,\mathrm{PeV}$. The resulting p-value of the fits is presented in Fig. 40. It can be seen that for the desired PeV cut-off energies a spectral index in the range of 2.15–2.20 yields the best fit, which is not far from the value of 2.25 used in the analysis. Also, Ref. [25] uses a relatively coarse scanning ($\Delta\alpha_p = 0.25$) of α_p and uses the spectra separated into northern and southern bubble for the fit. Given this, both results are in good agreement. For steeper spectra ($\alpha_p \approx 2.0$), cut-off energies of below 100 TeV are needed to fit the Fermi-LAT data.

Some more details on the Sibyll parametrisation of the neutrino flux

In Fig. 41 (left), the neutrino flux parametrisation of Ref. [24], is fit with an $E^{-2.20}$ and an $E^{-2.18}$ power-law. This illustrates, why the index of 2.18 is used for the analysis instead of the more natural choice of using less decimal digits, i.e. 2.2. Also, looking at Fig. 41 (right), it can be seen that an $E^{-}2$ neutrino flux would be generated by a slightly softer proton spectrum with an index close to $\alpha_p = 2.05$.

Comparing the cutoff $E_{\mathrm{cutoff},\nu} \approx 1/20 \times E_{\mathrm{cutoff},p}$ assumed in Eq. 7 for $E_{\mathrm{cutoff},p} = 30\,\mathrm{PeV}$ with the parametrisation of the neutrino flux in Fig. 42, it can be seen that the cutoff in the parametrisation is at slightly higher energies. Hence, the factor 1/20 yields a conservative estimate for the neutrino cutoff.

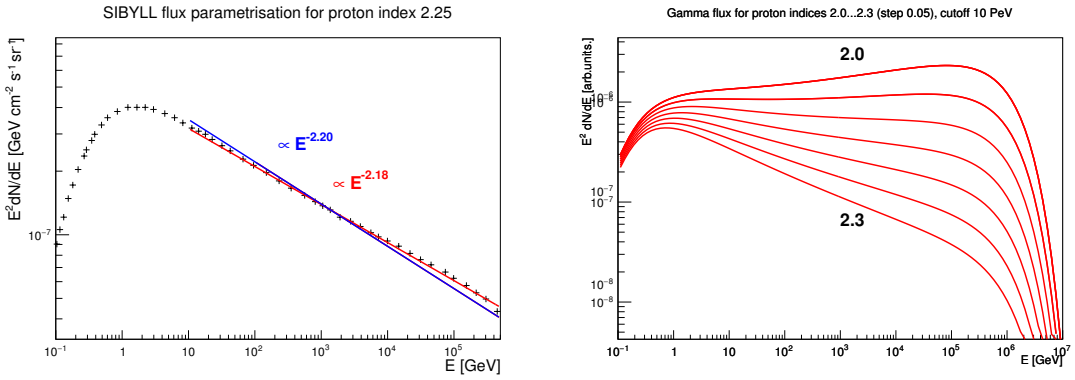

Figure 41: *Left:* Comparison of an $E^{-2.18}$ (red) and $E^{-2.20}$ (blue) fit to the neutrino flux parametrisation. *Right:* Parametrised γ-fluxes for different proton spectral indices.

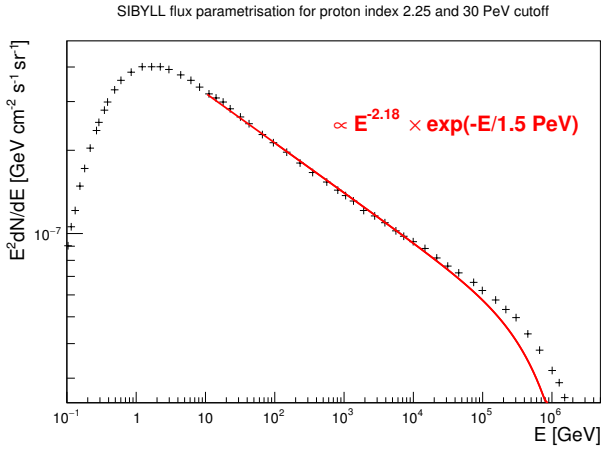

Figure 42: Comparison between a neutrino spectrum from the parametrisation (black crosses) and the assumed resulting neutrino flux which is used in the analysis (red line).

B | On- and off-zones at the IceCube detector

The IceCube detector is located directly at the south pole (i.e. at 90° S). Hence, in contrast to ANTARES (cf. Fig. 11), neutrinos coming from the Fermi Bubbles are observed as down-going events or close to the horizon. Also, the rotation of the lobes in detector coordinates during the day is in the opposite direction compared to ANTARES. As illustrated in Fig. 43 for down-going events, a total of three off-zones can be accomodated also at the IceCube detector.

Due to the special position at 90° S, a point within the Fermi Bubbles will always be observed at the same zenith angle in local coordinates. Hence, for every point in time the visibility of each zone will be the same (given azimuthal dependences can be neglected). This is an advantage with respect to ANTARES, where the visibilities are only equal when averaged over a sidereal day. On the other hand, a search for a signal from the Fermi Bubbles would need to concentrate on down-going and horizontal events, where the rejection of atmospheric muons takes more effort.

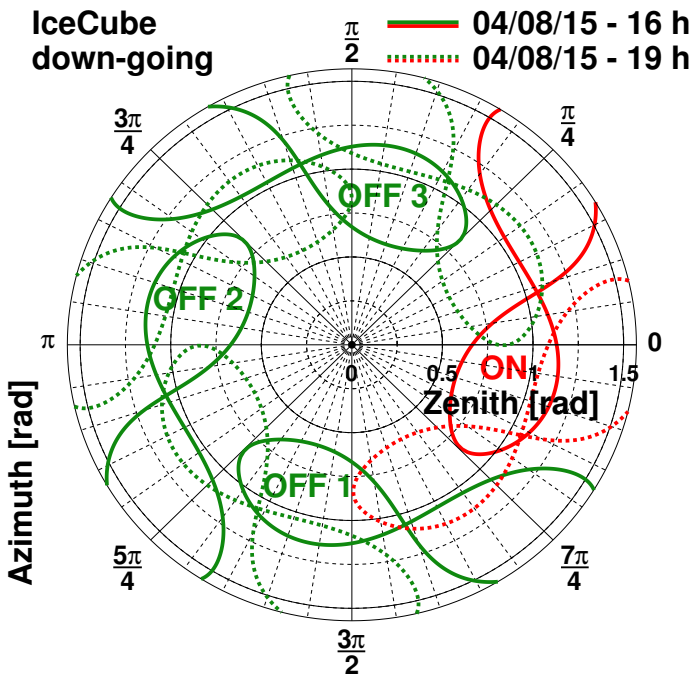

Figure 43: On-zone (red, solid) and the three off-zones (green, solid) as seen within the IceCube detector at a particular time. The range of zenith angles is restricted to down-going events. The dashed lines illustrate the local positions within the detector three hours later. The off-zones are shifted in time by 6 (off-zone 1), 12 (off-zone 2) and 18 hours (off-zone 3) with respect to the on-zone.

C | List of runs used for the track analysis

45546 45553 45557 45561 45563 45577 45586 45592 45595 45598 45617 45620 45626 45628 45630
45635 45648 45653 45658 45663 45665 45670 45681 45687 45689 45692 45695 45700 45710 45713
45714 45717 45719 45721 45724 45728 45753 45755 45757 45761 45766 45771 45773 45775 45776
45778 45788 45800 45802 45804 45812 45814 45818 45820 45822 45825 45835 45843 45845 45848
45851 45853 45860 45862 45871 45873 45875 45909 45912 45915 45918 45920 45924 45931 45936
45938 45940 45942 45944 45946 45956 45962 45971 45978 45983 45985 45987 45991 45994 45996
45998 46003 46006 46009 46011 46014 46026 46030 46033 46036 46040 46043 46045 46052 46054
46092 46094 46097 46101 46104 46106 46109 46112 46120 46122 46124 46129 46130 46133 46135
46139 46140 46141 46143 46147 46153 46165 46167 46169 46170 46173 46177 46183 46193 46197
46207 46211 46217 46225 46228 46230 46241 46310 46324 46341 46353 46362 46369 46383 46388
46398 46401 46404 46406 46407 46420 46422 46423 46428 46430 46438 46442 46449 46451 46457
46460 46469 46475 46478 46482 46487 46489 46492 46494 46498 46502 46507 46510 46514 46518
46521 46523 46525 46527 46531 46533 46536 46538 46540 46542 46551 46556 46558 46559 46561
46563 46564 46572
61908 61915 61917 61920 61922 61924 61928 61931 61935 61941 61943 61949 61954 61958 61960
61966 61969 61971 61973 61975 61976 61978 61980 61986 61988 61989 61993 61996 61999 62001
62002 62004 62006 62011 62013 62015 62017 62019 62021 62022 62024 62028 62030 62032 62033
62039 62043 62044 62046 62048 62050 62054 62056 62057 62059 62061 62074 62076 62078 62080
62085 62087 62093 62095 62104 62106 62108 62110 62112 62113 62115 62117 62119 62121 62127
62128 62130 62132 62134 62135 62137 62140 62143 62145 62150 62155 62157 62159 62165 62168
62172 62174 62178 62180 62182 62189 62191 62228 62232 62234 62236 62238 62241 62243 62247
62249 62250 62252 62254 62258 62261 62263 62269 62270 62276 62279 62281 62283 62285 62286
62288 62290 62291 62295 62297 62298 62303 62305 62309 62314 62315 62317 62319 62324 62328
62329 62331 62336 62340 62344 62345 62347 62349 62352 62354 62355 62369 62370 62376 62378
62380 62384 62386 62390 62392 62394 62396 62398 62400 62406 62408 62410 62414 62416 62418
62422 62424 62429 62432 62436 62444 62446 62448 62450 62452 62456 62460 62462 62464 62466
62468 62475 62477 62484 62488 62489 62491 62498 62500 62509 62511 62513 62515 62525 62527
62529 62533 62535 62537 62539 62541 62543 62545 62551 62553 62554 62556 62559 62560 62562
62565 62566 62570 62572 62577 62579 62583 62589 62599 62601 62602 62612 62614 62616 62625
62634 62636 62638 62645 62651 62655 62657 62661 62668 62675 62679 62681 62683 62687 62697
62701 62705 62714 62716 62718 62720 62726 62730 62745 62749 62753 62755 62757 62759 62766
62773 62780 62782 62784 62791 62796 62800 62804 62807 62811 62812 62815 62819 62821 62824
62826 62827 62834 62839 62843 62844 62846 62859 62862 62865 62867 62877 62879 62885 62887
62891 62897 62899 62901 62902 62906 62911 62913 62915 62917 62919 62921 62922 62930 62935
62937 62939 62941 62945 62947 62949 62951 62957 62959 62962 62964 62966 62968 62969 62971
62973 62977 62985 62987 62989 62993 62995 62997 62999 63003 63007 63009 63011 63019 63021
63026 63030 63032 63033 63035 63041 63043 63045 63049 63068 63072 63074 63076 63078 63080
63085 63089 63091 63093 63095 63097 63099 63101 63107 63109 63115 63150 63204 63206 63210
63218 63222 63224 63228 63230 63241 63247 63249 63261 63263 63265 63267 63269 63271 63273
63275 63277 63281 63285 63287 63291 63326 63328 63330 63336 63340 63342 63343 63344 63345
63348 63352 63353 63355 63361 63365 63369 63371 63373 63375 63377 63380 63382 63384 63387
63388 63390 63398 63400 63402 63404 63411 63413 63417 63419 63519 63521 63525 63527 63529
63531 63539 63541 63542 63543 63544 63545 63547 63548 63550 63552 63735 63736 63738 63740
63742 63766 63768 63770 63772 64074 64077 64083 64087 64088 64090 64092 64094 64113 64114
64116 64117 64121 64126 64128 64130 64135 64136 64138 64140 64144 64146 64148 64150 64153
64155 64159 64192 64196 64267 64334 64403 64404 64406 64408 64413 64419 64428 64430 64436
64440 64442 64444 64448 64450 64455 64489 64493 64495 64497 64500 64502 64503 64548 64600

64602 64606 64611 64615 64616 64618 64626 64630 64636 64637 64638 64640 64661 64662 64665
64668 64669 64671 64676 64688 64690 64692 64694 64725 64735 64737 64738 64741 64743 64744
64746 64748 64750 64751 64753 64755 64758 64772 64773 64776 64782 64791 64793 64795 64797
64805 64807 64884 64890 64903 64905 64908 64915 64918 64923 64926 64927 64929 64930 64933
64947 64960 64961 64963 64969 64972 64981 64983 64984 64989 64990 64992 64993 64994 64996
64997 64999 65000 65008 65011 65013 65018 65019 65021 65022 65025 65027 65028 65030 65031
65033 65034 65052 65057 65063 65066 65068 65071 65073 65074 65076 65088 65119 65120 65122
65123 65125 65136 65138 65146 65149 65150 65152 65160 65176 65177 65181 65183 65185 65187
65188 65189 65191 65196 65198 65199 65203 65214 65215 65220 65224 65226 65233 65239 65241
65244 65246 65247 65249 65252 65254 65258 65259 65261 65263 65265 65266 65271 65273 65274
65276 65278 65280 65288 65289 65291 65292 65296 65298 65310 65311 65317 65319 65323 65325
65329 65332 65333 65336 65339 65345 65346 65347 65349 65351 65352 65353 65355 65358 65360
65365 65366 65368 65369 65372 65374 65388 65390 65393 65398 65400 65410 65412 65414 65415
65417 65421 65423 65425 65428 65436 65438 65440 65441 65445 65447 65449 65453 65465 65469
65474 65475 65480 65482 65489 65493 65494 65495 65497 65499 65500 65505 65506 65509 65521
65525 65527 65528 65530 65531 65535 65537 65539 65542 65545 65547 65550 65551 65552 65556
65558 65559 65563 65565 65566 65575 65581 65583 65587 65588 65595 65597 65598 65600 65603
65605 65607 65609 65610 65612 65613 65617 65619 65620 65625 65627 65630 65632 65633 65637
65638 65640 65642 65647 65649 65652 65658 65661 65667 65669 65671 65676 65678 65684 65690
65691 65693 65694 65698 65699 65702 65704 65708 65716 65718 65719 65722 65724 65727 65732
65737 65740 65742 65743 65747 65751 65752 65755 65757 65760 65762 65764 65767 65770 65773
65779 65782 65784 65786 65787 65789 65790 65793 65795 65796 65799 65802 65803 65805 65806
65811 65814 65816 65817 65819 65821 65854 65858 65862 65864 65865 65867 65869 65870 65874
65875 65877 65879 65882 65884 65887 65890 65892 65894 65898 65900 65901 65903 65905 65907
65908 65911 65913 65915 65919 65921 65924 65926 65928 65930 65932 65935 65939 65940 65942
65949 65951 65955 65956 65958 65961 65965 65971 65973 65984 65987 65989 65990 65992 65993
65997 65999 66002 66004 66006 66007 66009 66013 66018 66024 66033 66058 66060 66062 66067
66069 66071 66079 66092 66095 66097 66100 66103 66105 66114 66115 66117 66119 66120 66125
66129 66131 66132 66134 66135 66137 66139 66140 66142 66146 66154 66155 66159 66161 66163
66164 66166 66168 66170 66171 66173 66177 66183 66187 66189 66191 66193 66195 66199 66204
66209 66213 66216 66219 66224 66232 66233 66237 66246 66257 66258 66260 66262 66264 66267
66271 66277 66286 66287 66299 66306 66312 66314 66316 66320 66322 66324 66326 66328 66330
66338 66340 66341 66347 66349 66351 66353 66362 66364 66365 66367 66369 66378 66380 66386
66388 66390 66392 66404 66406 66407 66421 66423 66428 66434 66435 66437 66439 66441 66445
66446 66448 66450 66452 66464 66466 66468 66470 66472 66474 66476 66491 66495 66497 66499
66502 66506 66510 66512 66515 66522 66526 66530 66532 66536 66538 66541 66543 66546 66548
66554 66555 66562 66565 66568 66569 66571 66573 66575 66577 66578 66581 66583 66585 66589
66590 66592 66594 66598 66599 66602 66608 66614 66616 66619 66621 66622 66624 66626 66628
66634 66636 66638 66640 66643 66649 66658 66664 66665 66667 66671 66673 66675 66677 66680
66682 66684 66686 66687 66689 66694 66703 66705 66709 66711 66713 66714 66718 66722 66724
66730 66733 66737 66743 66745 66749 66751 66752 66756 66762 66768 66772 66779 66781 66783
66786 66788 66792 66793 66800 66804 66805 66807 66809 66811 66818 66821 66823 66825 66827
66831 66832 66834 66838 66839 66841 66843 66844 66846 66847 66853 66859 66861 66862 66870
66871 66873 66877 66884 66888 66892 66894 66896 66898 66901 66909 66911 66913 66919 66923
66938 66939 66941 66947 66950 66955 66957 66963 66965 66969 66975 66978 66980 66983 66985
66987 66991 66993 66998 67000 67002 67004 67006 67008 67010 67012 67013 67015 67017 67021
67023 67025 67027 67029 67035 67037 67039 67047 67049 67053 67055 67057 67059 67062 67065
67067 67069 67071 67073 67075 67079 67081 67084 67091 67098 67100 67102 67104 67115 67117
67119 67122 67124 67126 67132 67136 67143 67145 67148 67150 67156 67187 67190 67192 67194

67196 67198 67202 67206 67217 67219 67224 67226 67228 67229 67231 67234 67236 67237 67239
67242 67244 67248 67250 67253 67255 67257 67263 67266 67270 67274 67277 67279 67280 67282
67288 67289 67291 67297 67300 67301 67307 67310 67312 67315 67323 67327 67335 67338 67339
67341 67343 67348 67350 67353 67355 67359 67360 67362 67367 67371 67372 67375 67377 67379
67380 67385 67387 67389 67391 67392 67394 67406 67409 67420 67423 67428 67431 67433 67434
67438 67440 67446 67452 67461 67463 67473 67475 67477 67478 67482 67490 67492 67497 67501
67502 67509 67510 67512 67516 67520 67529 67531 67533 67535 67542 67544 67547 67551 67554
67561 67566 67568 67571 67573 67576 67578 67580 67582 67583 67585 67586 67588 67590 67594
67597 67611 67615 67619 67622 67627 67628 67630 67632 67634 67638 67639 67653 67657 67661
67663 67665 67669 67671 67677 67679 67681 67687 67689 67692 67694 67701 67703 67705 67721
67723 67725 67735 67737 67741 67743 67747 67749 67750 67752 67756 67757 67759 67761 67765
67767 67768 67770 67774 67779 67783 67785 67787 67790 67792 67793 67795 67797 67799 67804
67805 67809 67811 67814 67817 67821 67824 67826 67828 67830 67833 67835 67844 67846 67848
67850 67852 67854 67858 67863 67871 67873 67877 67879 67881 67883 67889 67897 67899 67901
67903 68140 68143 68145 68147 68149 68154 68156 68158 68160 68162 68166 68170 68172 68530
68532 68534 68536 68538 68540 68544 68546 68549 68552 68554 68556 68558 68560 68562 68564
68566 68568 68570 68573 68575 68577 68579 68581 68583 68585 68587 68590 68592 68595 68597
68599 68601 68603 68605 68608 68610 68640 68642 68644 68646 68649 68651 68653 68655 68657
68659 68661 68663 68668 68670 68672 68676 68678 68683 68685 68687
68692 68694 68696 68697 68699 68701 68706 68708 68710 68712 68714 68716 68723 68726 68728
68730 68732 68736 68743 68745 68747 68749 68751 68753 68756 68759 68761 68764 68766 68768
68770 68772 68774 68776 68779 68781 68783 68786 68788 68794 68796 68798 68800 68802 68806
68807 68809 68811 68813 68815 68817 68819 68821 68822 68824 68826 68828 68832 68834 68835
68837 68841 68843 68845 68848 68850 68852 68854 68856 68858 68860 68862 68864 68865 68867
68869 68871 68873 68875 68879 68881 68885 68887 68889 68891 68893 68895 68897 68899 68901
68907 68909 68915 68917 68919 68923 68925 68927 68929 68933 68935 68936 68938 68939 68941
68943 68945 68947 68951 68955 68957 68959 68961 68965 68967 68969 68971 68975 68976 68978
68980 69000 69002 69004 69006 69008 69011 69013 69016 69018 69020 69022 69024 69026 69031
69033 69035 69037 69038 69040 69041 69045 69049 69050 69052 69054 69057 69059 69063 69065
69067 69070 69072 69074 69076 69078 69080 69082 69084 69086 69090 69092 69093 69095 69097
69099 69101 69103 69105 69107 69109 69111 69112 69114 69116 69118 69120 69121 69124 69127
69129 69131 69133 69135 69137 69139 69141 69144 69146 69152 69156 69157 69159 69161 69163
69165 69167 69169 69171 69175 69177 69179 69180 69182 69185 69187 69189 69191 69193 69197
69199 69201 69203 69205 69207 69211 69215 69217 69219 69221 69223 69225 69227 69230 69232
69234 69236 69238 69240 69242 69244 69246 69250 69252 69254 69256 69258 69262 69264 69267
69269 69271 69273 69274 69276 69278 69280 69282 69283 69286 69288 69290 69293 69295 69297
69299 69310 69312 69314 69316 69318 69320 69321 69323 69324 69326 69328 69332 69334 69336
69338 69340 69342 69344 69347 69352 69354 69356 69358 69360 69364 69366 69368 69370 69374
69375 69377 69379 69381 69383 69385 69387 69390 69421 69423 69425 69427 69432 69434 69436
69437 69440 69442 69444 69445 69447 69449 69451 69453 69455 69457 69461 69466 69468 69470
69472 69480 69483 69485 69487 69489 69493 69495 69497 69499 69501 69503 69505 69506 69508
69510 69512 69514 69516 69517 69519 69521 69527 69529 69531 69532 69534 69536 69538 69540
69542 69544 69549 69550 69552 69554 69556 69558 69561 69563 69564 69566 69567 69569 69571
69573 69575 69579 69581 69583 69584 69586 69588 69590 69592 69594 69596 69598 69603 69605
69607 69609 69611 69612 69616 69631 69633 69635 69637 69671 69673 69678 69683 69685 69687

69689 69695 69696 69698 69700 69739 70204 70210 70214 70217 70453 70458 70498 70503 70534
70540 70584 70601 70619 70623 70629 70634 70642 70647 70652 70659 70664 70679 70686 70694
70698 70703 70708 70719 70720 70723 70734 70741 70766 70773 70775 70778 70782 70790 70794
70848 70870 70875 70885 70919 70924 70932 70944 70950 70953 70986 70990 71005 71008 71011
71016 71018 71022 71026 71029 71034 71039 71043 71047 71052 71057 71062 71065 71067 71069
71070 71075 71079 71083 71090 71092 71096 71116 71121 71128 71136 71144 71266 71272 71275
71285 71291 71298 71304 71309 71325 71332 71335 71338 71340 71341 71343 71370 71375 71387
71394 71403 71407 71421 71435 71441 71442 71444 71450 71452 71459 71462 71466 71473 71477
71484 71486 71491 71504 71510 71512 71513 71520 71547 71555 71627 71647 71654 71666 71679
71683 71696 71710 71717 71754 71760 71763 71777 71780 71786 71803 71810 71821 71823 71831
71836 71838 71845 71856 71864 71878 71889 71901 71908 71914 71924 71939 71953 71974 71985
71989 71997 72001 72004 72035 72042 72058 72065 72084 72097 72100 72116 72123 72127 72131
72135 72139 72144 72150 72157 72162 72165 72169 72177 72179 72185 72192 72194 72201 72207
72222 72227 72237 72244 72250 72257 72263 72269 72274 72279 72286 72299 72305 72311 72317
72322 72329 72335 72348 72354 72374 72384 72391 72454 72460 72467 72475 72488 72494 72508
72528 72534 72541 72548 72552 72561 72572 72579 72587 72595 72601 72608 72611 72616 72624
72629 72634 72638 72644 72653 72657 72662 72668 72672 72677 72686 72696 72701 72710 72714
72719 72723 72727 72740 72743 72751 72760 72764 72774 72787 72794 72799 72805 72810 72814
72827 72835 72842 72848 72853 72861 72867 72872 72877 72891 72903 72908 72913 72918 72924
72931 72939 72943 72953 72959 72963 72979 72985 72993 73009 73023 73029 73040 73043 73048
73056 73058 73064 73068 73070 73082 73097 73104 73123 73130 73150 73163 73167 73177 73182
73184 73189 73192 73195 73200 73202 73208 73212 73217 73226 73257 73259 73269 73272 73277
73281 73288 73296 73299 73306 73315 73326 73357 73363 73373 73387 73400 73420 73427 73438
73443 73448 73453 73458 73463 73476 73480 73488 73493 73499 73504 73509 73516 73529 73535
73546 73566 73571 73578 73590 73596 73606 73611 73617 73628 73633 73639 73644 73652 73660
73665 73669 73679 73681 73684 73691 73697 73708 73714 73733 73743 73749 73752 73758 73789
73801 73807 73815 73820 73825 73828 73835 73839 73844 73853 73857 73860 73864 73866 73872
73875 73880 73905 73912 73916 73920 73926 73927 73933 73950 73958 73969 73974 73985 73990
73996 74000 74002 74012 74021 74028 74039 74041 74046 74052 74058 74065 74075 74079 74086
74091 74094 74095 74103 74110 74113 74129 74145 74147 74152 74158 74162 74168 74173 74179
74187 74194 74202 74208 74215 74226 74246 74257 74261 74268 74274 74279 74284 74293 74303
74307 74320 74326 74335

D | Details on the identified sparking runs

Runs listed in Sec. D.1 have been identified by collaborators. The method described in Sec. 4.2.3 is able to identify runs listed in Sec. D.2. Sec. D.3 contains runs where the brightest events are loosely clustered, some of them may also contain sparking events.

D.1 | Sparking runs identified by others

2007–2011:
30658 31309 33608 33610 34663 34665 35467 36600 36666 36670 36689 38347 38348 38349 38351 38352 38353 38355 38357 38482 39192 41668 41671 42507 42509 42511 42513 42746 42915 42919 43196 43202 43206 43210 43215 43684 43996 44030 44035 44070 45242 46980 51036 53508 53851 54512
2012–2013:
52675 54512 **55259 56457 63718** 64452 64457 **65532** 66037 66039 66042 66046 66049 66053 68950 **70201 70203 70633**

Bold face run numbers are suspect to be sparking but have not yet been confirmed.

D.2 | Sparking runs found in this analysis (i.e. $\overline{r} < \text{MEAN} - 5 \times \text{RMS}$)

33608 33610 36666 36670 36689 42513 42746 **42771** 43996 44030 52675 **52676** 54512 **64028 64619 65512 65518 65568 66020 66022 66035** 66037 66039 **66041** 66042 **66044** 66046 **66048** 66049 **66051** 66053 **66055 66235 66239 66241 66242 66248 66250 66255 66280 66282 66289 66291 66293 66295 66297 66300 68245** 70201 70203 70633

Bold face run numbers have not been identified as sparking before (i.e. are not listed in Sec. D.1).

D.3 | Low average pairwise distance runs found in this analysis (i.e. $\text{MEAN} - 5 \times \text{RMS} < \overline{r} < \text{MEAN} - 3 \times \text{RMS}$):

60847 64678 65506 65508 65572 66027 66033 66058 66060 66077 66237 66257 66287

D.4 | Event distributions for clustered sparking runs

For each of the runs identified as sparking by the low average distance of Dusj vertices (Sec. D.2), the distributions of the number of hits used by the Dusj and AAFit reconstruction algorithms are shown (plot 1, plot 2). Also the Dusj vertex distribution for all events with more than 100 (plot 3) and more than 50 (plot 4) used hits is shown. If the run has low statistics, the distribution for more than 15 used hits is shown instead of the one for more than 100.

SPARKING RUN 33608: $\overline{r} = 2.0\,\mathrm{m}$, AAFit rate ($\geq 200$ used hits): $34.56\,\mathrm{mHz}$

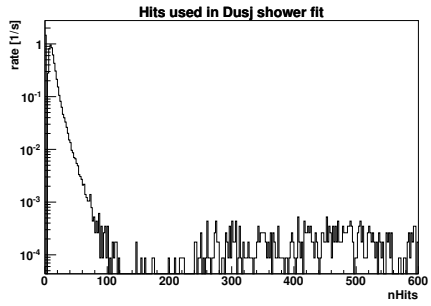

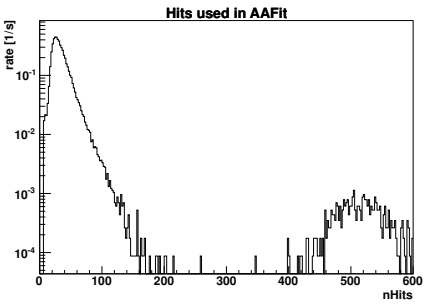

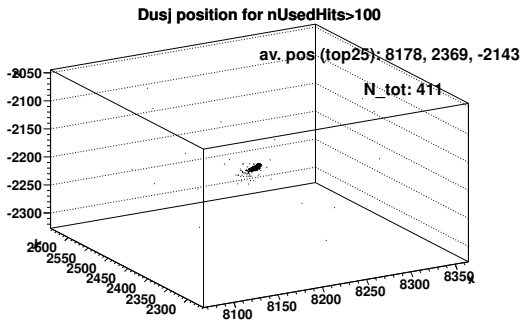

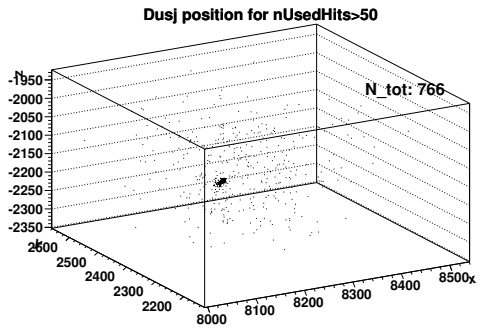

SPARKING RUN 33610: $\overline{r} = 5.0\,\mathrm{m}$, AAFit rate ($\geq 200$ used hits): $5.17\,\mathrm{mHz}$

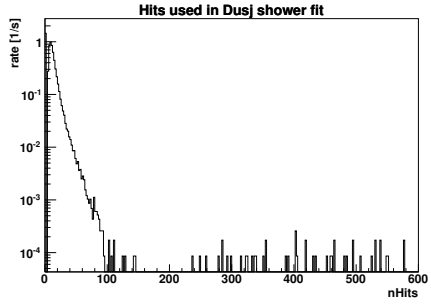

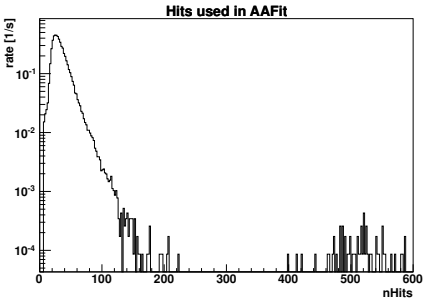

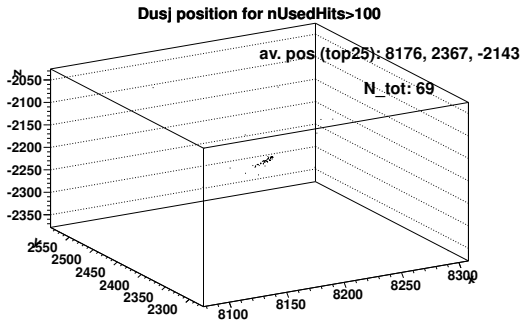

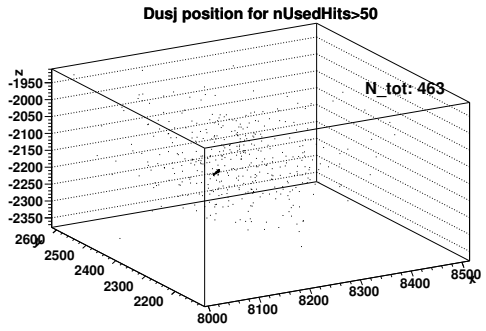

SPARKING RUN 36666: $\overline{r} = 3.6\,\mathrm{m}$, AAFit rate ($\geq 200$ used hits): $46.91\,\mathrm{mHz}$

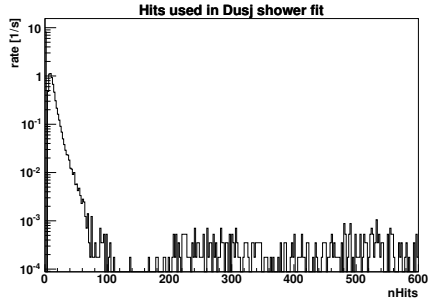

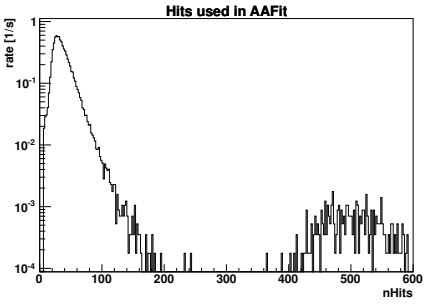

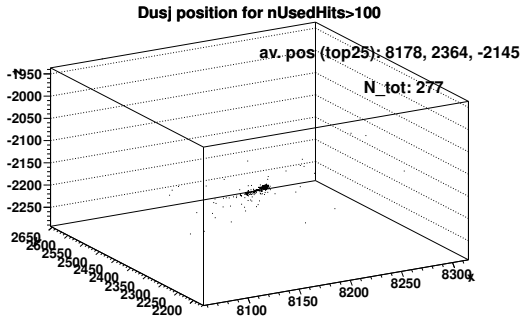

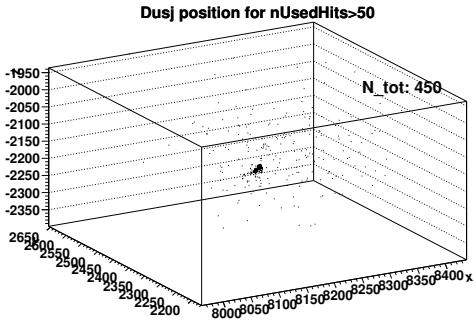

SPARKING RUN 36670: $\overline{r} = 13.1\,\mathrm{m}$, AAFit rate ($\geq 200$ used hits): $41.77\,\mathrm{mHz}$

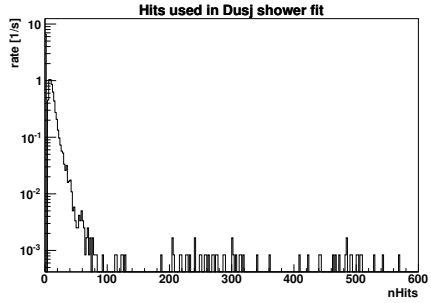

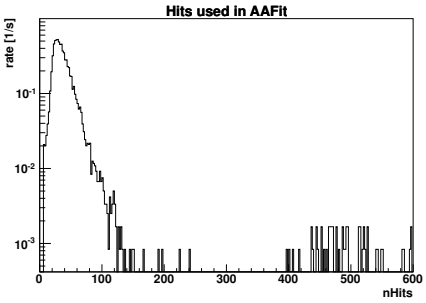

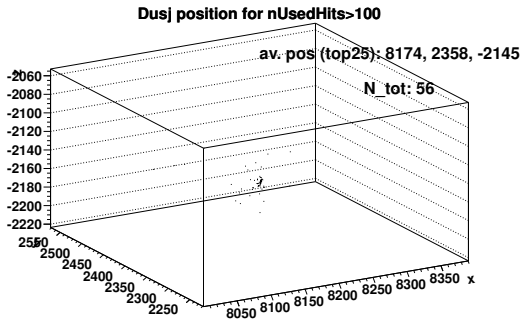

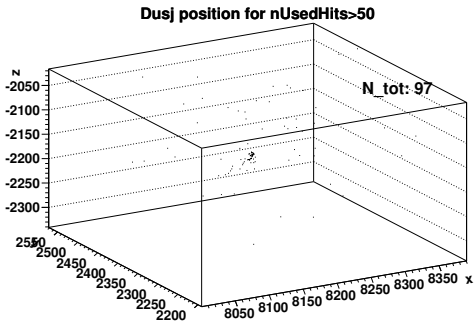

SPARKING RUN 36689: $\overline{r} = 1.8\,\mathrm{m}$, AAFit rate ($\geq 200$ used hits): $58.06\,\mathrm{mHz}$

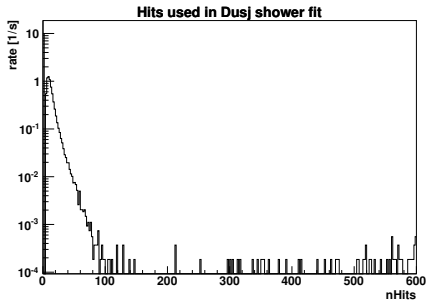

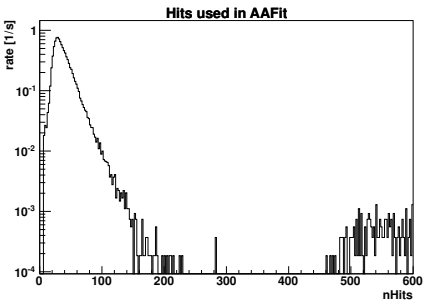

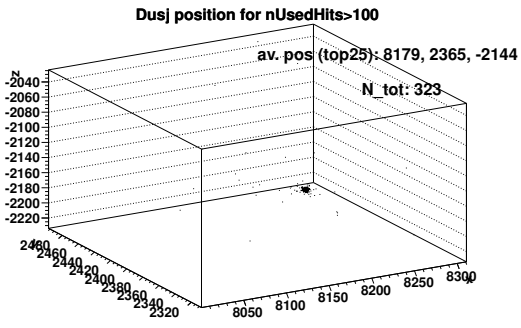

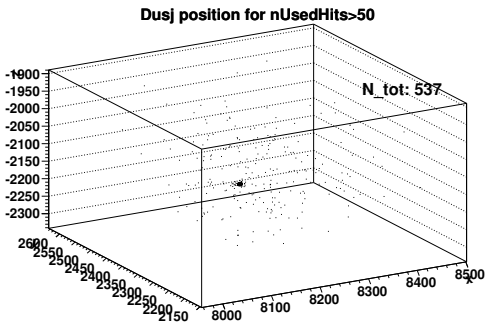

SPARKING RUN 42513: $\overline{r} = 66.2\,\mathrm{m}$, AAFit rate ($\geq 200$ used hits): $0.0\,\mathrm{mHz}$

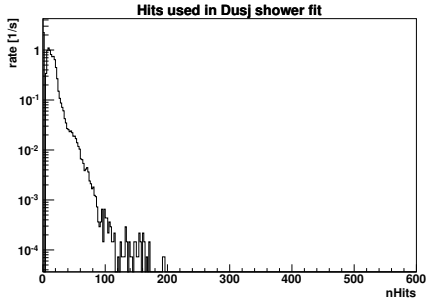

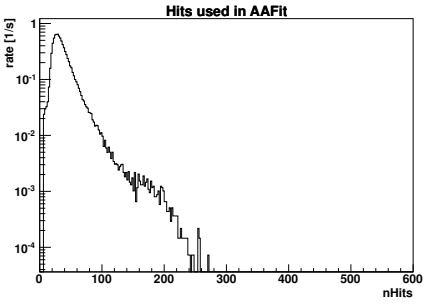

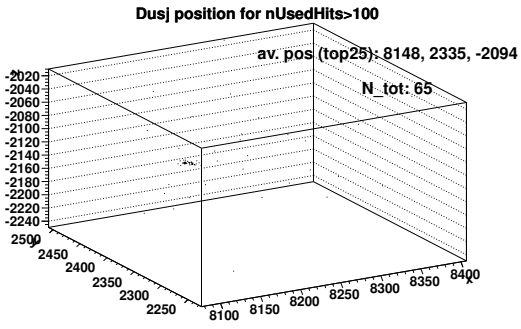

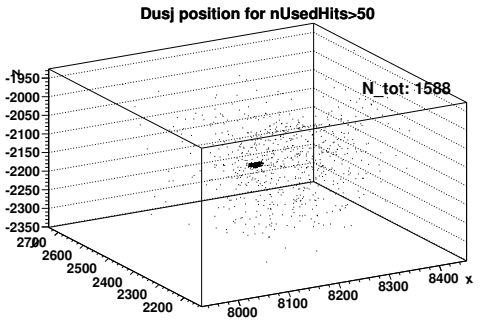

SPARKING RUN 42746: $\overline{r} = 56.2\,\mathrm{m}$, AAFit rate ($\geq 200$ used hits): $0.17\,\mathrm{mHz}$

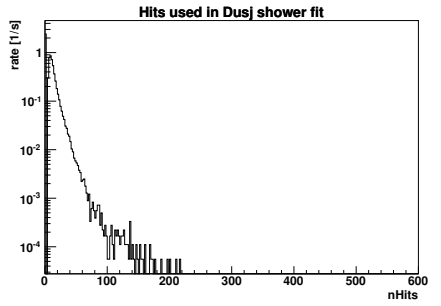

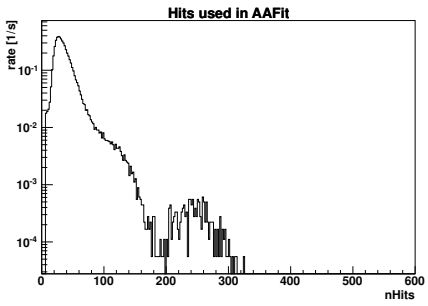

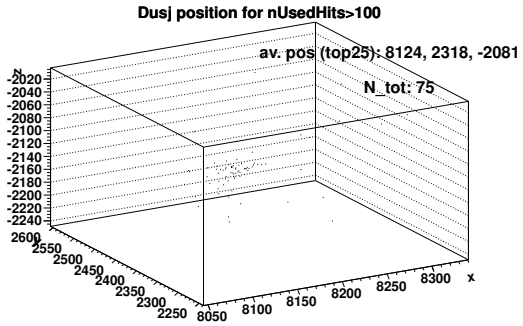

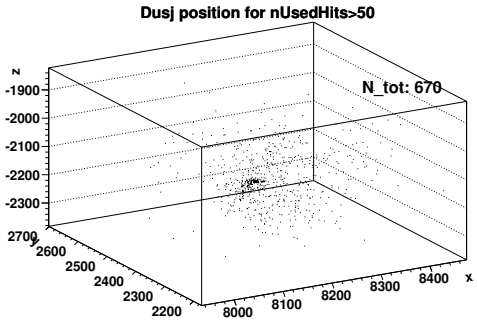

SPARKING RUN 42771: $\overline{r} = 87.3\,\mathrm{m}$, AAFit rate ($\geq 200$ used hits): $0.4\,\mathrm{mHz}$

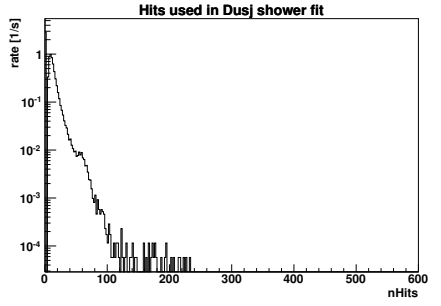

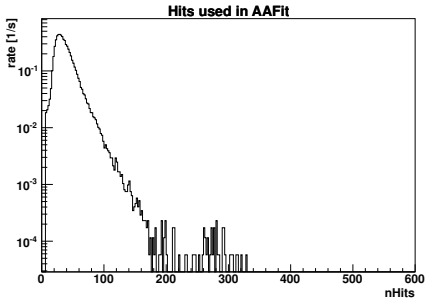

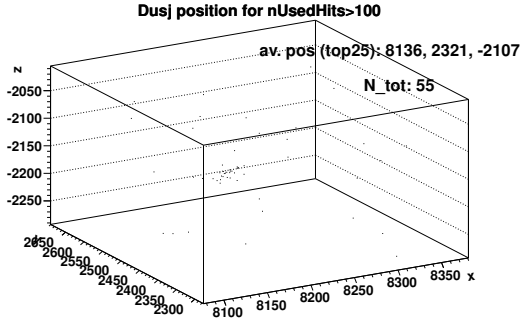

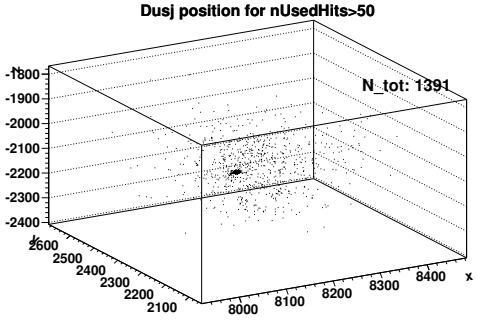

SPARKING RUN 43996: $\overline{r} = 83.0\,\mathrm{m}$, AAFit rate ($\geq 200$ used hits): $0.67\,\mathrm{mHz}$

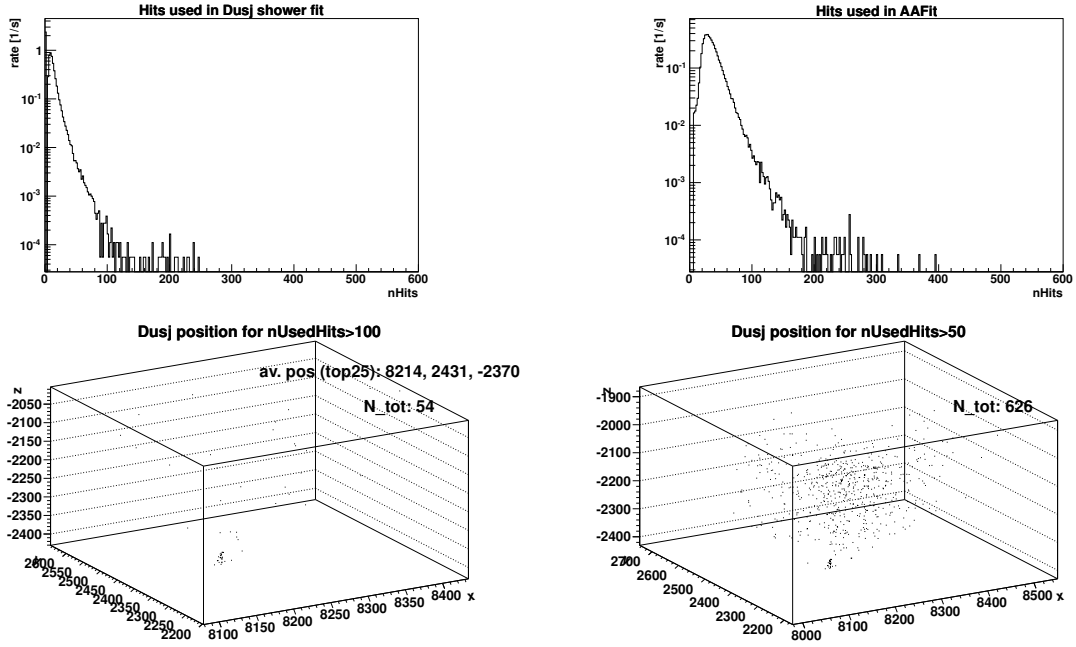

SPARKING RUN 44030: $\overline{r} = 79.2\,\mathrm{m}$, AAFit rate ($\geq 200$ used hits): $0.07\,\mathrm{mHz}$

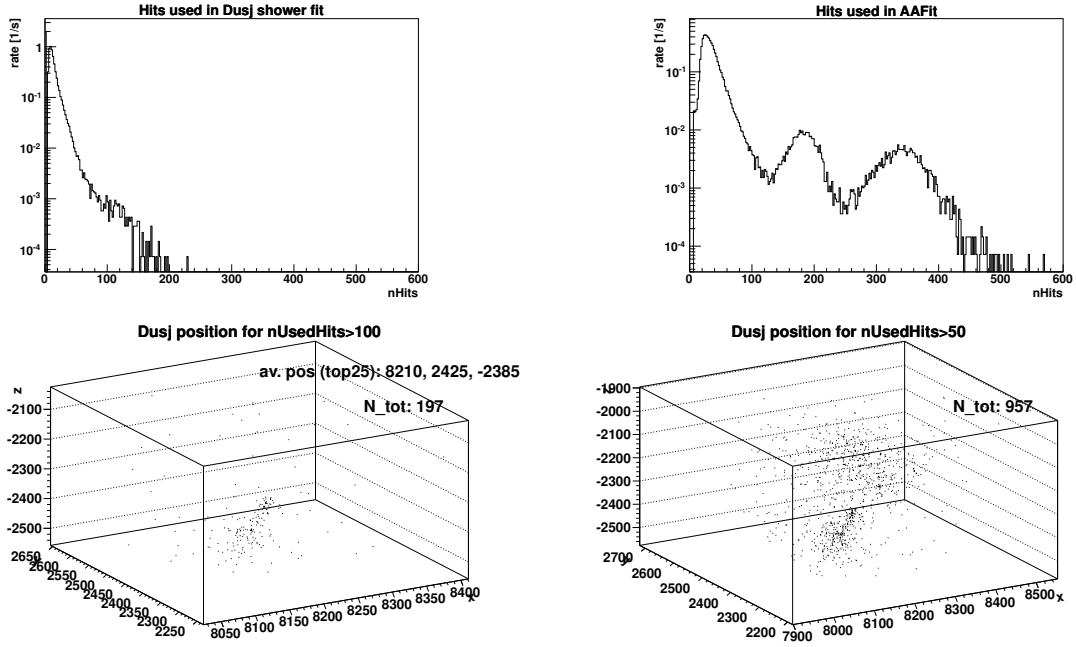

SPARKING RUN 52675: $\overline{r} = 12.6\,\mathrm{m}$, AAFit rate ($\geq 200$ used hits): $1.27\,\mathrm{mHz}$

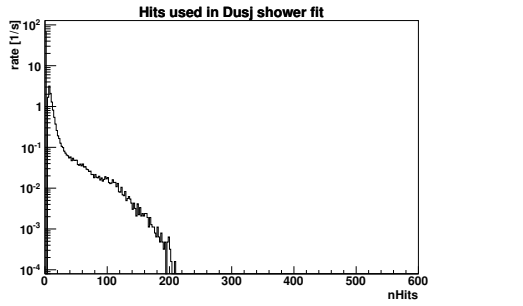

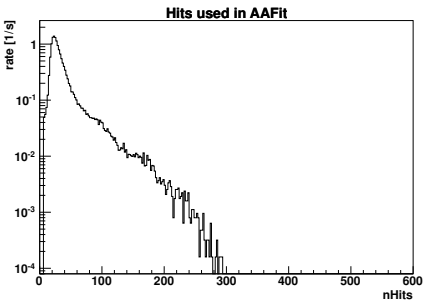

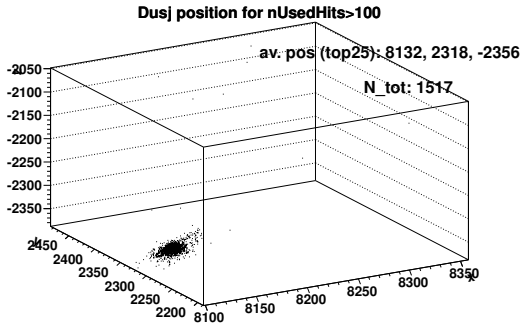

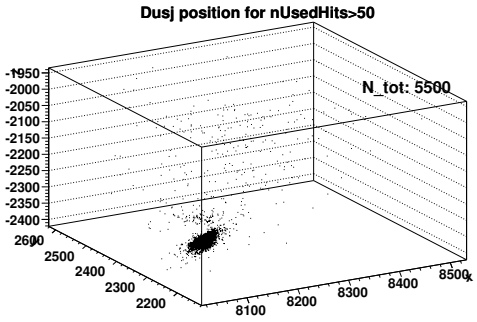

SPARKING RUN 52676: $\overline{r} = 56.4\,\mathrm{m}$, AAFit rate ($\geq 200$ used hits): $0.15\,\mathrm{mHz}$

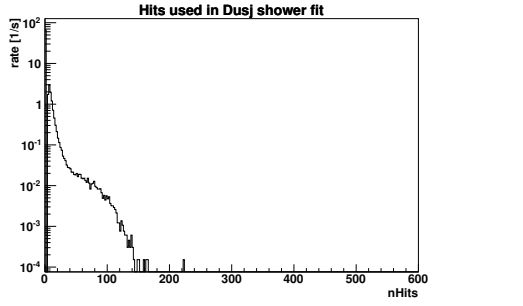

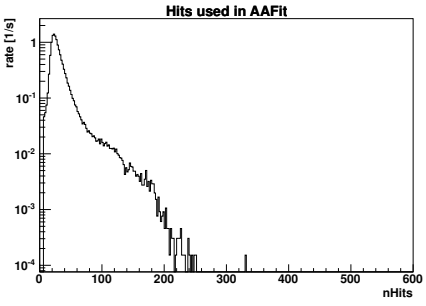

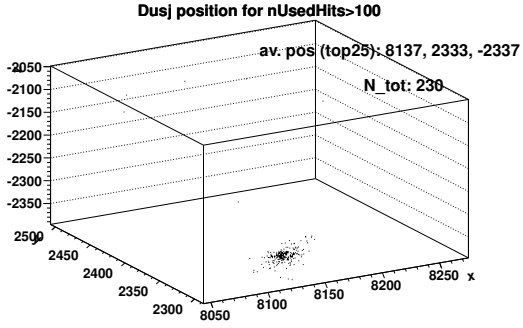

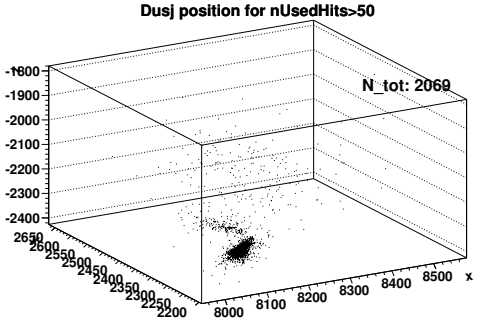

SPARKING RUN 54512: $\overline{r} = 84.2\,\mathrm{m}$, AAFit rate ($\geq 200$ used hits): $22.3\,\mathrm{mHz}$

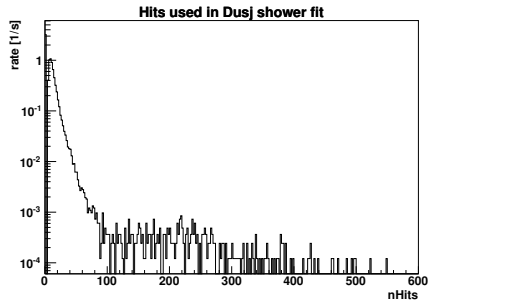

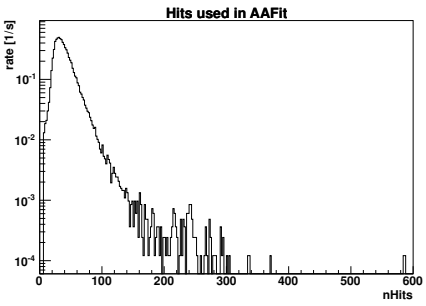

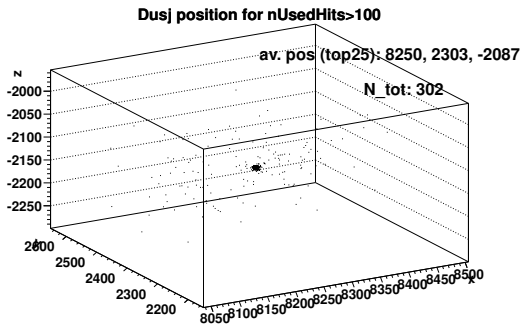

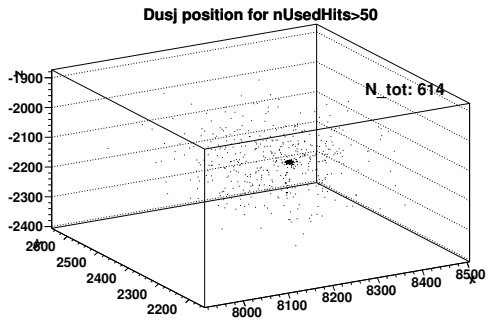

SPARKING RUN 64028: $\overline{r} = 19.9\,\mathrm{m}$, AAFit rate ($\geq 200$ used hits): $0.0\,\mathrm{mHz}$

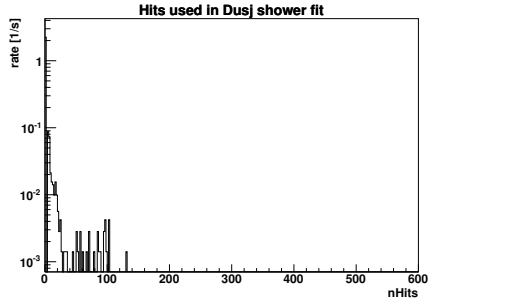

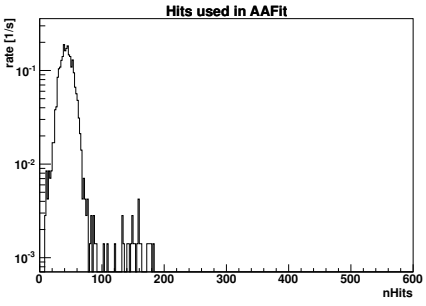

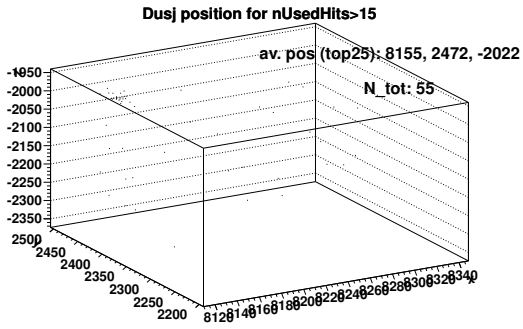

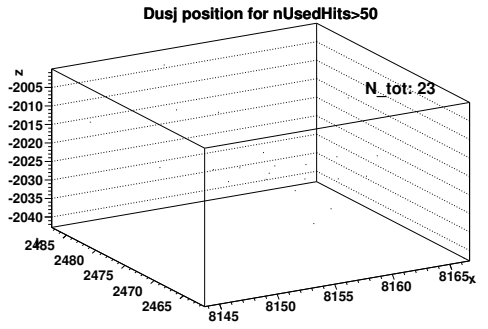

SPARKING RUN 64619: $\overline{r} = 73.9\,\mathrm{m}$, AAFit rate ($\geq 200$ used hits): $0.0\,\mathrm{mHz}$

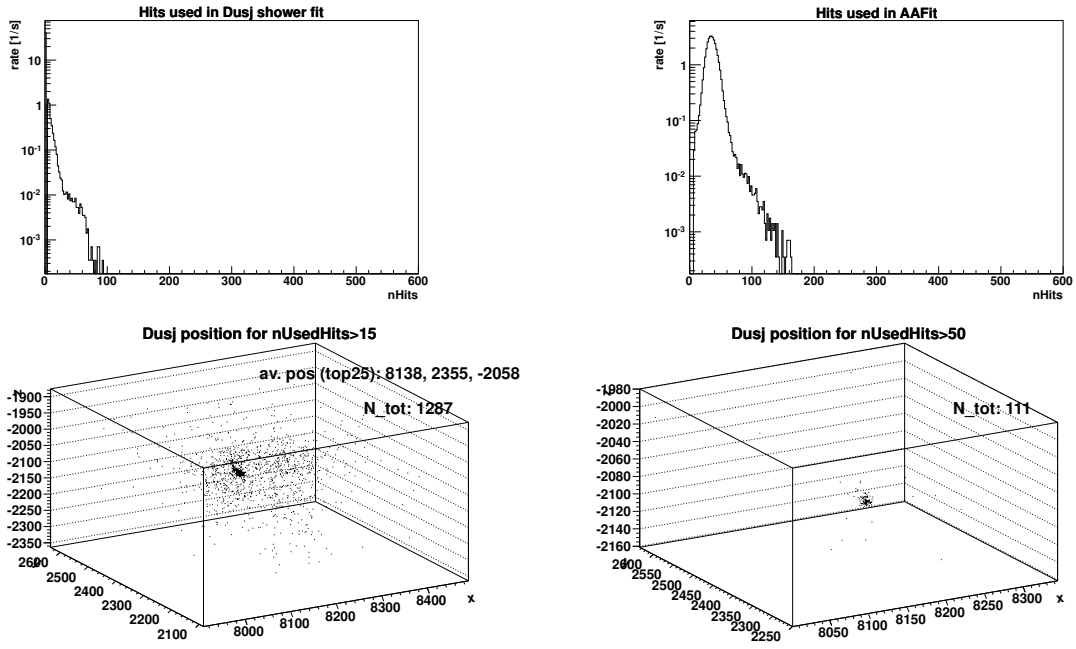

SPARKING RUN 65512: $\overline{r} = 32.4\,\mathrm{m}$, AAFit rate ($\geq 200$ used hits): $0.0\,\mathrm{mHz}$

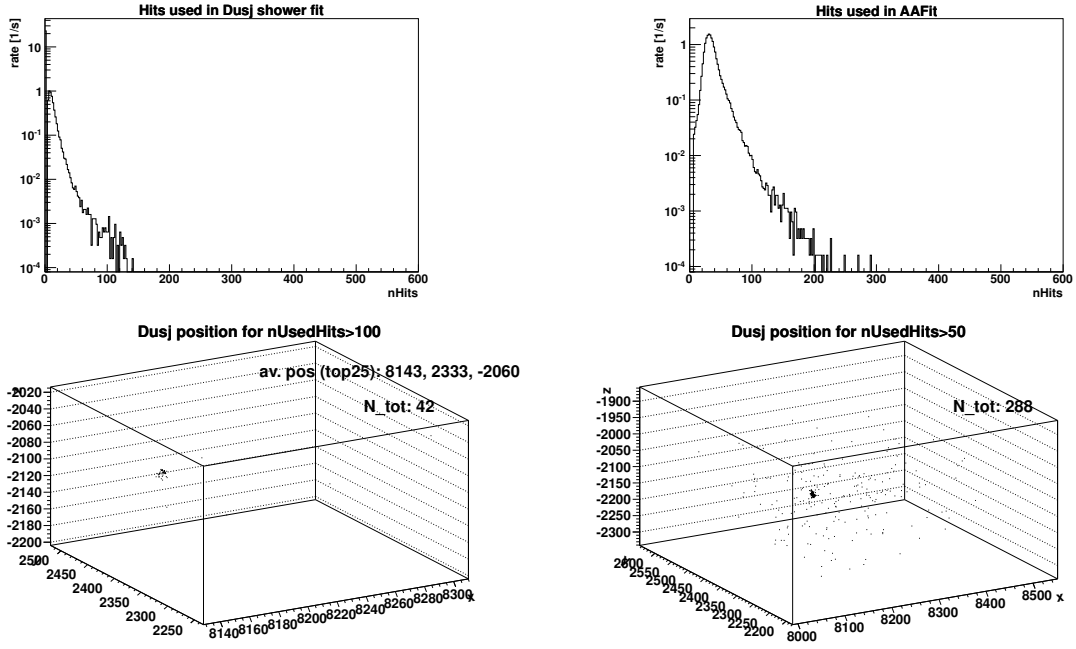

SPARKING RUN 65518: $\overline{r} = 63.5\,\mathrm{m}$, AAFit rate ($\geq 200$ used hits): 0.0 mHz

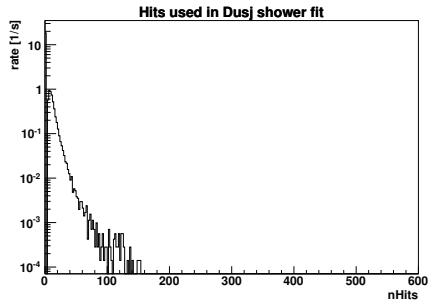

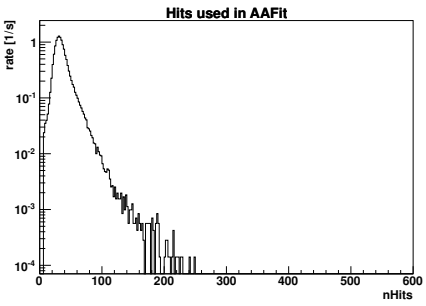

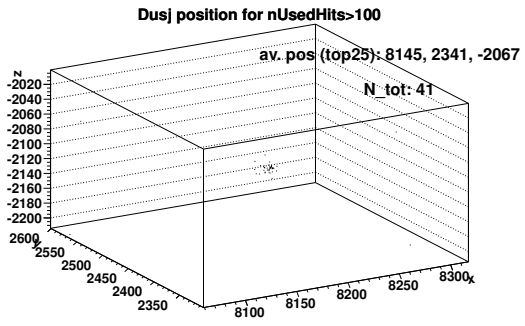

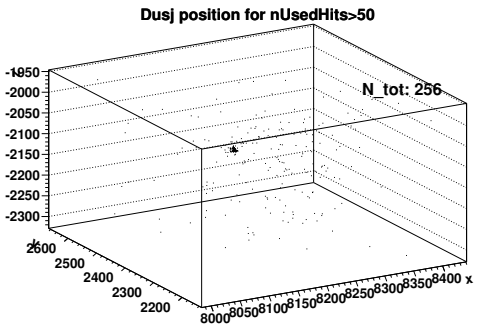

SPARKING RUN 65568: $\overline{r} = 73.7\,\mathrm{m}$, AAFit rate ($\geq 200$ used hits): 0.0 mHz

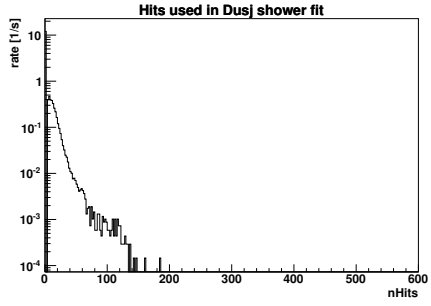

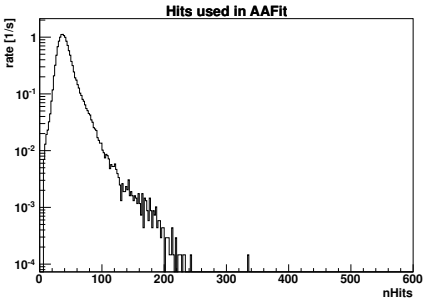

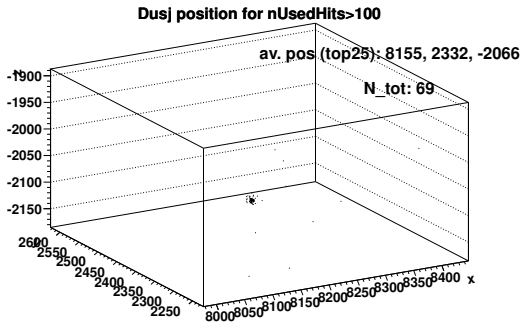

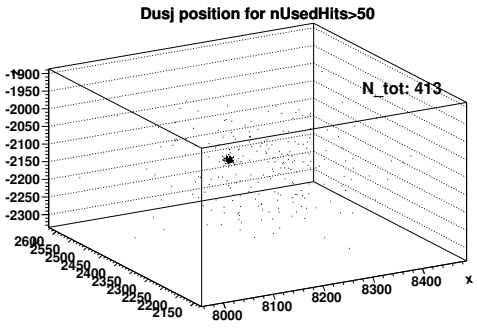

SPARKING RUN 66020: $\overline{r} = 73.6\,\mathrm{m}$, AAFit rate ($\geq 200$ used hits): $0.1\,\mathrm{mHz}$

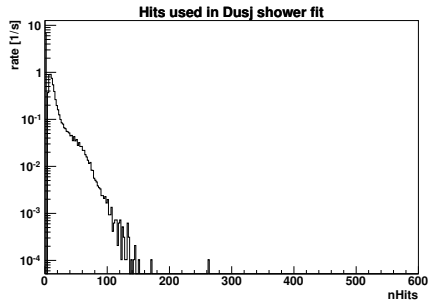

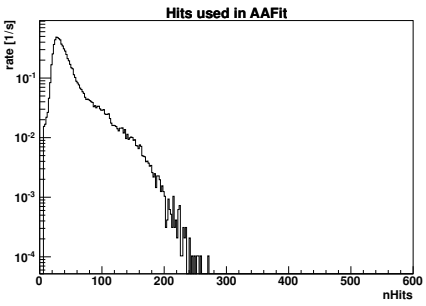

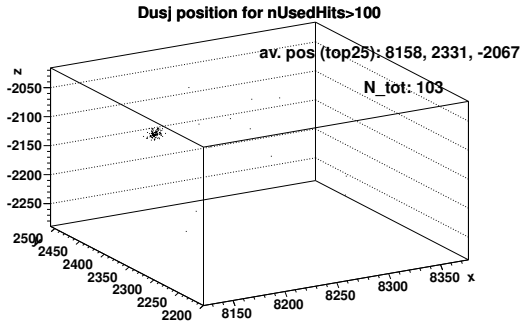

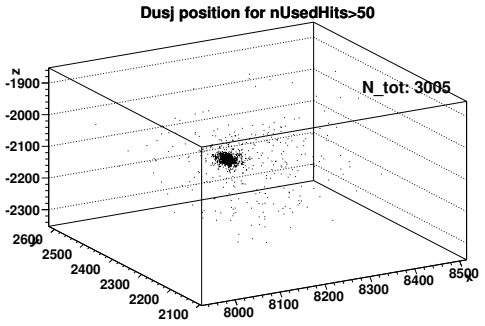

SPARKING RUN 66022: $\overline{r} = 70.1\,\mathrm{m}$, AAFit rate ($\geq 200$ used hits): $0.0\,\mathrm{mHz}$

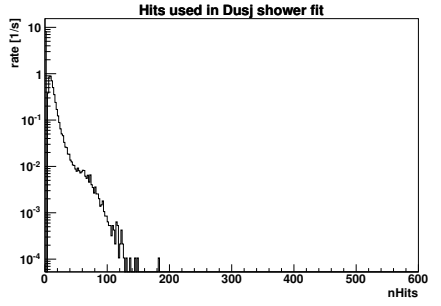

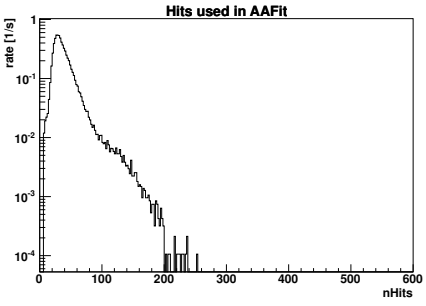

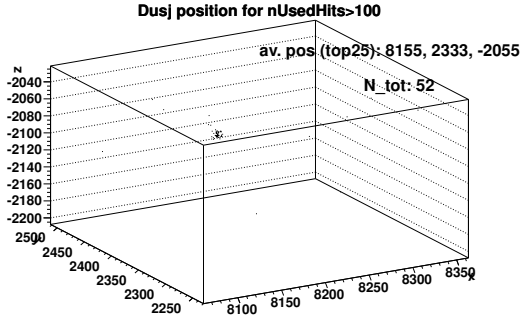

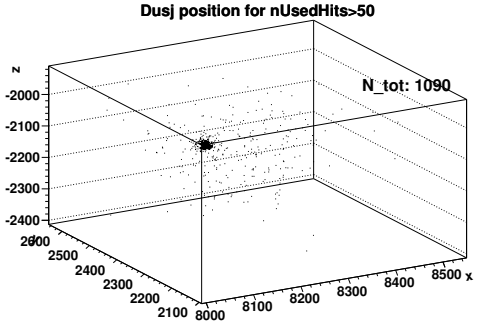

SPARKING RUN 66035: $\overline{r} = 8.6\,\mathrm{m}$, AAFit rate ($\geq 200$ used hits): $2.76\,\mathrm{mHz}$

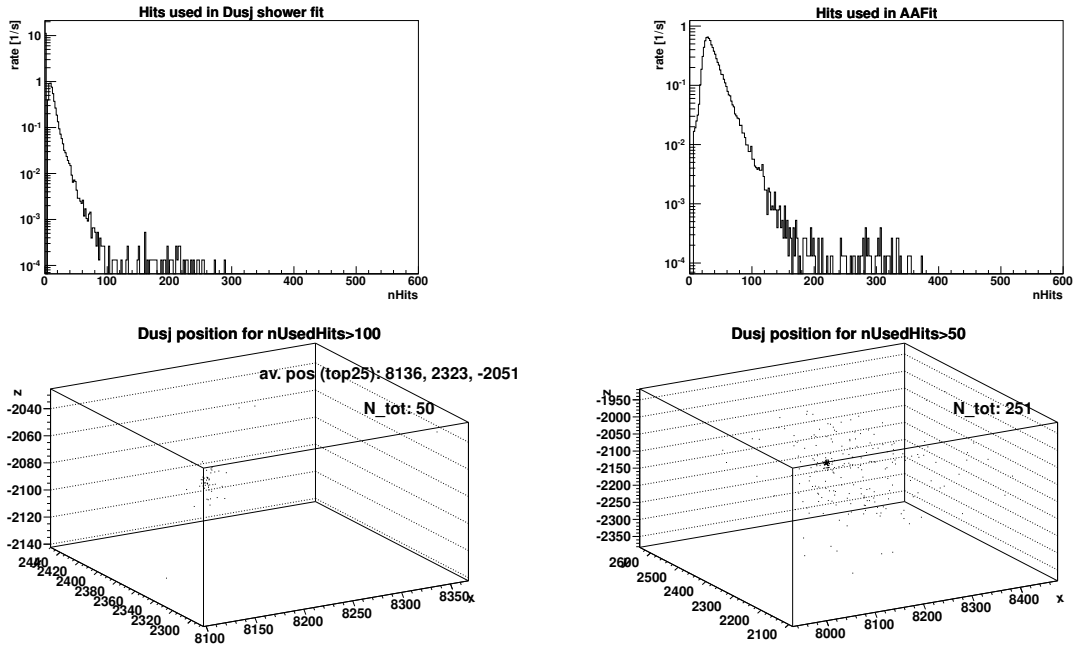

SPARKING RUN 66037: $\overline{r} = 5.4\,\mathrm{m}$, AAFit rate ($\geq 200$ used hits): $10.12\,\mathrm{mHz}$

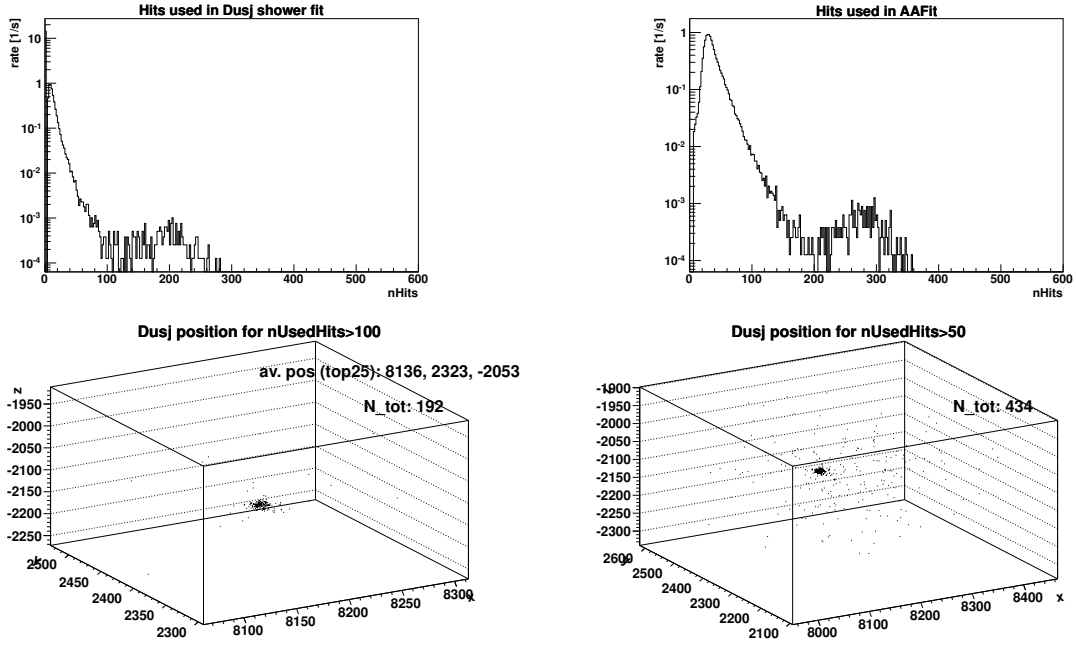

SPARKING RUN 66039: $\overline{r} = 7.7\,\mathrm{m}$, AAFit rate ($\geq 200$ used hits): $2.81\,\mathrm{mHz}$

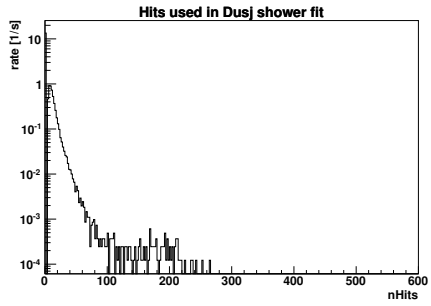

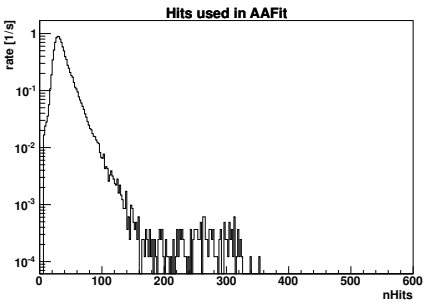

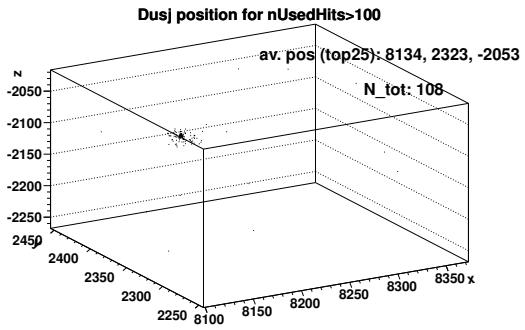

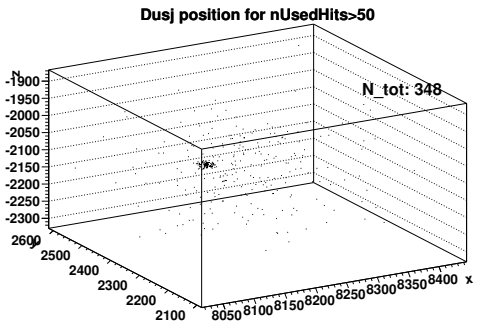

SPARKING RUN 66041: $\overline{r} = 45.7\,\mathrm{m}$, AAFit rate ($\geq 200$ used hits): $1.15\,\mathrm{mHz}$

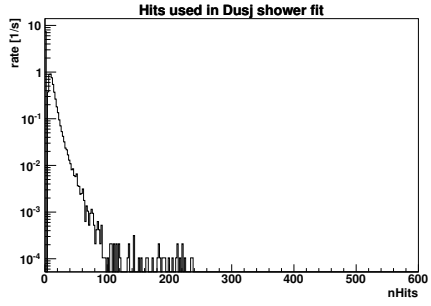

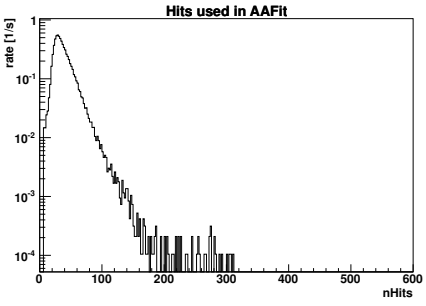

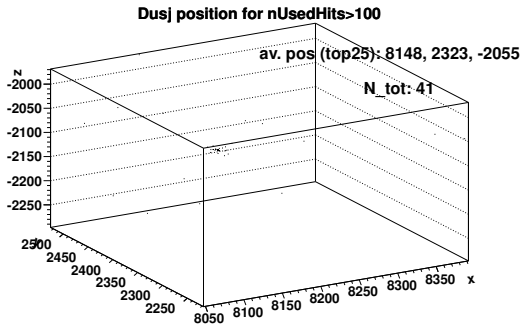

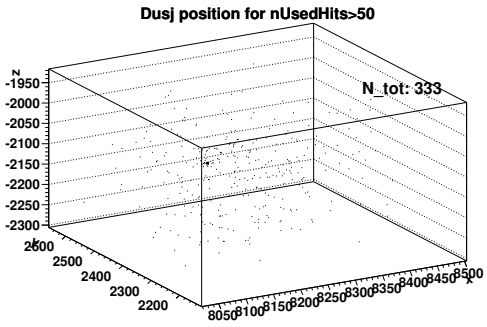

SPARKING RUN 66042: $\overline{r} = 5.3\,\mathrm{m}$, AAFit rate ($\geq 200$ used hits): $16.68\,\mathrm{mHz}$

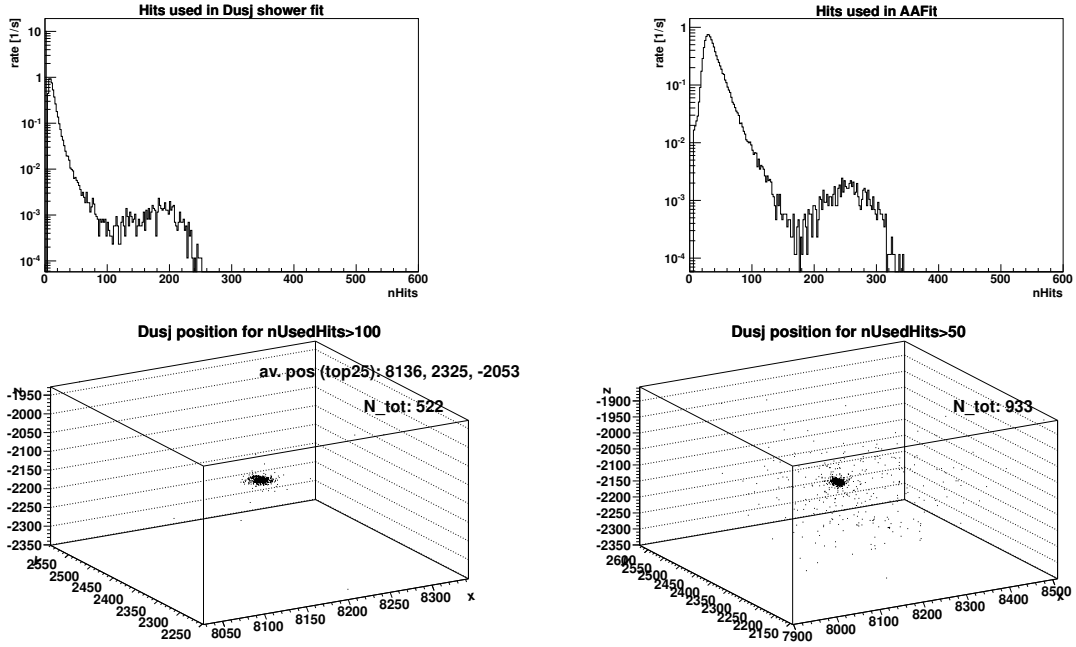

SPARKING RUN 66044: $\overline{r} = 8.4\,\mathrm{m}$, AAFit rate ($\geq 200$ used hits): $0.69\,\mathrm{mHz}$

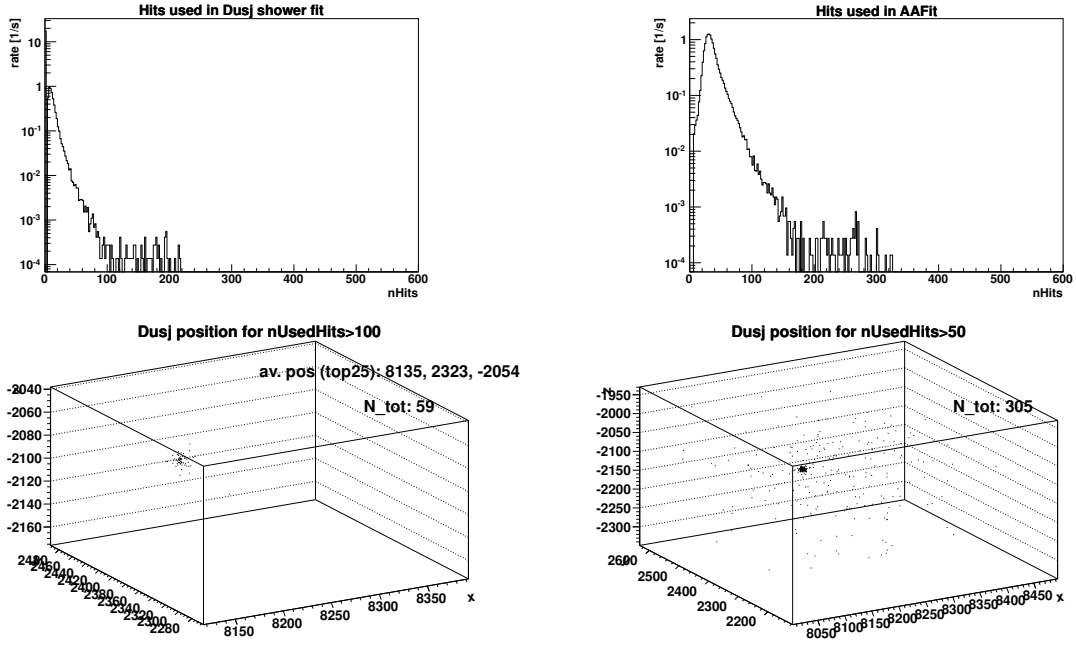

SPARKING RUN 66046: $\overline{r} = 8.7\,\mathrm{m}$, AAFit rate ($\geq 200$ used hits): $0.83\,\mathrm{mHz}$

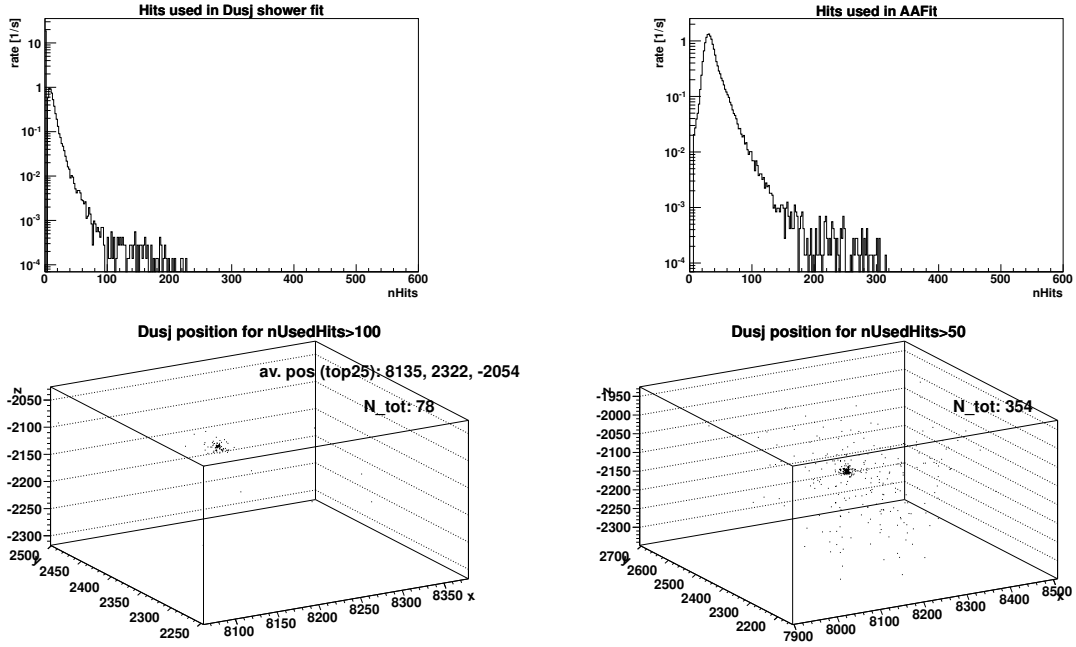

SPARKING RUN 66048: $\overline{r} = 44.2\,\mathrm{m}$, AAFit rate ($\geq 200$ used hits): $0.25\,\mathrm{mHz}$

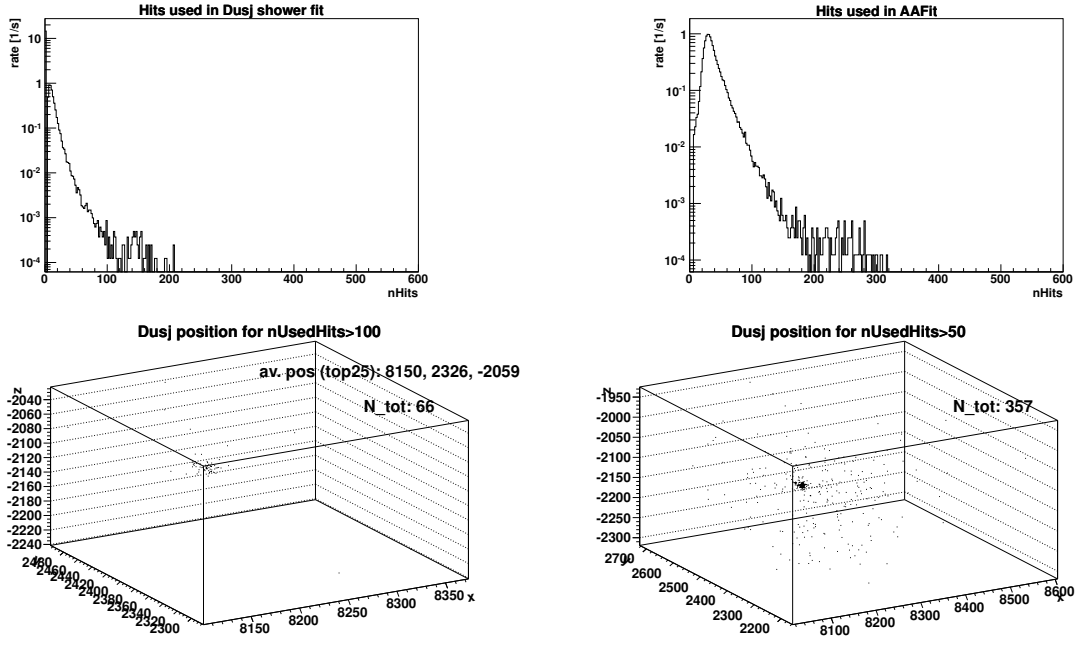

SPARKING RUN 66049: $\overline{r} = 41.2\,\mathrm{m}$, AAFit rate ($\geq 200$ used hits): $1.12\,\mathrm{mHz}$

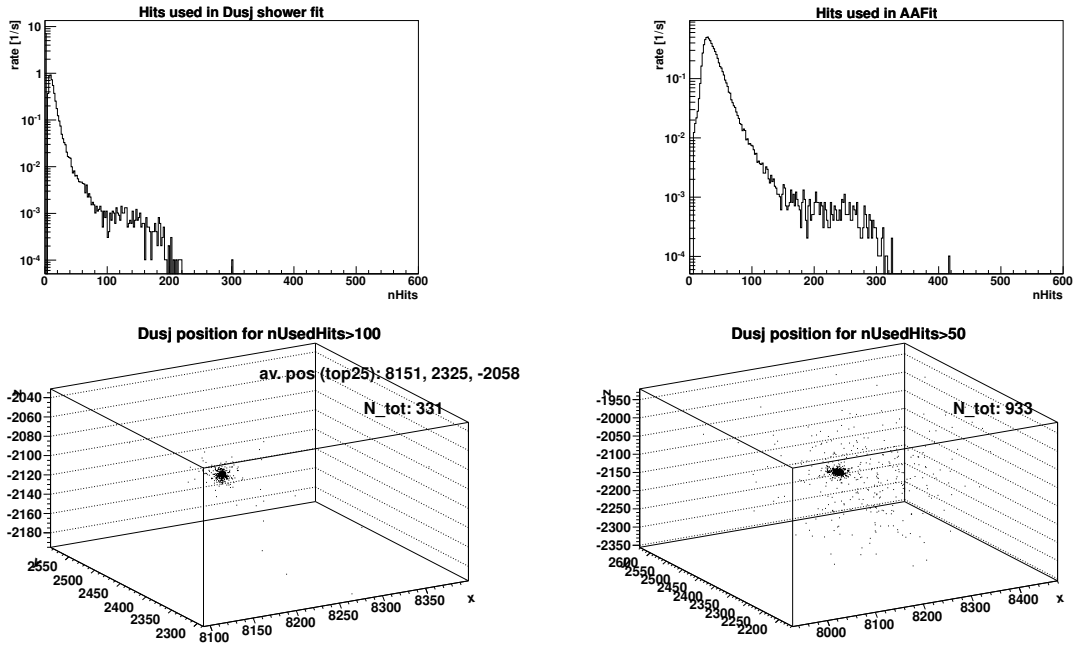

SPARKING RUN 66051: $\overline{r} = 32.4\,\mathrm{m}$, AAFit rate ($\geq 200$ used hits): $0.1\,\mathrm{mHz}$

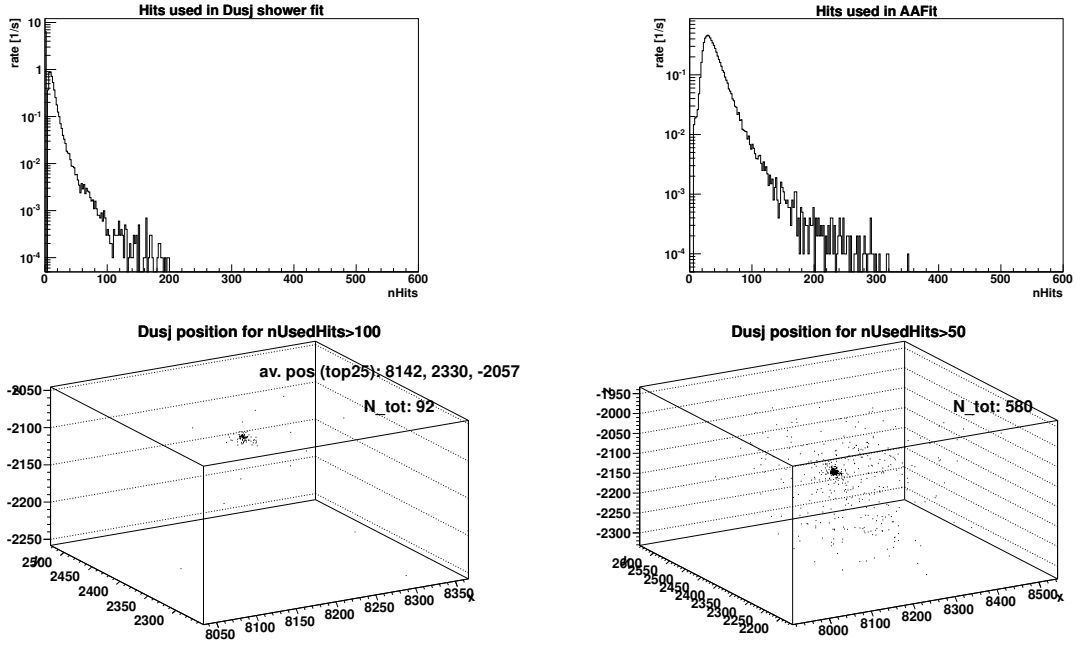

SPARKING RUN 66053: $\overline{r} = 7.3\,\mathrm{m}$, AAFit rate ($\geq 200$ used hits): $4.56\,\mathrm{mHz}$

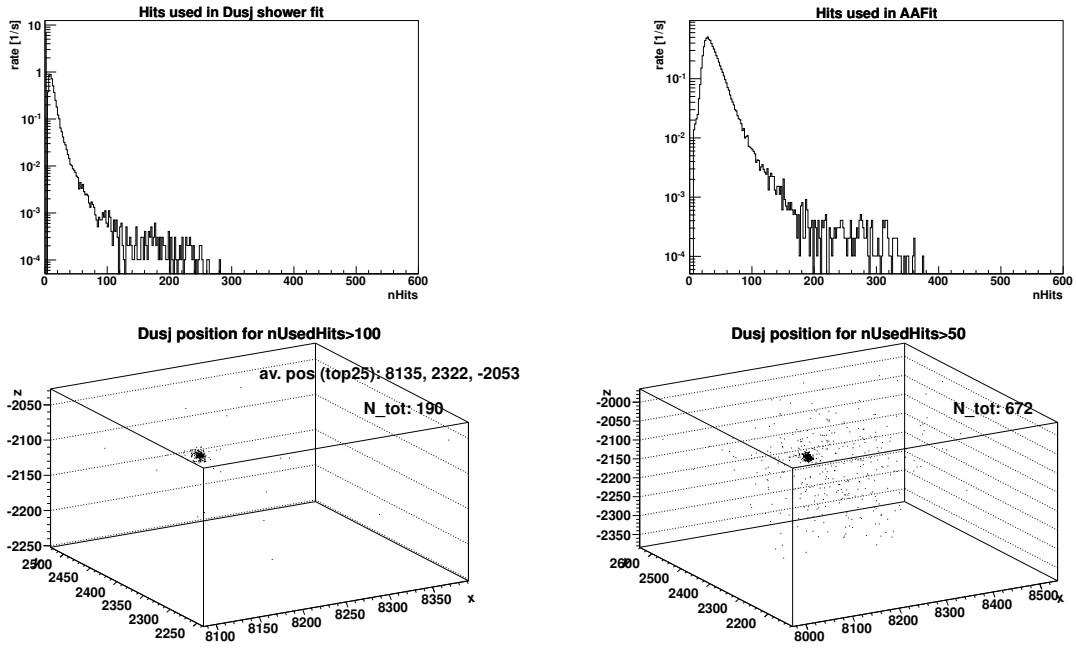

SPARKING RUN 66055: $\overline{r} = 55.5\,\mathrm{m}$, AAFit rate ($\geq 200$ used hits): $0.0\,\mathrm{mHz}$

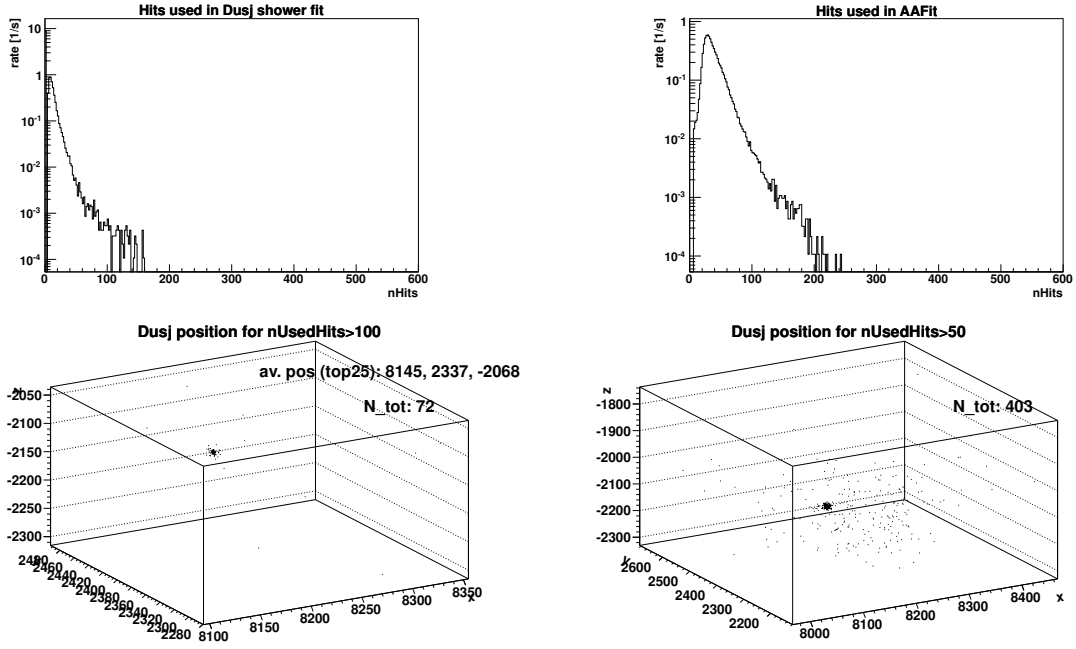

SPARKING RUN 66235: $\overline{r} = 36.0\,\mathrm{m}$, AAFit rate ($\geq 200$ used hits): $0.1\,\mathrm{mHz}$

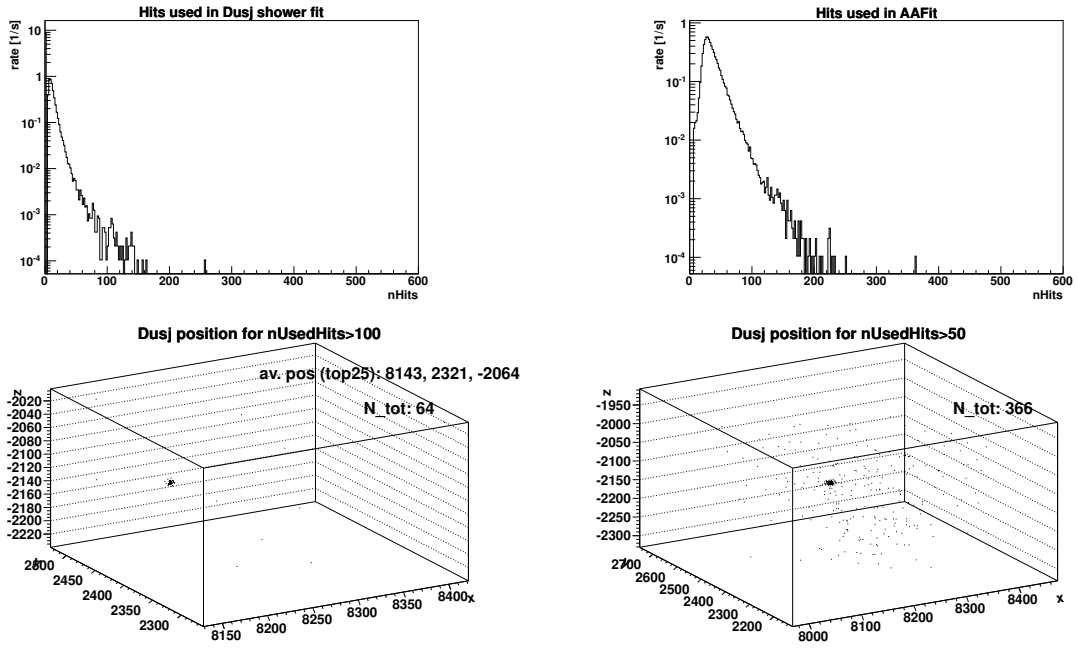

SPARKING RUN 66239: $\overline{r} = 12.8\,\mathrm{m}$, AAFit rate ($\geq 200$ used hits): $0.0\,\mathrm{mHz}$

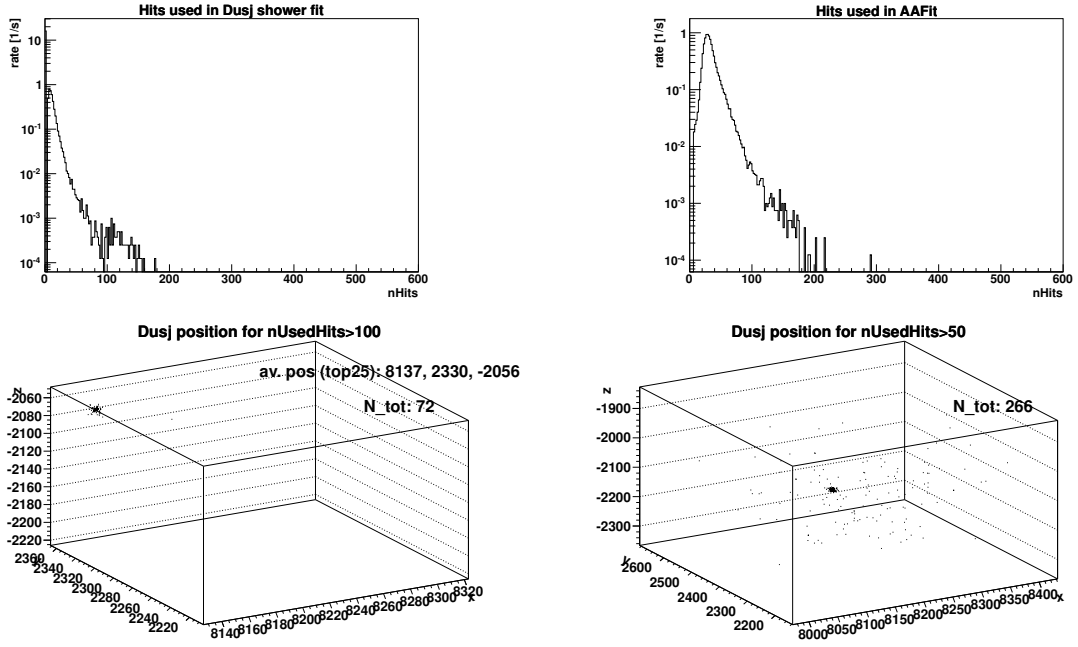

SPARKING RUN 66241: $\overline{r} = 13.8\,\mathrm{m}$, AAFit rate ($\geq 200$ used hits): $0.14\,\mathrm{mHz}$

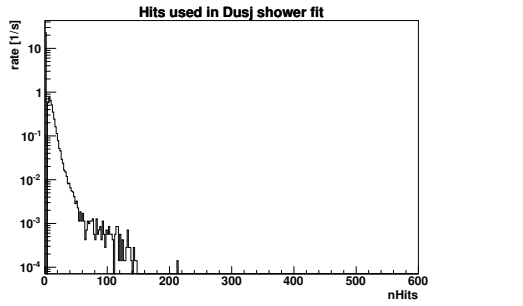

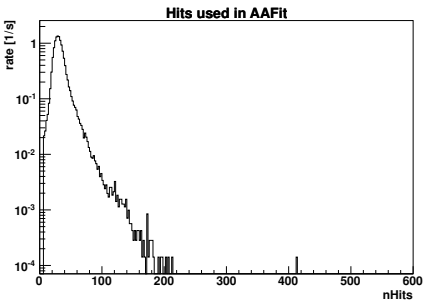

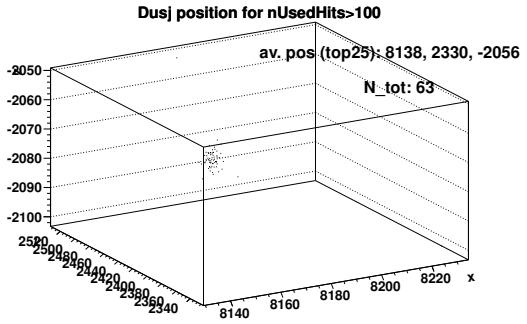

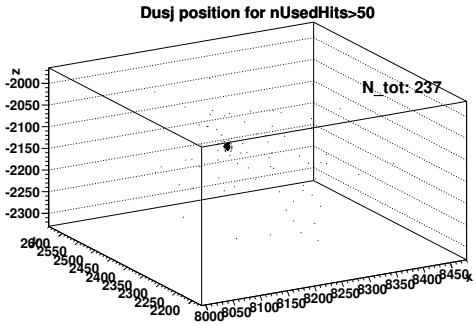

SPARKING RUN 66242: $\overline{r} = 44.5\,\mathrm{m}$, AAFit rate ($\geq 200$ used hits): $0.0\,\mathrm{mHz}$

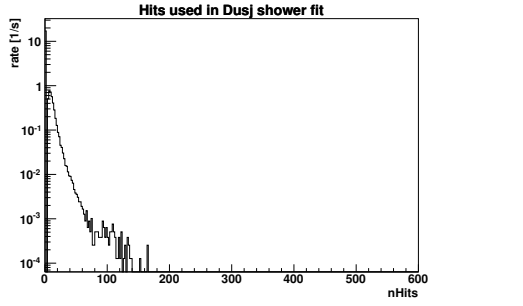

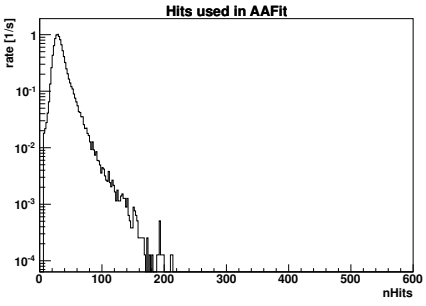

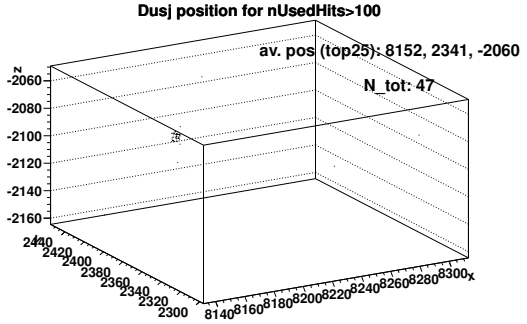

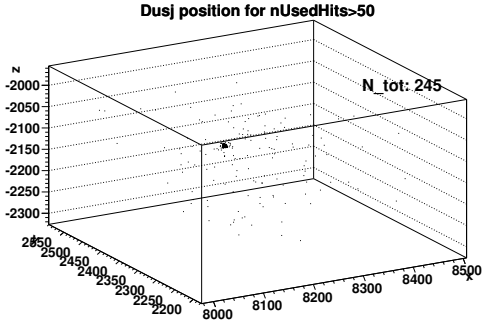

SPARKING RUN 66248: $\overline{r} = 55.8\,\mathrm{m}$, AAFit rate ($\geq 200$ used hits): $0.0\,\mathrm{mHz}$

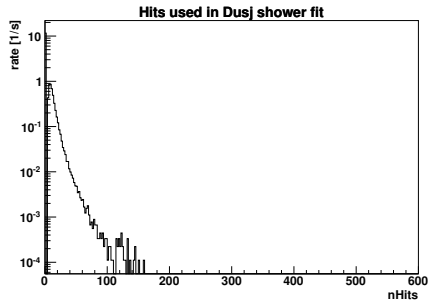

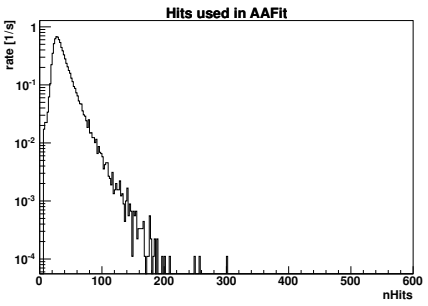

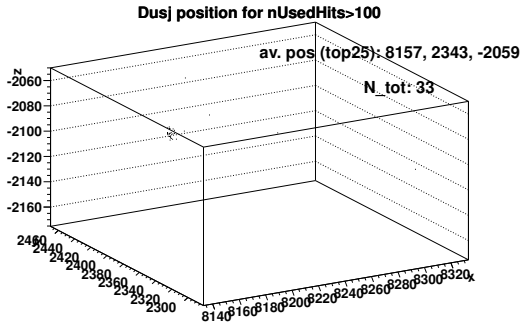

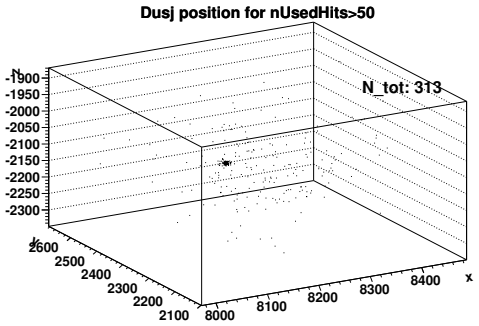

SPARKING RUN 66250: $\overline{r} = 68.1\,\mathrm{m}$, AAFit rate ($\geq 200$ used hits): $0.0\,\mathrm{mHz}$

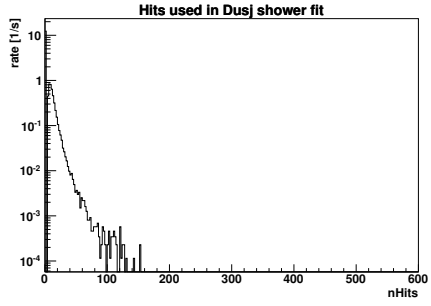

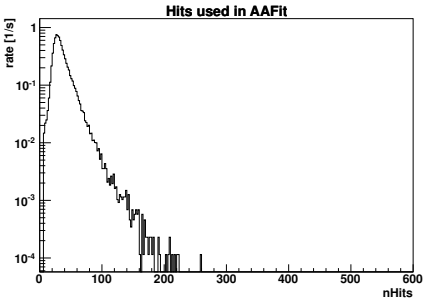

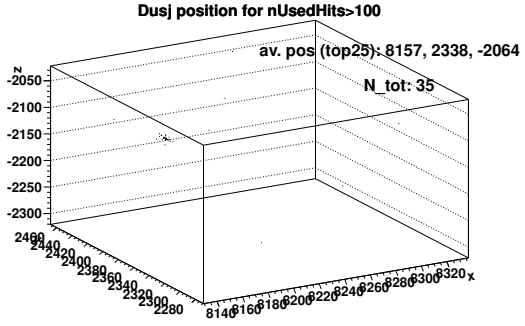

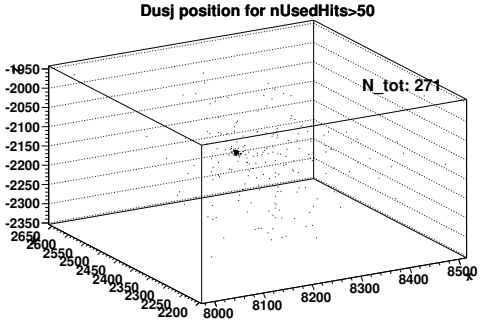

SPARKING RUN 66255: $\overline{r} = 83.5\,\mathrm{m}$, AAFit rate ($\geq 200$ used hits): 0.0 mHz

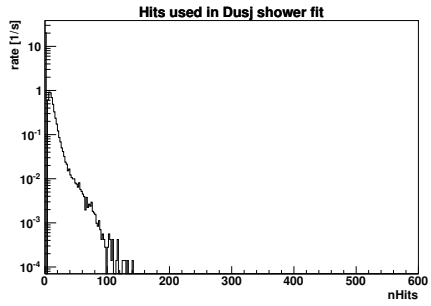

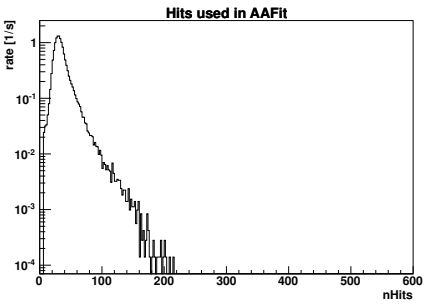

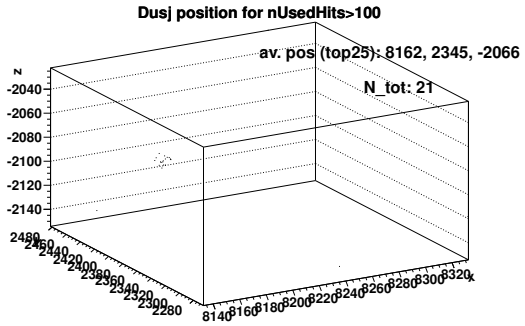

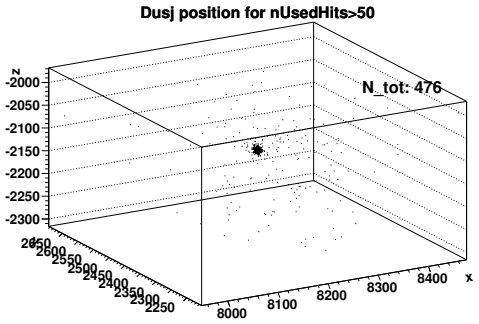

SPARKING RUN 66280: $\overline{r} = 14.6\,\mathrm{m}$, AAFit rate ($\geq 200$ used hits): 0.11 mHz

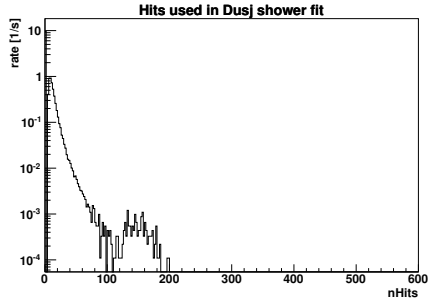

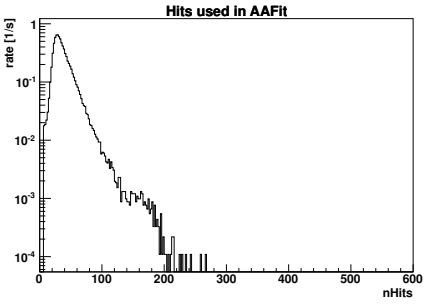

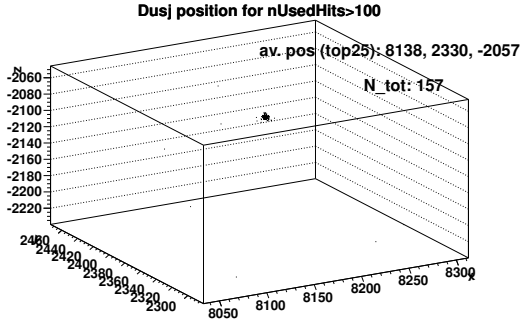

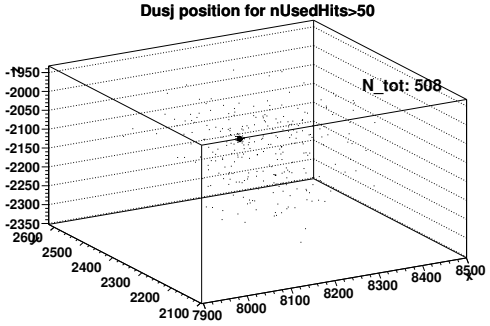

SPARKING RUN 66282: $\overline{r} = 31.9\,\mathrm{m}$, AAFit rate ($\geq 200$ used hits): $0.0\,\mathrm{mHz}$

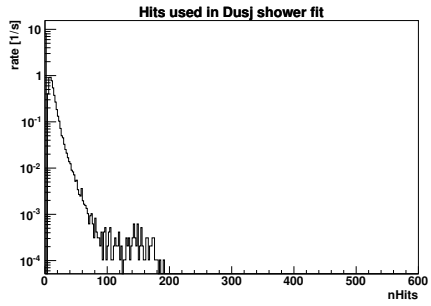

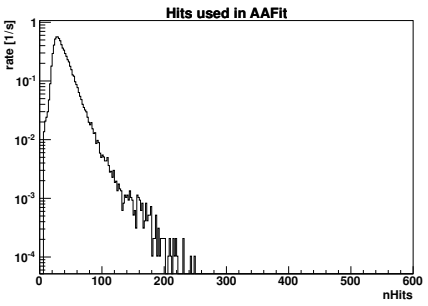

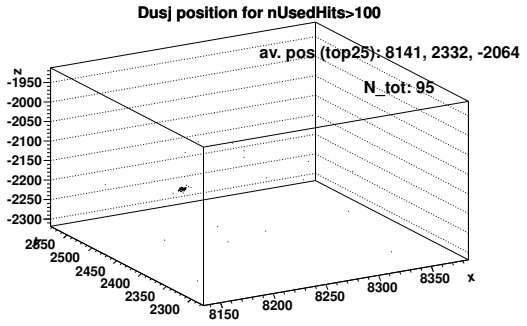

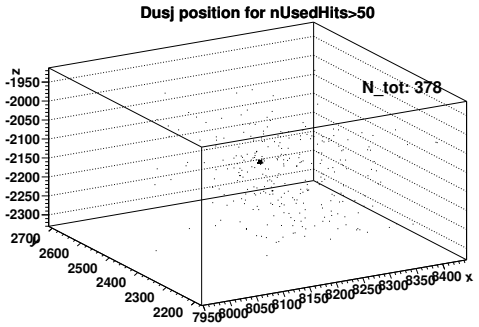

SPARKING RUN 66289: $\overline{r} = 36.9\,\mathrm{m}$, AAFit rate ($\geq 200$ used hits): $0.0\,\mathrm{mHz}$

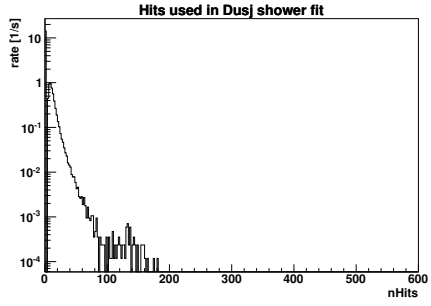

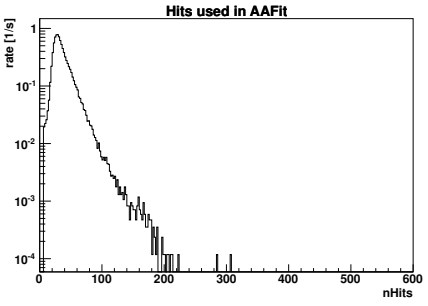

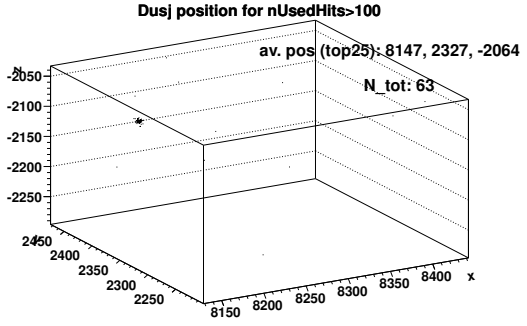

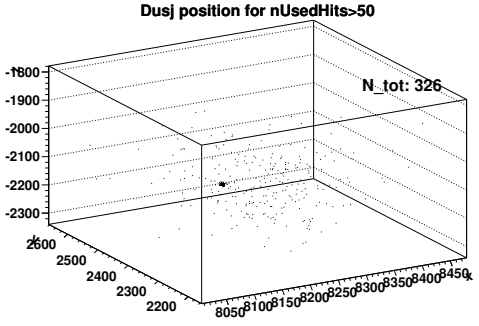

SPARKING RUN 66291: $\overline{r} = 61.5\,\mathrm{m}$, AAFit rate ($\geq 200$ used hits): 0.0 mHz

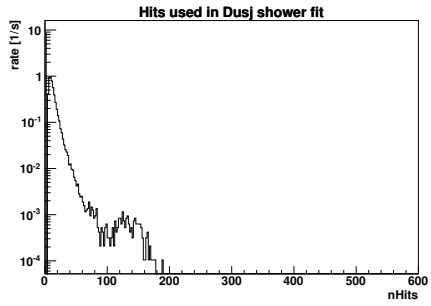

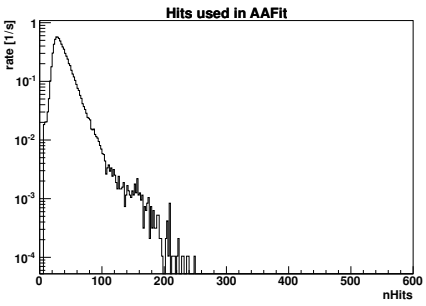

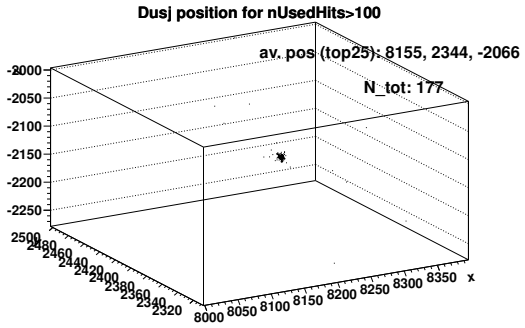

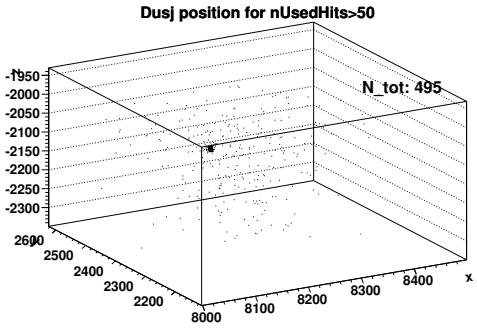

SPARKING RUN 66293: $\overline{r} = 31.0\,\mathrm{m}$, AAFit rate ($\geq 200$ used hits): 0.0 mHz

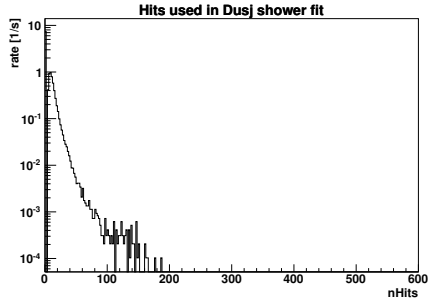

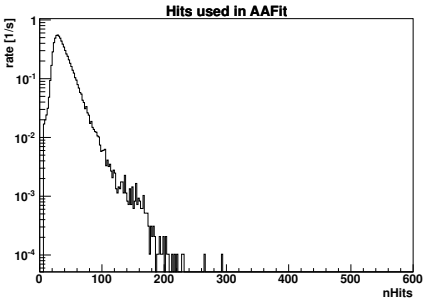

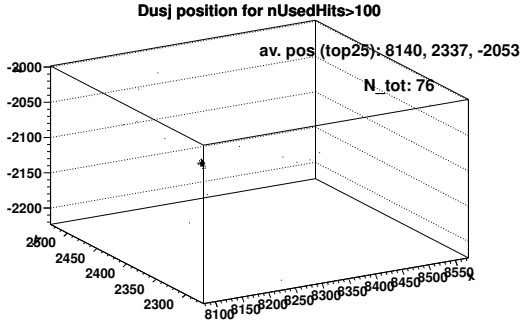

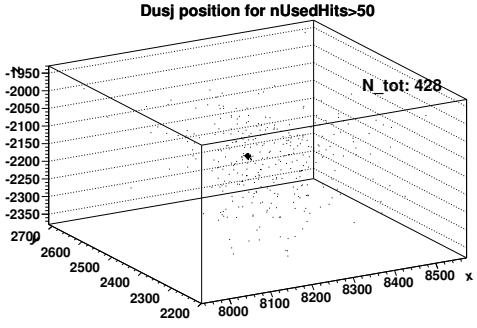

SPARKING RUN 66295: $\overline{r} = 41.9\,\mathrm{m}$, AAFit rate ($\geq 200$ used hits): $0.0\,\mathrm{mHz}$

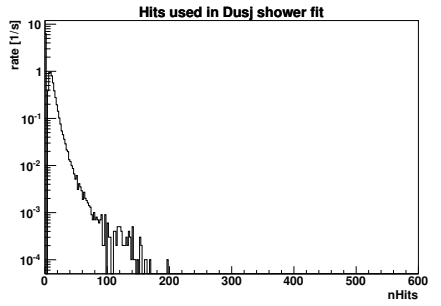

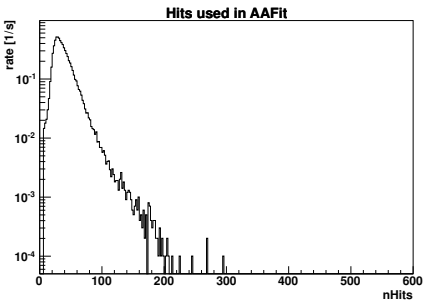

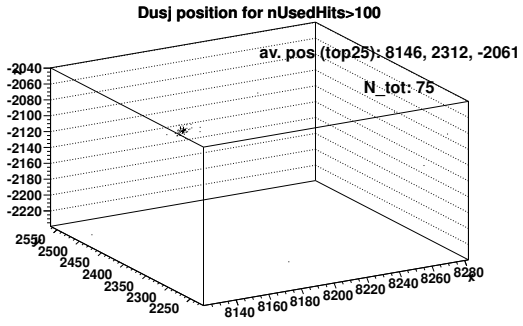

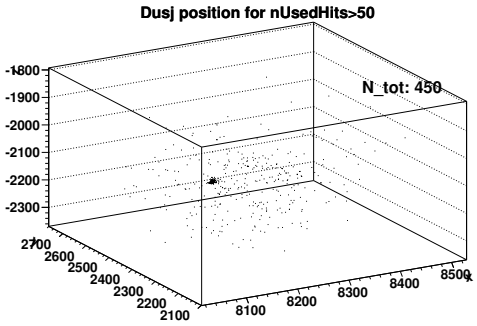

SPARKING RUN 66297: $\overline{r} = 64.3\,\mathrm{m}$, AAFit rate ($\geq 200$ used hits): $0.1\,\mathrm{mHz}$

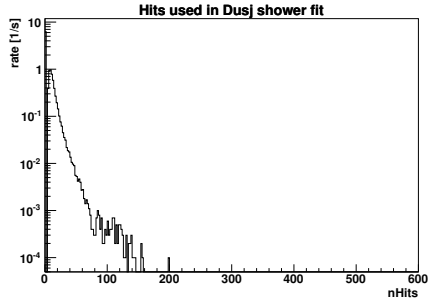

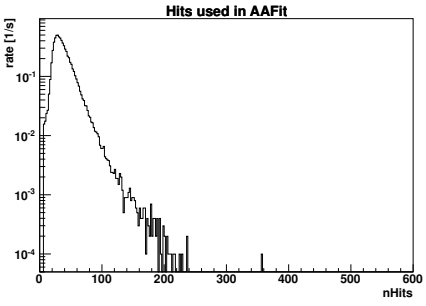

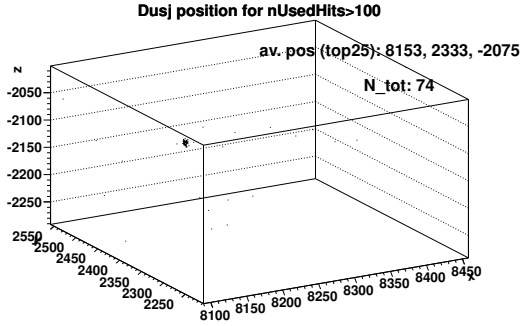

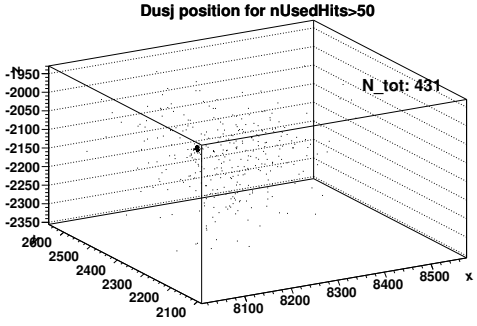

SPARKING RUN 66300: $\overline{r} = 45.6\,\mathrm{m}$, AAFit rate ($\geq 200$ used hits): 0.0 mHz

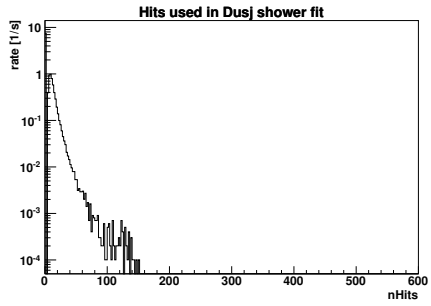

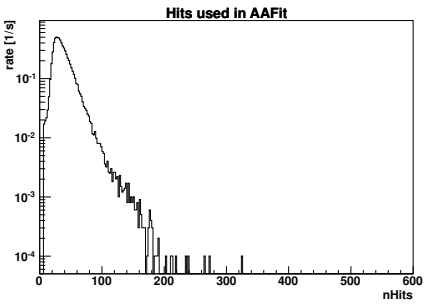

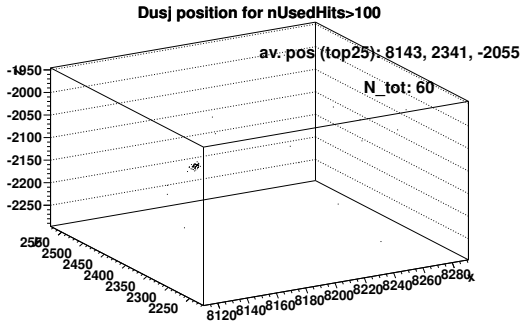

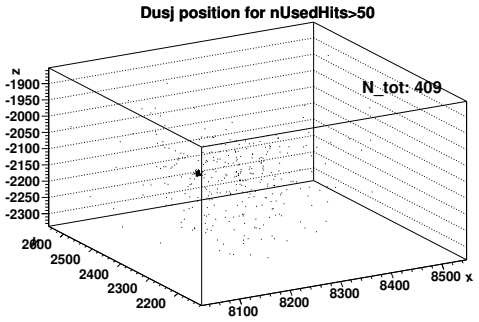

SPARKING RUN 68245: $\overline{r} = 46.5\,\mathrm{m}$, AAFit rate ($\geq 200$ used hits): 0.0 mHz

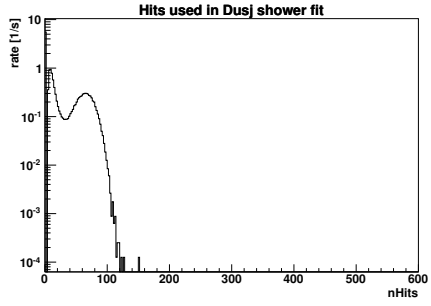

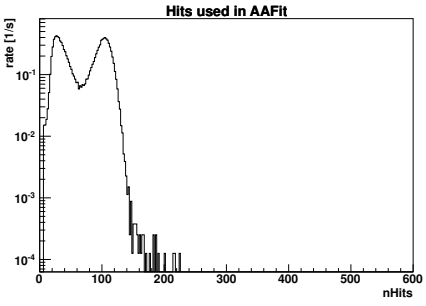

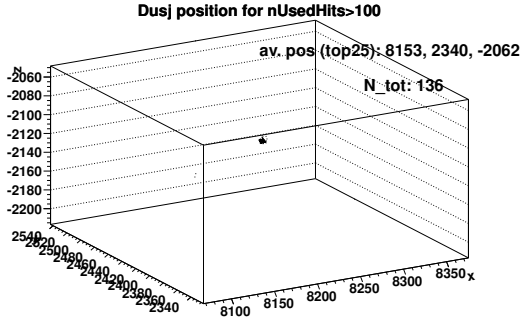

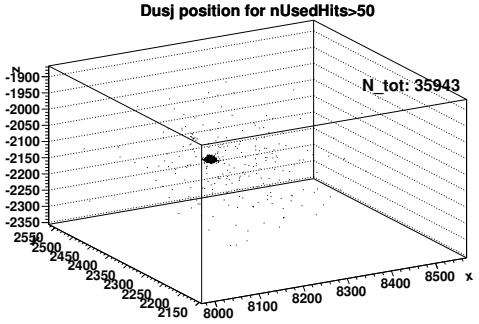

SPARKING RUN 70201: $\overline{r} = 1.3\,\mathrm{m}$, AAFit rate ($\geq 200$ used hits): $40.83\,\mathrm{mHz}$

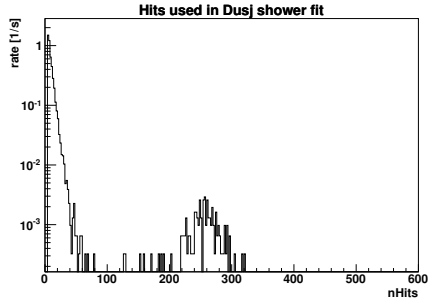

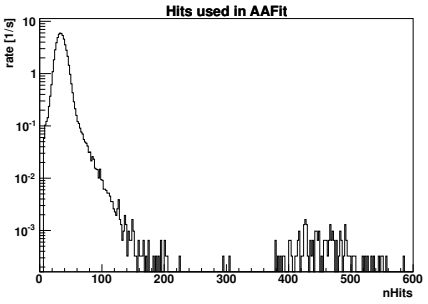

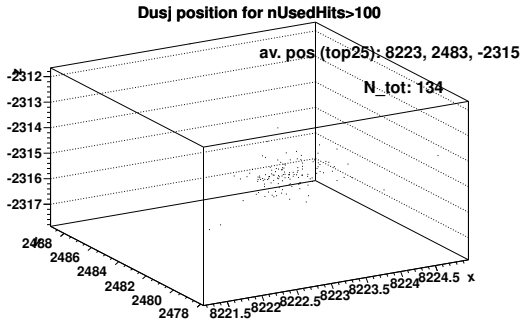

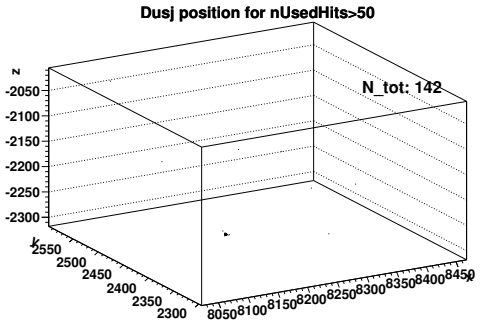

SPARKING RUN 70203: $\overline{r} = 1.2\,\mathrm{m}$, AAFit rate ($\geq 200$ used hits): $7.71\,\mathrm{mHz}$

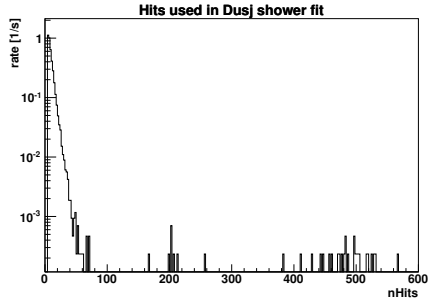

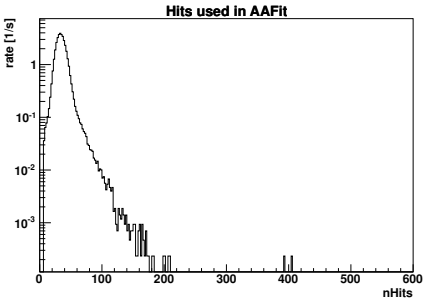

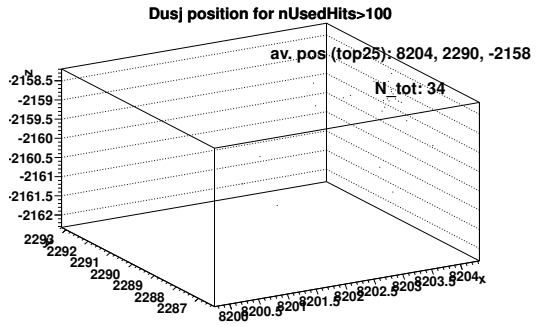

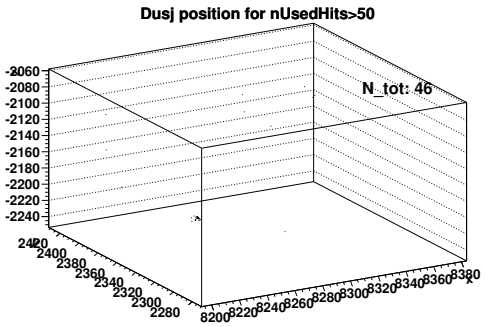

SPARKING RUN 70633: $\overline{r} = 2.4\,\mathrm{m}$, AAFit rate ($\geq 200$ used hits): $0.0\,\mathrm{mHz}$

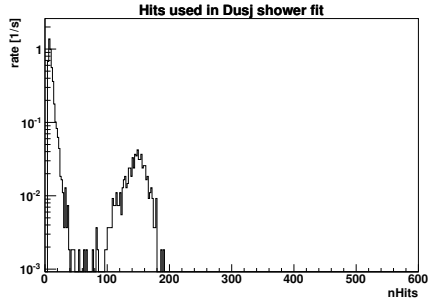

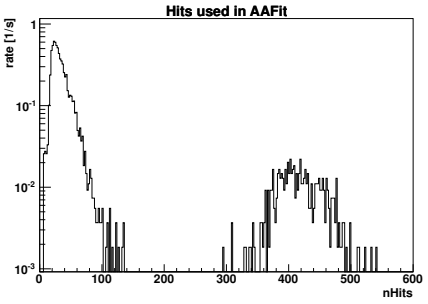

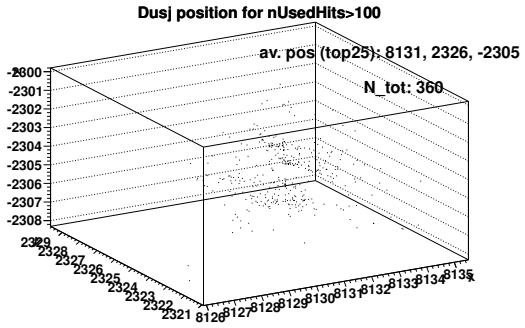

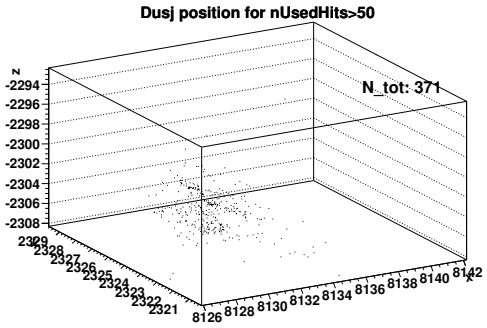

E | List of runs excluded due to bad agreement of measured and simulated data

2010:
45701 45703 45750 46367 46409 46411
2012 & 2013:
62517 63051 63064 63066 63082 63120 63423 63425 63427 63436 63555 63718 63747 63773 64028 64200 64202 64264 64277 64278 64295 64305 64367 64400 64434 64558 64574 64576 64577 64623 64632 64642 64674 64678 64682 64683 64718 64736 64810 64877 64882 64887 64893 64894 64895 64897 64935 64937 64938 64940 64944 64946 64951 64952 64954 64956 65047 65048 65054 65072 65077 65091 65100 65109 65118 65139 65532 66310 67396 67637 68738 68973 69476 69525 70206 70331 70358 70685 70690 70718 70797 70803 70809 70811 70835 70846 70866 70916 70929 70954 70967 70971 70974 70976 71108 71141 71315 71348 71390 71490 71523 71525 72976

F | Event displays for the 6 on-zone events

The event display for all six neutrino candidates found in this analysis looks better for the track reconstruction (AAFit) than for the shower reconstruction (Dusj). The size of the coloured spheres indicates the deposited charge, the coloring indicates times from early (red) to late (blue).

Event 1

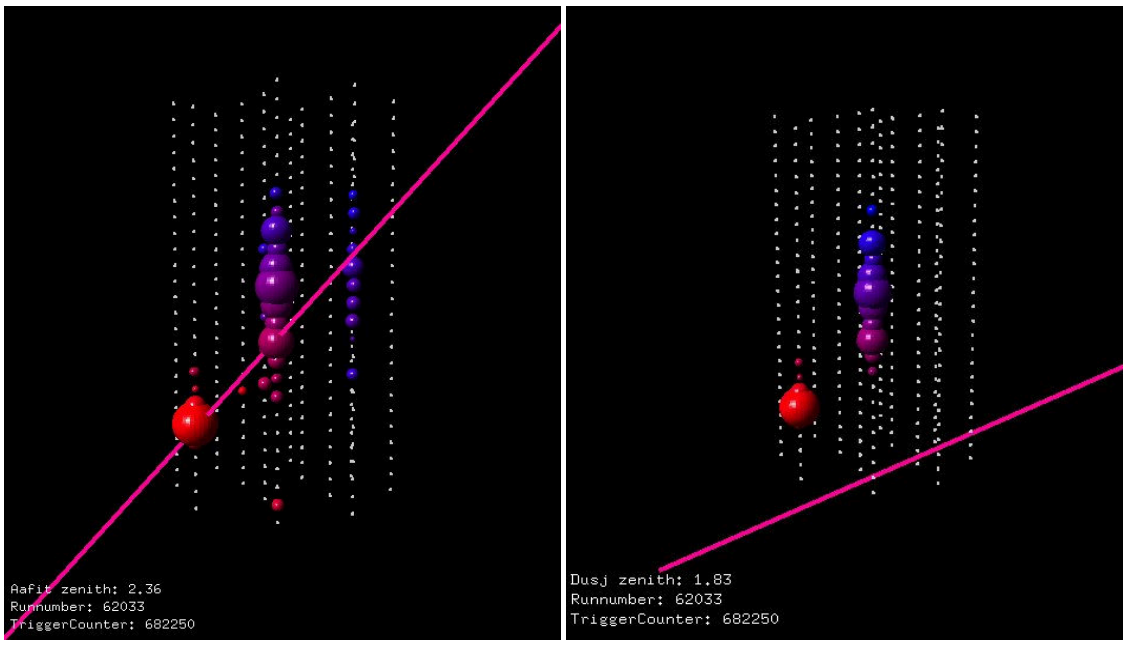

Event 2

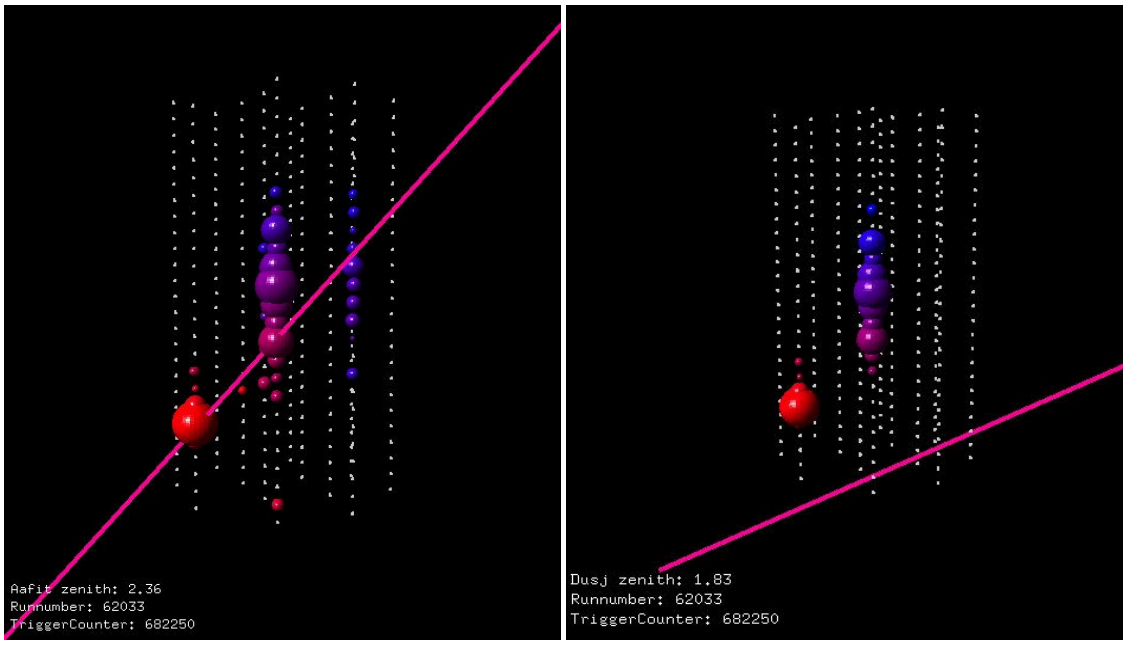

Event 3

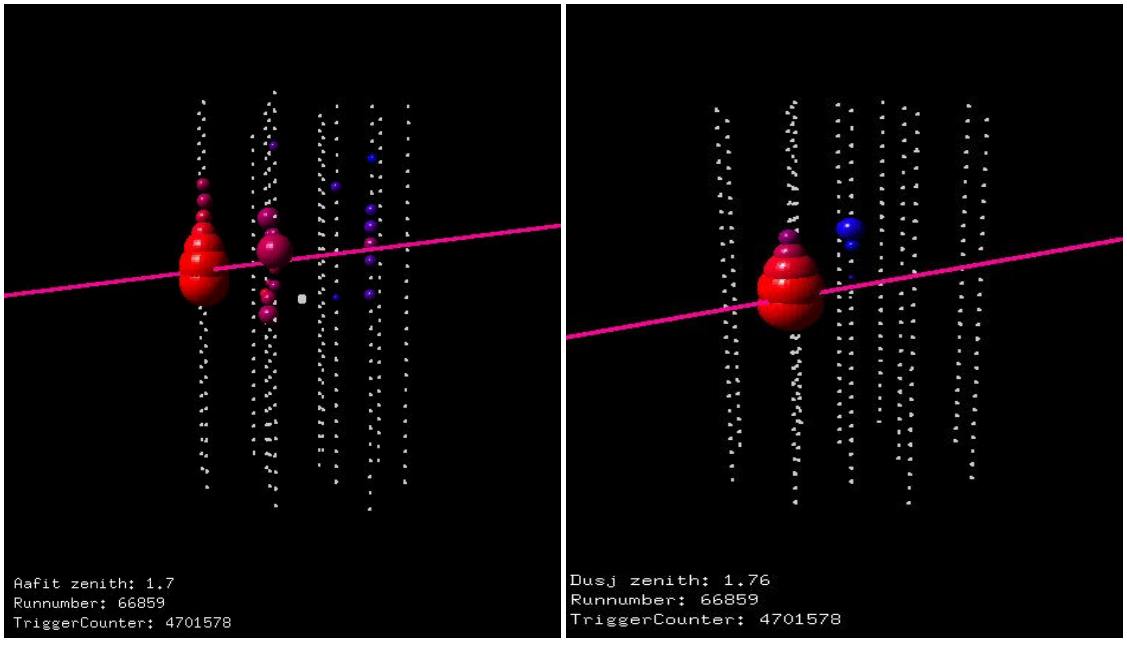

Event 4

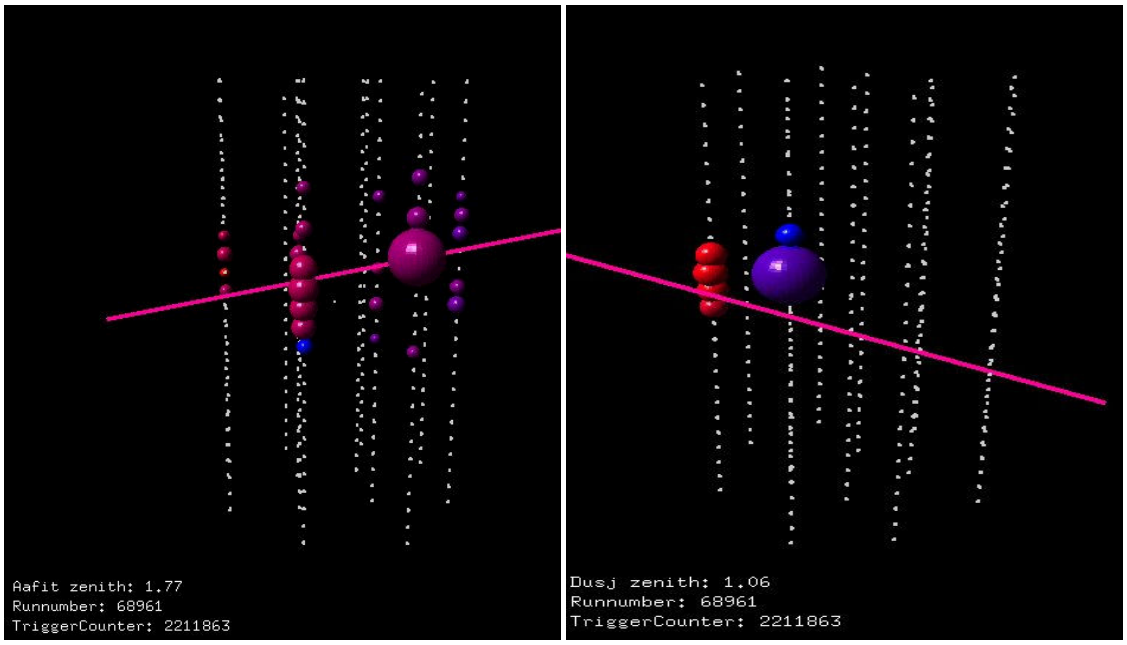

Event 5

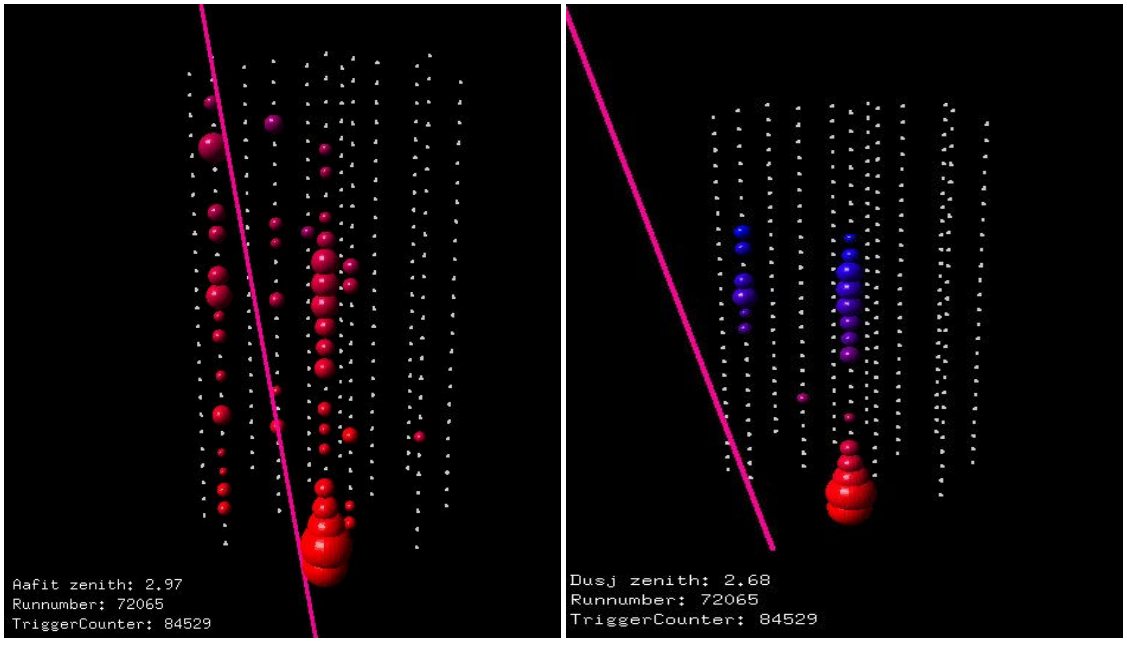

Event 6

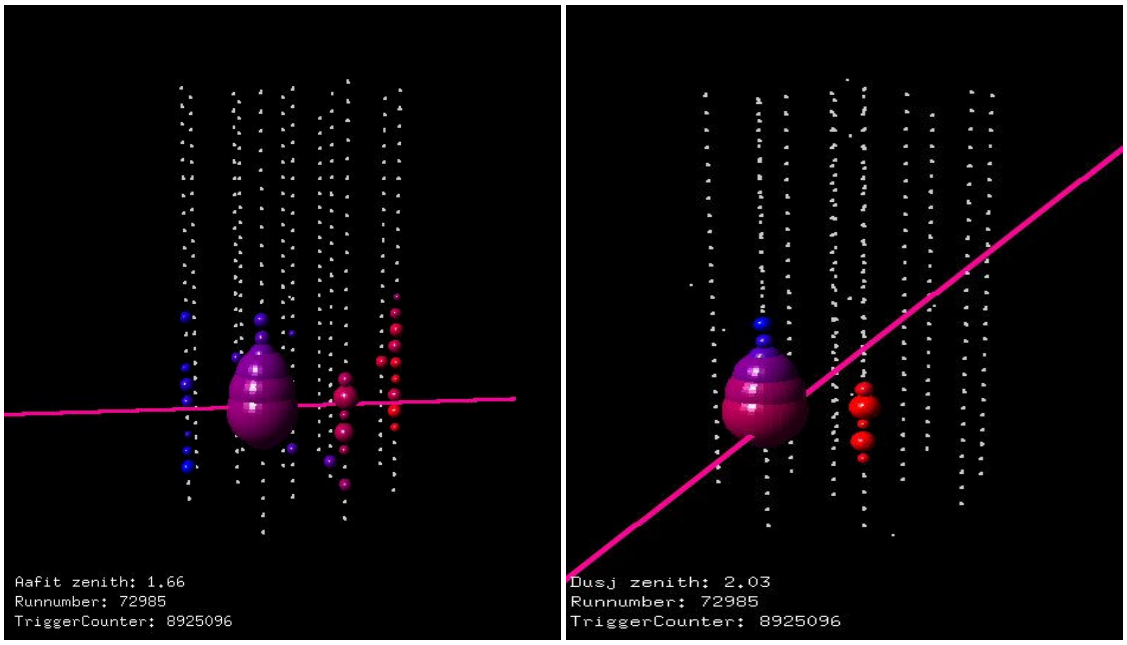
Aafit zenith: 1.66
Runnumber: 72985
TriggerCounter: 8925096
Dusj zenith: 2.03
Runnumber: 72985
TriggerCounter: 8925096

G | MRFs without re-weighting of the background simulation

In the analysis, the atmospheric neutrino flux for 2012 and 2013 is scaled by a factor of 0.7 in order to provide good agreement between data and the Monte Carlo simulation. As a cross check, the MRF optimisation is done without this re-scaling, and the result is given in Tab. 5. The obtained MRF values do not differ significantly. The optimal cut for the reconstructed energy tends to shift to higher energies, because of the increased background.

Table 5: Results for the cut optimisation for an E^{-2} ($E^{-2.18}$) neutrino spectrum on the left (right) with different cutoff energies. In contrast to Tab. 2, the atmospheric neutrino flux is not rescaled in the Monte Carlo to match the data. The coefficient for the flux sensitivity $\overline{A}^{\alpha}_{90\%}$ is given in units of $1 \times 10^{-7}\,\mathrm{GeV}^{\alpha-1}\,\mathrm{cm}^{-2}\,\mathrm{s}^{-1}\,\mathrm{sr}^{-1}$. Gray shaded numbers indicate the cut values used to calculate the 100 TeV cuts sensitivity.

	E^{-2} neutrino spectrum:				$E^{-2.18}$ neutrino spectrum:			
$E_{\mathrm{cutoff},\nu}$ [TeV]	∞	500	100	50	∞	500	100	50
Λ^{cut}	-5.34	-5.27	-5.16	-5.16	-5.26	-5.16	-5.16	-5.16
$\log_{10}\left(E^{\mathrm{cut}}_{\mathrm{reco}}[\mathrm{GeV}]\right)$	4.04	3.87	3.67	3.58	3.86	3.70	3.58	3.50
background MC	7.52	11.3	15.6	19.8	11.5	14.4	19.8	24.2
signal MC	1.6	1.2	0.79	0.62	0.33	0.28	0.21	0.18
$\overline{A}^{\alpha}_{90\%}$	3.82	5.78	9.83	14.7	30.3	40.0	62.3	83.6
Applying the cut values obtained for 100 TeV to all other cutoff energies:								
$\overline{A}^{\alpha}_{90\%}$ (100 TeV cuts)	3.99	5.89	9.83	14.8	31.2	40.6	62.6	84.2
Applying the cut values obtained in 4–year analysis to all cutoff energies:								
$\overline{A}^{\alpha}_{90\%}$ (cuts from Ref. [17])[a]	3.87	5.87	10.2	15.9	30.7	41.0	66.8	93.4

[a] $\Lambda^{\mathrm{cut}} > -5.14$, $\log_{10}\left(E^{\mathrm{cut}}_{\mathrm{reco}}[\mathrm{GeV}]\right) > 4.0\bar{3}$